

December 2012

Accelerating MRI Data Acquisition Using Parallel Imaging and Compressed Sensing

Haifeng Wang

University of Wisconsin-Milwaukee

Follow this and additional works at: <https://dc.uwm.edu/etd>

 Part of the [Biomedical Engineering and Bioengineering Commons](#), and the [Electrical and Electronics Commons](#)

Recommended Citation

Wang, Haifeng, "Accelerating MRI Data Acquisition Using Parallel Imaging and Compressed Sensing" (2012). *Theses and Dissertations*. 207.

<https://dc.uwm.edu/etd/207>

This Dissertation is brought to you for free and open access by UWM Digital Commons. It has been accepted for inclusion in Theses and Dissertations by an authorized administrator of UWM Digital Commons. For more information, please contact open-access@uwm.edu.

Accelerating MRI Data Acquisition

Using Parallel Imaging and Compressed Sensing

by

Haifeng Wang

A Dissertation Submitted in

Partial Fulfillment of the

Requirements for the Degree of

Doctor of Philosophy

in Engineering

at

The University of Wisconsin-Milwaukee

December 2012

ABSTRACT

ACCELERATING MRI DATA ACQUISITION USING PARALLEL IMAGING AND COMPRESSED SENSING

by

Haifeng Wang

The University of Wisconsin-Milwaukee, 2012
Under the Supervision of Professor Leslie (Lei) Ying and Jun Zhang

Magnetic Resonance Imaging (MRI) scanners are one of important medical instruments, which can achieve more information of soft tissues in human body than other medical instruments, such as Ultrasound, Computed Tomography (CT), Single Photon Emission Computed Tomography (SPECT), Positron Emission Tomography (PET), etc. But MRI's scanning is slow for patience of doctors and patients. In this dissertation, the author proposes some methods of parallel imaging and compressed sensing to accelerate MRI data acquisition. Firstly, a method is proposed to improve the conventional GRAPPA using cross-sampled auto-calibration data. This method use cross-sampled auto-calibration data instead of the conventional parallel-sampled auto-calibration data to estimate the linear kernel model of the conventional GRAPPA. The simulations and experiments show that the cross-sampled GRAPPA can decrease the quantity of ACS lines and reduce the aliasing artifacts comparing to the conventional GRAPPA under same reduction factors. Secondly, a Hybrid encoding method is proposed to accelerate the MRI data acquisition using compressed sensing. This method completely changes the conventional Fourier encoding into Hybrid encoding, which combines the benefits of Fourier and Circulant random encoding, under 2D and 3D situation, through the proposed special hybrid encoding pulse sequences. The

simulations and experiments illustrate that the images can be reconstructed by the proposed Hybrid encoding method to reserve more details and resolutions than the conventional Fourier encoding method. Thirdly, a pseudo 2D random sampling method is proposed by dynamically swapping the gradients of x and y axes on pulse sequences, which can be implemented physically as the convention 1D random sampling method. The simulations show that the proposed method can reserve more details than the convention 1D random sampling method. These methods can recover images to achieve better qualities under same situations than the conventional methods. Using these methods, the MRI data acquisitions can be accelerated comparing to the conventional methods.

© Copyright by Haifeng Wang, 2012
All Rights Reserved

TABLE OF CONTENTS

1. Introduction	1
1.1 Parallel MRI	2
1.1.1 Parallel Imaging.....	2
1.1.2 SENSE	5
1.1.3 GRAPPA.....	6
1.2 Compressed Sensing.....	7
1.3 Benefits and Limitations.....	8
1.4 Our Works.....	9
2. Purpose of the Dissertation	11
3. Proposed Schemes	11
3.1 GRAPPA Using Cross Sampling	11
3.1.1 Summary of GRAPPA	13
3.1.2 Which ACS data are important?	14
3.1.3 Cross Sampling Method.....	15
3.1.4 Data Co-registration.....	17
3.1.5 Image Reconstruction	20
3.1.6 Nonlinear Denoise	21
3.2 Hybrid-Encoded MRI Using Compressed Sensing	24
3.2.1. Compressed Sensing.....	26
3.2.2. Circulant random matrices.....	28
3.2.2. Hybrid Encoding Scheme	30
3.2.3. Pulse Sequence Design	33
3.2.4. Bloch Equation Simulation.....	38

3.2.5. Pulse Sequence Implementation	43
3.3 Pseudo 2D Random Sampling in CS MRI	47
4. Simulations and Experiments	51
4.1 Cross-GRAPPA	51
4.1.1 Simulation.....	53
4.1.2 Phantom Experiment.....	56
4.1.3 In Vivo Experiments	58
4.1.4 Noise Issue.....	61
4.2 Hybrid-Encoded MRI.....	63
4.2.1 Simulations of GE QA Phantom.....	63
4.2.2 Simulations of Human Brain and Knee	64
4.2.1 Experiments of Phantoms	72
4.2.3 Experiments of Watermelon.....	73
4.2.4 In Vivo Experiments of Human Knee.....	75
4.3 Pseudo 2D Random Sampling	80
4.3.1 Bloch Simulation	80
4.3.2 Simulation of GE QA phantom.....	81
5. Discussions and Future Works.....	83
5.1 Co-registration and 3D Acquisition of Cross-GRAPPA.....	83
5.2 Contrast of Hybrid-Encoded MRI	85
5.3 Co-registration of Pseudo 2D Random Sampling	91
6. Summary.....	92
7. Reference	93
CURRICULLUM VITAE	101

1. Introduction

Magnetic Resonance Imaging (MRI) is one imaging modality based on the Nuclear Magnetic Resonance (NMR) phenomenon. Generally, a magnetic resonance imaging scans use magnetism, radio waves, and computers to produce detailed images of human body inside structures. An MRI scanner is a tube surrounded by a large, powerful magnet. The patient lies on a moveable bed which is placed into the magnet. The magnet generates a strong magnetic field to align the magnetization of some atomic nuclei in the human bodies, usually such as the protons of hydrogen atoms. Then, radio waves are transmitted to alter the equilibrium alignment of the magnetization. After that, the decays of the various proton spins can produce radio waves that are detected by the receivers of the scanners. The radio waves are reconstructed to images by computers. The MR images are quite detailed and good contrast for body structures and can often detect tiny lesions of human bodies.

As one nonionizing radiation technique different with X-rays, Computer Tomography (CT), Single Photon Emission Computed Tomography (SPECT) and Positron Emission Tomography (PET), MRI can achieve true three-dimensional images, remarkable spatial resolution and outstanding soft-tissue contrast [1]. Especially, MRI provides good contrast in imaging the brain, muscles, heart and cancers compared with CT or X-rays, and high resolution compared with PET or SPECT. Although, MRI has many benefits different with other imaging modalities, imaging speed is still one of tough challenges for MRI applications. Some schemes have been proposed to accelerate MR imaging speed, such as Parallel MRI (PMRI), Compressed Sensing (CS), Rapid Imaging, etc. Contemporarily, imaging quality is another tough challenge after accelerating MR imaging. Some derivative schemes are presented to ensure the reconstruction image quality.

1.1 Parallel MRI

1.1.1 Parallel Imaging

Generally, pulse sequences are used to control the image encoding method and data acquisition of MRI scanners. Among the conventional pulse sequences, there are usually four primary pulses and gradients to spatially excite and encode objects in image domain: RF pulses, slice selection gradient (G_z), frequency encoding gradient (G_x), and phase encoding gradient (G_y). As seen as Fig.1, RF pulses excite the protons in objects; slice selection is realized simultaneously with RF pulses; frequency encoding, also called readout, is applied to receive echo signal for data acquisition; phase encoding is applied between excitation and receiving echo, and its gradient value is shifted each Repetition Time (TR). Echo Time (TE) is the time between RF excitation and MR signal sampling, corresponding to maximum echo signals. Sometimes, the 180° RF pulse and the corresponding gradient are applied at the time of TE/2. The acquired data is converted from image space to frequency space (k -space) by mathematical Fourier transformation [2, 3]. As usual, phase encoding, frequency encoding, and slice encoding, of conventional pulse sequences obey Fourier transformation. But sometimes, there is no Fourier encoding along the slice encoding direction if the pulse sequences are not a three dimensional encoding pulse sequence.

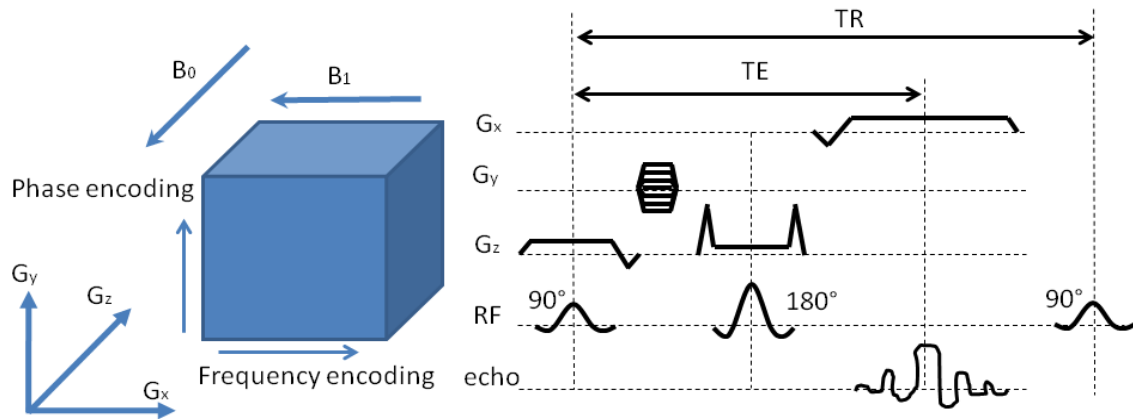


Fig. 1 Conventional encoding method and pulse sequence diagram. The pulse sequence is a traditional spin echo pulse sequence, which is based on repetition of 90° and 180° RF pulses. B_0 field is generated by a very strong magnet; B_1 field is generated by RF coils; B_1 field is much smaller than B_0 field.

Usually, the data acquisition should fill up the k -space, but totally fully sampling is very slow. Because frequency ending steps are much faster than phase ending steps in MRI scanners, one way to accelerate data acquisition is skipping the phase encoding steps by increasing the step length of equidistantly sampled k -space lines. However, the type of undersampled dataset would yield a reduced field of view (FOV), which is equal to fold images along phase encoding direction and yield aliasing artifacts along the underdamped direction as seen as Fig. 2 [4].

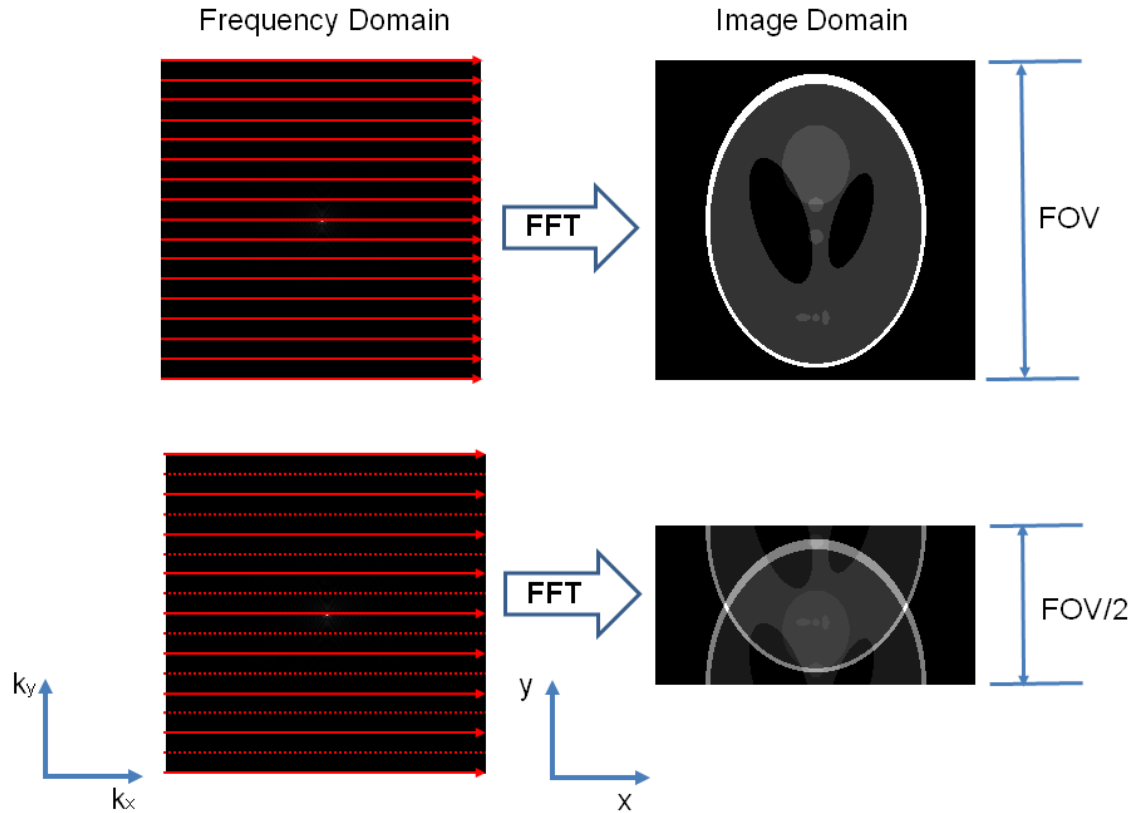


Fig. 2 Comparison of fully sampled acquisition (top row) and undersampled acquisition (bottom row). Fully sampling results a full FOV image after Fourier transformation; undersampled acquisition yields a reduced FOV image with aliasing artifacts. Dot lines mean missing lines; red solid lines are acquired lines. The acceleration factor is 2; FFT means Fast Fourier Transformation.

To short the acquisition time and recover a full-FOV image, PMRI exploits the phased array coils to reconstruct the entire image [5]. The basic idea of PMRI is simultaneously acquiring reduced FOV which covering one part of the entire image by one coil of the receive array coils, and then combine the acquired multiple-coil images to yield the full-FOV image [6]. The actual coil sensitivities extend over the FOV and overlaps, therefore amounts of algorithms are proposed to realize the problem for reconstructing the undersampled raw data in PMRI. Such as, Sensitivity Encoding (SENSE) [7], Partially Parallel Imaging with Localized Sensitivity (PILS) [8], Array

Spatial Sensitivity Encoding Technique (ASSET) [9], Simultaneous Acquisition of Spatial Harmonies (SMASH) [10], Auto Simultaneous Acquisition of Spatial Harmonies (AUTO-SMASH) [11], Variable Density Auto Simultaneous Acquisition of Spatial Harmonies (VD-AUTO-SMASH) [12], Generalized Simultaneous Acquisition of Spatial Harmonies (Generalized-SMASH) [13], Modified Sensitivity Encoding (mSENSE) [14], Sensitivity Profiles from an Array of Coils for Encoding and Reconstruction in Parallel (SPACE RIP) [15], Generalized Autocalibrating Partially Parallel Acquisition (GRAPPA) [16], etc. Among the PMRI algorithms, SENSE and GRAPPA are two representative algorithms.

1.1.2 SENSE

SENSE is the first reconstruction algorithm used for clinical applications. It is considered as an “unfolding” algorithm in image domain [4]. An undersampled acquisition (reduction factor R) results in a reduced FOV in every coil image after Fourier transforming to the image domain. Each pixel in the individual reduced FOV coil image contains information from total R equidistantly distributed pixels in the desired full FOV image ρ . Arbitrary pixel will be weighted with the coil sensitivity C at the corresponding location in the full FOV image. Thus, one folded pixel I_k at a certain location (x, y) received in the k^{th} coil image can be written as [7],

$$I_k(x, y) = \sum_{l=1}^R C_k(x, y_l) \cdot \rho(x, y_l) \quad (1)$$

If Eq. (1) is generalized in matrix notation and the matrix knowledge is applied here, the desired full FOV image ρ can be written as [7],

$$\bar{\rho} = \left(\hat{C}^H \hat{C} \right)^{-1} \hat{C}^H \cdot \bar{I} \quad (2)$$

where, $\hat{\mathbf{C}}$ denotes the sensitivity matrix for each coil at the \mathbf{K} superimposed positions; the vector $\bar{\rho}$ lists the vector of the \mathbf{K} pixels in the desired full FOV image; the vector $\bar{\mathbf{I}}$ represents the folded complex coil image value at the chosen pixel. A detailed description about SENSE is given by Ref. [4] and [7]. Theoretically, SENSE can get an exact solution for the reconstruction of PMRI, but it needs to know coil sensitivities which is hard to be exactly measured in clinic situations. Actually, we usually compute approximate coil sensitivities from pre-scan.

1.1.3 GRAPPA

GRAPPA is another traditional algorithm among PMRI, which is an auto-calibration method in frequency domain [4]. The additional k -space lines in low frequency region, named as auto-calibration signal (ACS) lines, are used to fit the coefficients of linear combinations. Next, the fitting coefficients are applied to estimate the missing k -space data by interpolation of acquired data. Finally, the image is recovered by using sum of squares (SoS) to combine all coil images [5]. Assuming to reconstruct the missing k -space data at the location $(k_x, k_y + m\Delta k_y)$ in coil j , the acquired data in the neighborhood are linearly combined [16]:

$$S_j(k_y + m\Delta k_y) = \sum_{l=1}^L \sum_{b=0}^{N_b-1} n(j, b, l, m) S_l(k_y + b \cdot ORF \cdot \Delta k_y) \quad (3)$$

where ORF represents outer reduction factor; N_b is the number of blocks used in the reconstruction; one block is defined as a single acquired line and its adjacent $ORF-1$ missing lines; $n(j, b, l, m)$ represents the coefficients for the linear combination. The index l counts through the individual coils, while the index b counts through the individual reconstruction blocks. This process is repeated for each coil in the array, resulting in L sets of full k -space data for the uncombined single-coil images. The missing data can be obtained in N_b+1 different ways, which are combined in a weighted average based on the goodness-of-fit (GOF). These images are then

combined using a conventional sum-of-squares (SoS) reconstruction [5]. More detailed descriptions are given by Ref. [4] and [16]. GRAPPA is an approximate scheme to interpolate missing lines in k -space with a linear model, which is different from SENSE that is theoretically an exact scheme. But GRAPPA has no explicit computation of sensitivity maps, not like SENSE. This is the benefit of GRAPPA, comparing to SENSE.

1.2 Compressed Sensing

Compressed sensing/compressive sampling (CS) has emerged as a new sampling theory, different from PMRI. CS allows sparse or compressible signals to be sampled at a rate that is close to their intrinsic information rate and well below their Nyquist rate [17-18]. The CS theory can be summarized into three conditions for applications [19]: (a) Sparsify: the desired signal has a sparse or compressible representation in a known transform domain; (b) Incoherence: undersampled sampling space must generate noise-like aliasing artifacts in the compression transform domain; (c) Nonlinear Reconstruction: a nonlinear reconstruction is required to exploit sparsity/compressibility while maintaining consistency with acquired data. Mathematically, CS reconstruction can be considered to solve the following optimization problem,

$$\mathbf{f}_{\text{opt}} = \arg \min_{\mathbf{f}} \{ \|\Psi \mathbf{f}\|_0 \} \quad s.t. \quad \|\mathbf{b} - \Phi \mathbf{f}\|_2 < \varepsilon \quad (4)$$

where \mathbf{f} is the desired N dimensional signal; \mathbf{f}_{opt} is the optimized desired signal; \mathbf{b} is the measured M dimensional signal, $M \ll N$; Φ is the sensing matrix; Ψ is the sparsifying transform; ε serves as the bound condition (usually noise level). Because minimizing L-0 norm is a non-deterministic polynomial-time hard (NP-hard) problem, L-0 norm is generally substituted by L-1 norm. When the sensing matrix Φ satisfies the restricted isometric property (RIP) condition [17], the desired signal \mathbf{f} can be exactly recovered. Theoretically, the sparsifying transform Ψ and the sensing matrix Φ together determine the acceleration performance, or rather, how many samples can exactly recover the desired signal.

In conventional MRI, the application of compressed sensing is made possible by the facts that (a) most MR images are compressible by certain transforms and (b) the desired image is Fourier encoded in the measurement (so called k -space) which allows incoherent sampling. Such reduced sampling of CS theory is very desirable in MRI because the data acquisition speed is directly related to the amount of data that needs to be acquired. Therefore, CS has been successfully used in conventional Fourier-encoded MRI applications [19-22].

1.3 Benefits and Limitations

Currently, some of PMRI techniques are commercially available. It can generally decrease data acquisition without the need of gradient performances, applying the phase array receiver coils. PMRI techniques have been proved in clinical applications to improve the image quality with increased signal to noise ratio (SNR), spatial resolution, reduced artifacts and the temporal resolution in dynamic MRI scans. Among PMRI techniques, SENSE and GRAPPA are two primary present commercially available techniques. Both techniques are well suited to enhance most of MRI applications. SENSE uses the prescan strategy for perspicuous coil sensitivities; GRAPPA employs the auto-calibration method for receiving coil sensitivities. So the betterments about SENSE mainly focus on how to achieve exact coil sensitivities; the improvements about GRAPPA mostly lie in the auto-calibration method. There are no obvious absolute advantage between SENSE and GRAPPA. Both techniques allow an accelerated image acquisition in arbitrary image plane orientation as well as with arbitrary coil configurations with essentially the same SNR performance, though GRAPPA has a slight advantage than SENSE in inhomogeneous regions with low spin density [4].

Different from PMRI, CS theory is recently a very significant popular advance in signal processing community because of its potential to accelerate signal reconstructions from very

fewer sampled data than conventional sampling by Nyquist-Shannon theory. Although, CS techniques are still being researched and developed further, they have illustrated to increase signal to noise ratio (SNR), and reduce aliasing artifacts. CS reduces the data acquisition depend on sampling below Nyquist rate, which is differ from PMRI accelerating depend on the multiple array receiver coils. CS and PMRI techniques have been mixed together in some research works [21-22]. Among CS theory, the sensing matrix Φ and the sparsifying transform Ψ are two significant factors. They largely influence whether the CS theory can be applied to recover the desire signals and how exactly the CS theory can recover the desire signal. However, they are hard to together achieve optimal settings of Φ and Ψ , under current commercial MRI hardware constrains. Otherwise, sampling pattern also affects the image quality of the reconstruction results, because the real signals from MRI scanners are not so ideal sparse.

1.4 Our Works

Our works include three parts to separately accelerate the MRI data acquisition.

The auto-calibration signal (ACS) lines in conventional GRAPPA are acquired with a frequency-encoding direction in parallel to other undersampled lines [16]. We propose a cross sampling method to acquire the ACS lines orthogonal to the undersampled lines. This cross sampling method increases the amount of calibration data along the direction where k -space is undersampled, and especially improves the calibration accuracy when a small number of ACS lines are acquired. The cross sampling method is implemented by swapping frequency and phase encoding gradients. In addition, an iterative co-registration method is also developed to correct the inconsistency between the ACS and undersampled data which are acquired separately in two orthogonal directions. The same calibration and reconstruction procedure as conventional GRAPPA is then applied to the co-registered data to recover the unacquired k -space data and

obtain the final image. The current results from simulations, phantom and *in vivo* human brain experiments have distinctly demonstrated that the proposed method, named as Cross-GRAPPA [23], can effectively reduce the aliasing artifacts of conventional GRAPPA when very few ACS lines are acquired, especially at high outer reduction factors (ORF).

Since now, CS has been successfully applied to accelerate the data acquisition of the conventional magnetic resonance imaging (MRI) with Fourier encoding [19-22]. However in Fourier encoding, the low spatial frequency always has to be fully sampled such that the high frequency is insufficiently sampled at high acceleration factors, leading to serious loss of resolution. Non-Fourier encoding has been studied in the context of compressed sensing for 2D imaging, but with limited improvement [24-29]. So, we propose a novel 3D acquisition method using hybrid encoding [30]. The method exploits random encoding with a circulant structure matrix along the “phase encoding” direction, while keeping conventional Fourier encoding along the readout and slice encoding directions. A designed 2D random undersampling pattern is used for accelerating the MRI scans according to the characters of the k -space raw dataset. The simulation and experimental results both demonstrate that the proposed schemes preserve much better resolution than the conventional 3D Fourier encoding when the same acceleration factors are applied to accelerate the imaging speeds.

Because the hardware and software constrains of MRI scanners limit the sampling arbitrary in k -space domain, it is very hard to achieve the ideal 2D random sampling pattern [19] with conventional methods to perfectly apply the CS theory. We present a new approach of pseudo 2D random sampling scheme for application of compressed sensing in the Cartesian MRI applications. The proposed scheme is realized by a pulse sequence program which switches the directions of phase encoding and frequency encoding during data acquisition such that both k_x and k_y directions can be undersampled randomly [31]. The resulting random sampling pattern approximates the ideal but impractical 2D sampling patterns. Current simulations and

experiments both show the proposed scheme is superior to the existing 1D random sampling and similar to the ideal 2D random sampling in terms of the image reconstruction quality. This method can potentially improve imaging speed in the CS applications in conventional MRI.

2. Purpose of the Dissertation

The purpose of the dissertation is to improve and accelerate the conventional MR imaging according to constraints of current commercial MRI scanners. The general scans of MR machines typically last 3~5 min to achieve common resolutions [1]. But doctors anticipate to diagnose patients as soon and accurate as possible. Therefore, amounts of the accelerated recon techniques are employed to reduce acquisition and short scan time. These techniques can bring economic benefits for doctors and patients. In the dissertation, three schemes corresponding to PMRI and CS are presented and further developed.

3. Proposed Schemes

Three schemes are proposed to accelerate the image acquisition and improve the image quality. They are Cross-GRAPPA, Hybrid-encoded CS MRI, and Pseudo 2D Random CS MRI. All these schemes are minutely described as follows.

3.1 GRAPPA Using Cross Sampling

GRAPPA scheme [16] has been employed in clinic applications to avoid the estimation of coil sensitivities, which is usually necessary for other approaches such as SENSE [7] and

SMASH [10]. GRAPPA uses a linear combination of the acquired k -space data to reconstruct the missing k -space data. The coefficients used for combination are usually calculated by fitting some acquired auto-calibration signal (ACS) lines. When the number of ACS lines is insufficient, aliasing artifacts of reconstruction are present along the undersampling direction. A number of reconstruction methods have been proposed to reduce aliasing artifacts and improve image quality, such as regularization [32], multicolumn multiline interpolation [33], reweighted least squares [34], high-pass filtering [35], cross-validation [36], iterative optimization [37], virtual coil using conjugate symmetric signals [38], multi-slice weighting [39], infinite impulse response model [40], nonlinear kernel [41].

The way along which ACS data is acquired is actually very important in reconstruction quality. Larger amounts of ACS data usually lead to improve calibration, but on the other hand prolong the imaging time. There have been only few methods modifying the data acquisition procedure to improve GRAPPA. In Ref. [41], it has been noted that the calibration using large ACS in the center of k -space may not be appropriate for reconstructing the missing signals in outer k -space with relatively much smaller amplitude, and a method is proposed to acquire the outer k -space data with different reduction factors and calibrate the GRAPPA coefficients locally. The method is shown to suppress residual aliasing artifacts and noise in GRAPPA when parameters are optimized, but it is not clear how the optimization is done in general.

We first demonstrate that the amount of ACS data needed for reconstruction is not isotropic -- more ACS data are needed along the undersampled phase-encoding direction than the fully sampled frequency-encoding direction to achieve similar reconstruction quality. We then propose a new cross-sampling acquisition method to improve conventional GRAPPA. The method acquires the ACS lines along the direction orthogonal to that of the undersampled lines. By this means, much more ACS data are available along the undersampled direction, and the image quality is thereby significantly improved. To address the “inconsistency” issue usually

encountered in non-Cartesian sampling, we develop an iterative co-registration method to align the reduced data acquired in two orthogonal directions. The same reconstruction procedure of conventional GRAPPA is then applied to the co-registered data for image reconstruction. We name the method cross-sampled GRAPPA (Cross-GRAPPA). Simulation and experimental results using phantom and *in vivo* data demonstrate that the proposed method can significantly reduce the aliasing artifacts in conventional GRAPPA reconstruction with the same number of ACS lines and outer reduction factors (ORFs).

3.1.1 Summary of GRAPPA

In conventional GRAPPA, to reconstruct the missing k -space data at the location $(k_x, k_y + m\Delta k_y)$ in coil j , the acquired data in the neighborhood are linearly combined [16]:

$$S_j(k_y + m\Delta k_y) = \sum_{l=1}^L \sum_{b=0}^{N_b-1} n(j, b, l, m) S_l(k_y + b \cdot \text{ORF} \cdot \Delta k_y) \quad (5)$$

where ORF represents outer reduction factor, N_b is the number of blocks used in the reconstruction, one block is defined as a single acquired line and its adjacent ORF-1 missing lines, and $n(j, b, l, m)$ represents the coefficients for the linear combination. The index l counts through the individual coils, while the index b counts through the individual reconstruction blocks. This process is repeated for each coil in the array, resulting in L sets of full k -space data for the uncombined single-coil images. These images are then combined using a conventional sum-of-squares (SoS) reconstruction [5].

In order to perform the reconstruction in Eq. (5), the coefficients $n(j, b, l, m)$ need to be determined initially. Some ACS lines are acquired with Nyquist rate in parallel to the undersampled k -space lines that are uniformly spaced. The procedure to calculate the coefficients, known as auto-calibration, is described by the following equation:

$$S_j^{ACS}(k_y + m\Delta k_y) \cong \sum_{l=1}^L \sum_{b=0}^{N_b-1} n(j,b,l,m) S_l(k_y + b \cdot ORF \cdot \Delta k_y) \quad (6)$$

where the acquired ACS data $S_j^{ACS}(k_y + m\Delta k_y)$ replaces the missing data $S_j(k_y + m\Delta k_y)$ in Eq. (5). After solving the linear equation Eq. (6), the coefficients $n(j,b,l,m)$ are obtained and slid block-by-block to reconstruct the missing data using Eq. (5). The missing data can be obtained in N_b+1 different ways, which are combined in a weighted average based on the goodness-of-fit (GOF). More ACS lines provide more equations of Eq. (6) and thus improve the coefficient accuracy, but require a longer acquisition time.

3.1.2 Which ACS data are important?

Several parameters of GRAPPA calibration affect the image quality. For example, it is known that more ACS data improves the calibration accuracy and thus the image quality in general. However, the effect of ACS data on reconstruction is neither isotropic nor proportional. Here we use a set of *in vivo* data acquired by an 8-channel head coil to demonstrate: (a) more ACS data barely improve aliasing artifacts beyond a certain threshold; (b) the threshold is larger along the undersampled direction than the fully sampled direction. Three different scenarios were investigated for GRAPPA with an ORF of 4 and the results are shown in Fig. 3. The first row in Fig. 3 shows how the reconstruction quality gradually improves with increasing numbers of ACS rows while all columns are included. It is seen that aliasing reduction saturates at a certain number (about 26) of rows. Beyond this point, the improvement is minimal in aliasing reduction and is primary in SNR enhancement. On the other hand, when the number of ACS rows is well below this point, serious residual aliasing artifacts can be present. Although all columns of ACS data are usually used in GRAPPA reconstruction due to the availability of full samples along the frequency encoding direction, the second scenario exploits only a few columns of the 32 ACS rows in GRAPPA reconstruction. The results on the second row of Fig. 3 demonstrate that

aliasing reduction also saturates at a certain number (about 18) of columns. In the third scenario shown on the third row of Fig. 3, a similar observation is obtained for the extreme case when all 256 rows are available as the ACS data but only a few columns are used for calibration. All results in Fig. 3 suggest that only a small region of ACS data in the central k -space play a key role in calibration. There are usually more ACS data needed along the undersampled direction than the fully sampled direction to suppress the aliasing artifacts. The large number of ACS data along the fully-sampled frequency encoding direction cannot improve the accuracy along the undersampled phase-encoding direction which is critically important in reducing the aliasing artifacts.

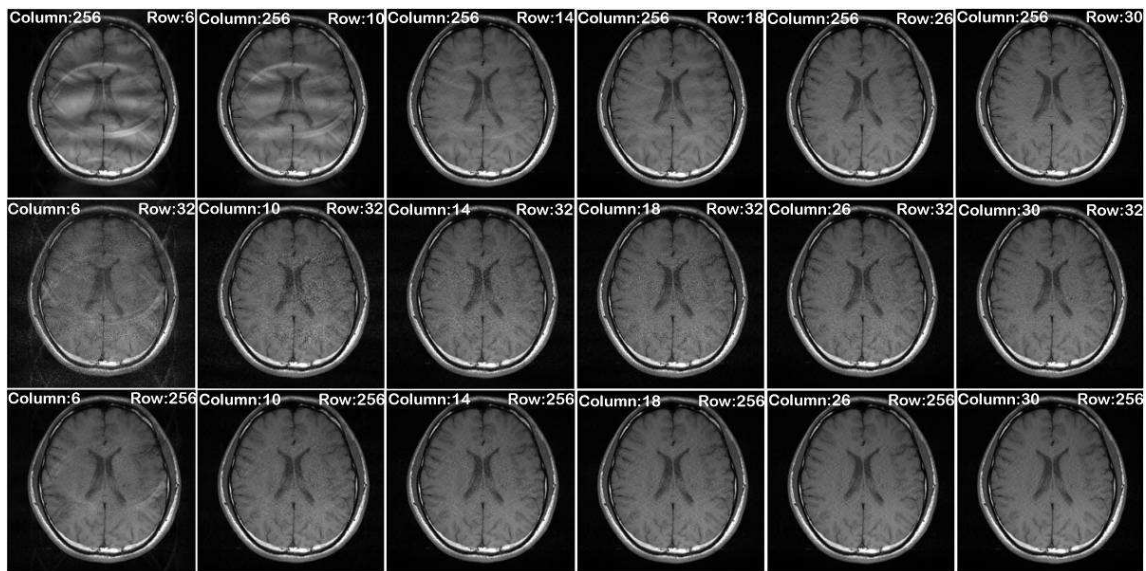


Fig. 3 Conventional GRAPPA reconstructions with different numbers of rows and columns (shown on the top of each image) for ACS data. The results suggest more ACS data are needed along the undersampled direction than fully sampled direction for aliasing-artifacts suppression.

3.1.3 Cross Sampling Method

The contradiction between the demand for a large amount of ACS data along the undersampled direction, and the availability of a large amount of ACS data along the fully-

sampled direction that is not contributing to artifacts reduction, motivates a new method to acquire the ACS lines. The method acquires that the ACS lines are orthogonal to the undersampled lines, as illustrated in Fig. 4(a), such that the amount of ACS data along the undersampled direction is maximized without prolonging the acquisition time. To realize the proposed acquisition method, we simply need to dynamically swap the phase encoding and frequency encoding gradients of a spin-echo or gradient-recalled-echo sequence during the ACS data acquisition such that the frequency/phase encoding direction is changed from one direction (e.g., anterior/posterior) for undersampled acquisition to its orthogonal direction (e.g., right/left) for ACS acquisition as done in Ref. [31]. Fig. 4(b) shows the diagram for a spin-echo sequence used for Cross-GRAPPA. The proposed method is a realistic implementation of the scenario in Fig. 3 last row which acquires a varying number of ACS columns. The results in Fig. 3 last row show in ideal case, the method suppresses aliasing artifacts better than conventional GRAPPA when a small number of ACS lines are used.

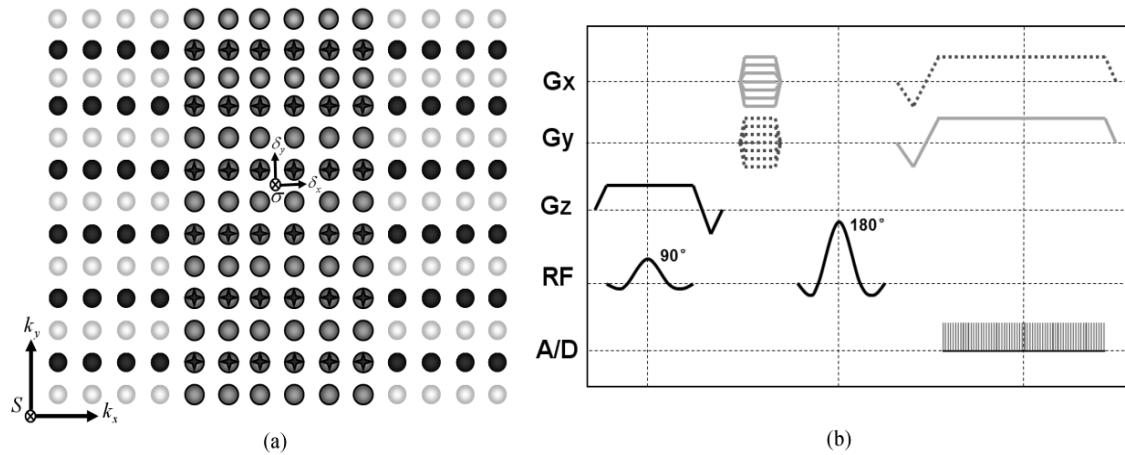


Fig. 4 (a) Sampling pattern of the proposed Cross-GRAPPA method with an ORF of 2, where the solid black dots represent the acquired undersampled data, the gray dots represent the ACS data, and the white dots represent the unacquired data. The black crosses inside the gray dots represent the intersecting locations between the ACS and undersampled data. Parameter δ_x and δ_y are the shifts between the two orthogonal acquisitions along k_x and k_y respectively; σ is a complex scaling

factor. (b) Diagram of a spin-echo pulse sequence for the proposed scheme. The phase and frequency encoding gradients are swapped during the acquisition. The solid gray gradients represent acquisition of the ACS lines and the dash black gradients represent that of the undersampled lines (or vice versa).

3.1.4 Data Co-registration

In practice, the data need to be pre-processed before reconstruction. It is known that when frequency encoding takes different directions, the actual acquired k -space data may not be perfectly consistent due to practical conditions such as eddy current, field inhomogeneities and chemical shift [42-46]. This inconsistency needs to be corrected in Cross-GRAPPA before the assembled data can be used for image reconstruction. A comprehensive correction of the inconsistency is very difficult due to the limited amount of data from two orthogonal directions that are supposed to overlap in k -space. Most correction methods that are used in EPI or PROPELLER [47-50] only work for fully sampled data or require reference scans, and are therefore not applicable here. We are able to correct the inconsistency in k -space rather accurately using a simple model inspired by a PROPELLER correction method used in Ref. [50]. In the model, we assume the two sets of k -space data acquired with orthogonal frequency encodings may be misaligned in position and scaled by a complex constant in value due to practical conditions [23].

To co-register the ACS data and undersampled data that are acquired with orthogonal readout directions, we assume these two sets of data are related by,

$$S_{\text{under}}(k_x + \delta_x, k_y) = \sigma \cdot S_{\text{ACS}}(k_x, k_y - \delta_y), \quad (7)$$

which means the k -space locations can be misaligned (shifted by δ_x along x and δ_y along y as shown in Fig. 4) and the k -space values can be off by a complex scaling factor σ as shown in Fig.

4(a). The complex factor σ is assumed to be $\alpha \cdot e^{-i2\pi\beta}$ with α and β being real numbers. The model in Eq. (7) can also be represented in the image domain as

$$s_{\text{under}}(x, y) e^{i2\pi\delta_x \cdot x} = \sigma \cdot s_{\text{ACS}}(x, y) \cdot e^{-i2\pi\delta_y \cdot y} \quad (8)$$

Because the ACS lines and the undersampled lines with orthogonal readouts intersect at some k -space locations indicated by crosses in Fig. 4 (a), data at these locations can be used to estimate the shifting and scaling parameters in Eq. (7) and thereby used to co-register the k -space data at other locations. To estimate the unknown parameters, the L-1 norm of the total differences between the two sets of data at the intersecting k -space locations is minimized after registration. The problem is formulated as

$$\delta_x, \delta_y, \sigma = \arg \min_{\delta_x, \delta_y, \sigma} \sum |S_{\text{under}}(k_x + \delta_x, k_y) - \sigma \cdot S_{\text{ACS}}(k_x, k_y - \delta_y)| \quad (9)$$

where the summation of the absolute difference is over all intersecting locations of S_{ACS} and S_{under} . Note that L-1 norm is used instead of L-2 norm due to its robustness to outliers that are not adequately characterized in the model in Eq. (7).

To calculate the shift in k -space, we use the image-domain equivalence in Eq. (8). Because the reduced data is fully sampled along the readout direction (assume x), a one-dimensional (1D) Fourier transform is carried out along x and then multiplied with $e^{i2\pi\delta_x x}$, followed by an inverse Fourier transform, i.e.,

$$S_{\text{under}}(k_x + \delta_x, k_y) = \mathcal{F}_x \left[\mathcal{F}_{k_x}^{-1} \left[S_{\text{under}}(k_x, k_y) \right] e^{i2\pi\delta_x x} \right] \quad (10)$$

Similarly, for the ACS data, a 1D Fourier transform is carried out along the fully-sampled readout direction (assume y) and then multiplied by $e^{-i2\pi\delta_y y}$, followed by an inverse Fourier transform:

$$S_{\text{ACS}}(k_x, k_y - \delta_y) = \mathcal{F}_y \left[\mathcal{F}_{k_y}^{-1} \left[S_{\text{ACS}}(k_x, k_y) \right] e^{-i2\pi\delta_y y} \right] \quad (11)$$

where \mathcal{F}_x and \mathcal{F}_y are 1D Fourier transforms along x and y directions in image domain and $\mathcal{F}_{k_x}^{-1}$ and $\mathcal{F}_{k_y}^{-1}$ are 1D inverse Fourier transforms along k_x and k_y directions in k -space.

The above minimization problem is solved using the Nelder-Mead algorithm as in [51, 52]. The Nelder-Mead method [53, 54] is a simplex method for finding a local minimum of a function of several variables. A simplex is a polytope (or generalized triangle) of $N + 1$ vertices in N dimensions. Examples of simplices include a linear segment on a line, a triangle on a plane, a tetrahedron in three-dimensional space and so forth. The method is a pattern search that compares the values of the objective function in Eq. (9) at all vertices of a polytope. The worst vertex giving the largest value of the objective function is rejected and replaced with a new vertex. A new polytope is formed and the search is repeated iteratively. The simplest step is to replace the worst point with a point reflected through the centroid of the remaining N points. If this point is better than the best current point, then we can try stretching exponentially out along this line. On the other hand, if this new point isn't much better than the previous value, then we are stepping across a valley, so we shrink the simplex towards a better point. The iterative process generates a sequence of polytope, for which the size is shrunk and the value of the objective function is reduced. When the polytope is sufficiently small, the coordinates are found to the minimizing point. The Nelder-Mead algorithm is heuristic and can converge to a non-stationary point. It is necessary to properly initialize the parameters for data co-registration. In this study, the initial values of -1 or 1 for δ_x and δ_y and ones for α and β are sufficiently good for all experiments. Although more advanced algorithms are available, we find the method effective and computationally efficient.

3.1.5 Image Reconstruction

After the data from orthogonal directions are co-registered, the same calibration and reconstruction procedure as conventional GRAPPA [16] can be employed to obtain the unacquired data, except that there are much more ACS data for calibration along the undersampled direction, as shown in Fig. 5. Specifically, Eq. (6) is used for the calibration process to estimate the coefficients $n(j,b,l,m)$. The coefficients usually take a size of 4 blocks and 5 columns based on conventional GRAPPA. More coefficients cannot bring more benefits in image quality, and on the contrary will cost more computation time. Eq. (5) is then employed for reconstruction of the missing k -space data using the estimated coefficients from Eq. (6). After the missing data are recovered by a weighted average based on GOF, the reconstructed and acquired data of each coil are then inverse Fourier transformed and combined using a root SoS method [5] to obtain the final desired image. It is worth noting that the image reconstruction step is independent of the proposed cross-sampling scheme. Therefore, all other reconstruction algorithms that improve upon conventional GRAPPA can be applicable in this step.

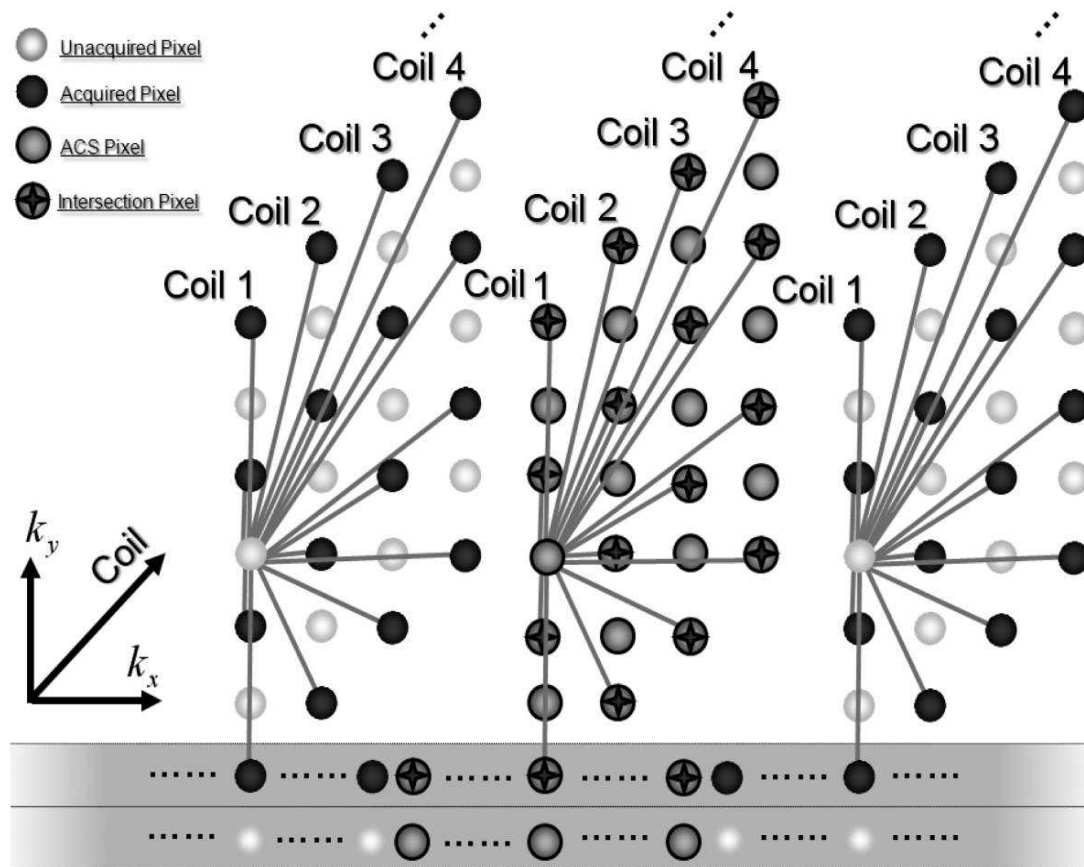


Fig.5 Illustration of Cross-GRAPPA reconstruction procedure with an ORF of 2 and a single column of ACS. Four blocks and one column are assumed for the coefficients. The gray lines represent the process to fit the ACS data (gray dots) in the center or to estimate the unacquired data (white dots) outside the center using undersampled data (solid black dots) from multiple coils. Gray dots with black crosses represent the data points where the ACS and undersampled data intersect. The bottom gray strips show acquisition along the readout direction k_x .

3.1.6 Nonlinear Denoise

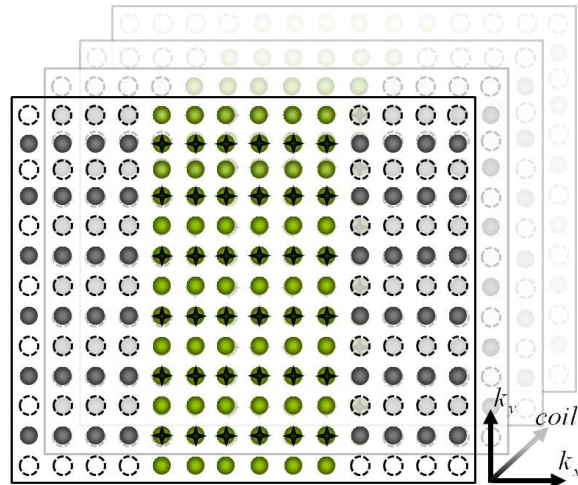
To reduce further noise in reconstruction of Cross-GRAPPA, the proposed method can integrate nonlinear GRAPPA [41] to substitute the conventional linear kernel [16]. Fig. 6 illustrates the procedures of the integration. In data acquisition, the ACS lines are acquired along

the direction orthogonal to that of the undersampled lines (Fig. 6 step 1). By this means, much more ACS data are available along the undersampled direction to improve the calibration accuracy. The previous iterative co-registration method is then used to correct any inconsistency between the data acquired in two orthogonal directions (Fig. 6 step 2). In reconstruction, a nonlinear model [41] is used to represent the relationship between the missing data and the acquired undersampled data (Fig. 6 step 3). Specifically, we have [41],

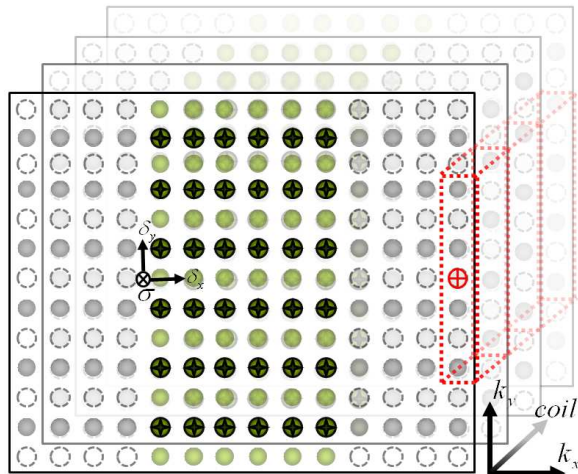
$$\begin{aligned}
S_j(k_y + r\Delta k_y, k_x) = & w_{j,r}^{(0)} \times 1 + \sum_{l=1}^L \sum_{b=B_1}^{B_2} \sum_{h=H_1}^{H_2} w_{j,r}^{(1)}(l, b, h) \times S_l(k_y + bR\Delta k_y, k_x + h\Delta k_x) \\
& + \sum_{l=1}^L \sum_{b=B_1}^{B_2} \sum_{h=H_1}^{H_2} w_{j,r}^{(2,0)}(l, b, h) \times S_l^2(k_y + bR\Delta k_y, k_x + h\Delta k_x)
\end{aligned} \tag{12}$$

where $S_j(k_y + r\Delta k_y, k_x)$ denotes the unacquired k -space signal at the target coil, $S_l(k_y + tR\Delta k_y, k_x + h\Delta k_x)$ denotes the one-order acquired undersampled signal, $S_l^2(k_y + tR\Delta k_y, k_x + h\Delta k_x)$ denotes the second-order acquired undersampled signal, and $w_{j,r}(l, t, h)$ are the coefficients obtained through calibration. The orthogonal ACS lines are used to estimate the coefficients of the nonlinear model. The interpolation is then repeated for each missing point at each coil. These images are then combined by a root sum-of-squares (SoS) method [5] to obtain the final image.

step 1: cross sampling



step 2: co-registration



step 3: nonlinear model

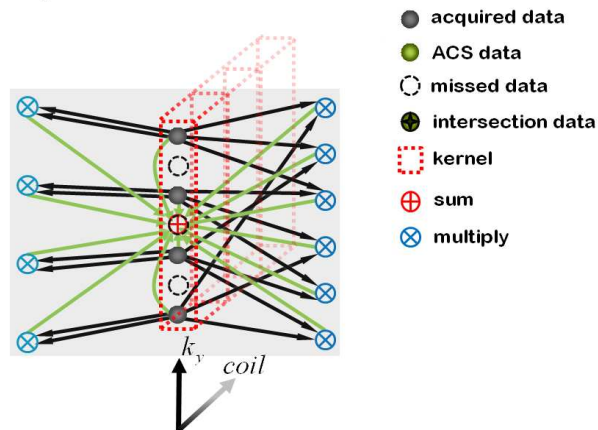


Fig.6 Algorithm procedure illustration of Cross-GRAPPA with nonlinear kernel. The first step is cross sampling the k -space data; the second step is aligning the two orthogonal k -space data; the third step is using nonlinear kernel to calibrate and recover the missed data. The nonlinear terms in Eq. (12) are just yielded from the same coils.

3.2 Hybrid-Encoded MRI Using Compressed Sensing

Among the CS MRI applications [19-22], to accelerate the MR imaging speed, the k -space is undersampled along the directions other than readouts. For example in 2D and 3D Cartesian sampling, a variable density random sampling pattern is used to undersample the k -space data along the phase encoding and slice encoding directions. The image \mathbf{f} can be recovered by solving a constrained convex minimization problem as similar as Ref. [19],

$$\arg \min_{\mathbf{f}} \{ \|\mathbf{b} - \mathbf{F}_u \mathbf{f}\|_2^2 + \lambda_1 \|\mathbf{W}\mathbf{f}\|_1 + \lambda_2 \text{TV}(\mathbf{f}) \} \quad (13)$$

where \mathbf{b} is the measured k -space data; \mathbf{F}_u is the random subset of the rows of the Fourier encoding matrix; \mathbf{W} is the sparsifying transform matrix; $\text{TV}(\cdot)$ is total variation; λ_1 and λ_2 are constant regularization parameters.

Although CS has been demonstrated to accelerate the speed of data acquisition in several Fourier-encoded MRI imaging applications, Fourier encoding may not be optimal for the CS theory, and is known to have some limitations [55, 56]. Firstly, Fourier matrix is known to need more measurement than random matrices for exact recovery. Secondly, Fourier encoding does not spread out the signal energy for natural images, on the contrary, Fourier encoding concentrates the energy in the low-frequency region. Actually, Nyquist sampling is still required in the low-frequency region, which leads to insufficient sampling of high-frequency components at high under-sampling factors. Finally, Fourier encoding is not universal, which is only maximum incoherent with the canonical basis or some spatial wavelet transforms. As a result, the incoherent

condition is weakly satisfied for some sparsifying transforms such as the coarse scale of wavelet transform [55].

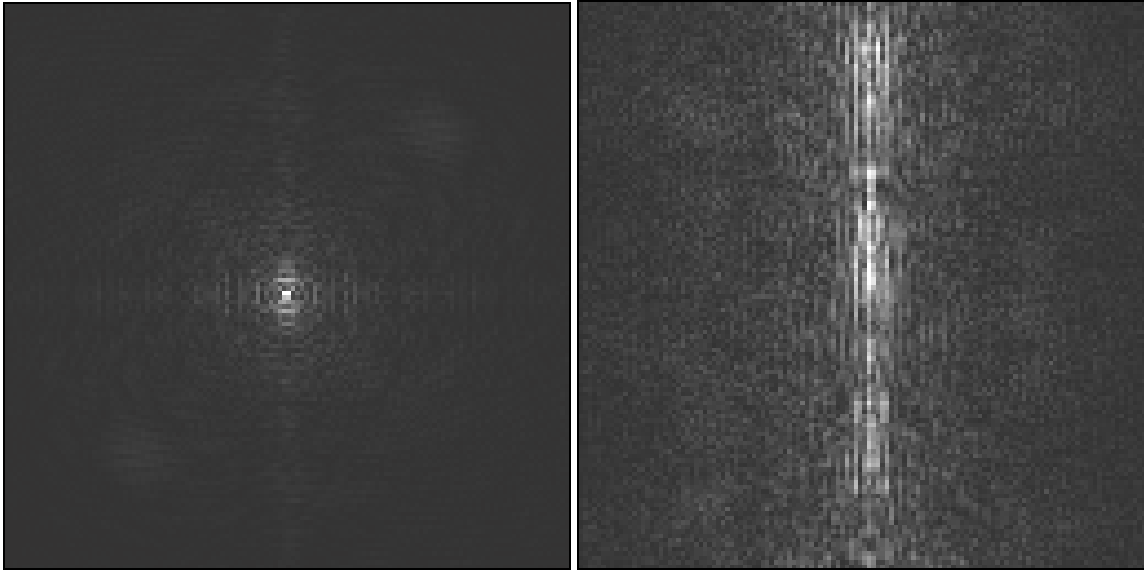


Fig. 7 k -space comparison of Fourier (left) and non-Fourier (right) encoding.

As seen as the Fig.7, the Fourier and non-Fourier (Toeplitz) encodings can generate different k -space raw dataset. For Fourier encoding, the energy in frequency domain is concentrated; the k -space is high coherent; there is high SNR in the low frequency regions and low SNR in the high frequency regions. But, for non-Fourier encoding, the energy in frequency domain is non-concentrated; the k -space is high incoherent; there is homogeneous SNR. Therefore, some people have investigated to use non-Fourier encoding for CS MRI [24-29]. For example, independently identically distributed (i.i.d.) Gaussian random matrices have been proved to have several favorable properties as a CS matrix, such as universal and spread out. It has been studied for MRI as an alternative to Fourier encoding. However, the memory usage and computations are demanding in reconstructing the large-scale 3D image volume. Toeplitz random matrices have

been shown to share similar properties as i.i.d. random matrices, but with more efficient memory usage and computations. 2D Toeplitz random encoding has also been investigated by the authors for CS MRI [25-27]. 2D random excitation [28] shows some promising results. But, a complete 2D random excitation may not be practical, because it requires a very long RF excitation profile for pulse sequences. Spread spectrum MRI [29] is another way to address this issue by a linear chirp modulation instead of the random modulation, which has been implemented physically using a second-order shim coil. The linear chirp is able to spread out the signal energy in the measurement domain. But, this method is constrained by the second-order shim coil and the MPRAG sequence. In sum, none of these existing non-Fourier methods have demonstrated notable improvement over Fourier encoding in real experiments.

We propose a hybrid encoding scheme with a novel pulse sequence [30]. Based on the conventional Fourier pulse sequence, the novel pulse sequence replaces the Fourier encoding along the phase encoding direction by a circulant random encoding. The encoding scheme excites the object along the “phase encoding” direction randomly. This excitation profile is repeated but shifted by a single pixel spatially during each excitation. The corresponding sensing matrix has a circulant structure with independent random complex elements. With the proposed hybrid encoding scheme, the benefits of both Fourier encoding and random encoding can be achieved simultaneously. The low frequency signal can still be densely sampled in the Fourier encoding direction for high SNR. At the same time, the signal energy is more spread out in the circulant random encoding direction such that high-frequency information is adequately sampled. Using both simulation and real experiments, we demonstrate that hybrid encoding under 3D encoding is superior to 3D Fourier encoding in preserving resolution at the same reduction factors.

3.2.1. Compressed Sensing

Compressed Sensing /compressive sampling (CS) theory [17, 18] is employed to reconstruct a signal which is sparse or compressible in multi-scale bases, such as wavelet bases. In the CS

theory, the desire signal is a length- N signal vector: $\mathbf{f} \in \mathbf{C}^N$; the measurement: $\mathbf{b} \in \mathbf{C}^M$ is a length- M measurement vector; the matrix: $\mathbf{E} \in \mathbf{C}^{M \times N}$ is the encoding matrix with $M \ll N$, and the vector: $\boldsymbol{\eta} \in \mathbf{C}^M$ is a length- M noise vector. The measurement model satisfies:

$$\mathbf{b} = \mathbf{E}\mathbf{f} + \boldsymbol{\eta}, \text{ with } \mathbf{E} = \mathbf{\Phi}\mathbf{\Psi} \quad (14)$$

where the matrix $\mathbf{\Psi}$ is a sparsifying transform matrix. The basic CS reconstruction $\hat{\mathbf{f}}$ of desire signal \mathbf{f} is solving an L-1 minimization problem:

$$\hat{\mathbf{f}} = \arg \min_{\mathbf{f} \in \mathbf{C}^N} \|\mathbf{\Psi}\mathbf{f}\|_1, \text{ s.t. } \|\mathbf{b} - \mathbf{E}\mathbf{f}\|_2^2 \leq \boldsymbol{\varepsilon} \quad (15)$$

where the L-1 norm and L-2 norm are respectively defined as $\|\mathbf{x}\|_1 = \sum_i |\mathbf{x}_i|$ and $\|\mathbf{x}\|_2 = \sqrt{\sum_i |\mathbf{x}_i|^2}$ for all k -sparse vector $\mathbf{x} \in \mathbf{R}^N$; the $\boldsymbol{\varepsilon}$ is the noise level of the noise vector $\boldsymbol{\eta}$. The desire signal \mathbf{f} can be exactly and stably recovered by the CS reconstruction, if the matrix $\mathbf{\Phi}$ satisfies restricted isometric properties (RIPs) [17]. Theoretically, the measurement matrix $\mathbf{\Phi}$ has restricted isometric properties of order K if the inequality is satisfied,

$$(1 - \boldsymbol{\delta}_k) \|\mathbf{x}\|_2^2 \leq \|\mathbf{\Phi}\mathbf{x}\|_2^2 \leq (1 + \boldsymbol{\delta}_k) \|\mathbf{x}\|_2^2 \quad (16)$$

for all K -sparse (length- K of nonzero) signals \mathbf{x} . The RIP condition does not hold for $K < M$, but it may hold for smaller K . Actually, the RIP condition is a stable embedding. If $\boldsymbol{\delta}_{2k} < \sqrt{2} - 1$, then for all k -sparse vector \mathbf{x} such that $\mathbf{\Phi}\mathbf{x} = \mathbf{b}$, the L-1 solution is equal to the L-0 solution [19]. And if $\boldsymbol{\delta}_{2k}$ have injectivity; smaller $\boldsymbol{\delta}_{2k}$ more stable. If the noise level

$\|\boldsymbol{\eta}\|_2 \leq \boldsymbol{\varepsilon}$ and $\boldsymbol{\delta}_{2k} < \sqrt{2} - 1$, then,

$$\|\mathbf{x}^* - \hat{\mathbf{x}}\|_2 \leq C_0 \cdot k^{-1/2} \boldsymbol{\sigma}_k(\hat{\mathbf{x}})_1 + C_1 \cdot \boldsymbol{\varepsilon} \quad (17)$$

where \mathbf{x}^* is the L-1 solution; $\hat{\mathbf{x}}$ is the proposed k -sparse vector; and

$\boldsymbol{\sigma}_k(\hat{\mathbf{x}})_1 = \min_{\mathbf{z} \in \Sigma_k} \|\hat{\mathbf{x}} - \mathbf{z}\|_1$ where $\mathbf{z} \in \Sigma_k$ that is [19],

$$\#\text{supp}(\mathbf{x}) \leq k . \quad (18)$$

For an arbitrary pair of matrices \mathbf{E} and $\mathbf{\Psi}$, it is often computationally infeasible to calculate practically-useful guarantees on the quality and robustness of the CS reconstruction [24]. The known reconstruction bounds for matrices with entries drawn at random from various probability distributions is,

$$k \leq C \cdot M / \log(N / M) \quad (19)$$

Usually, it is difficult to verify RIP for a given matrix \mathbf{E} , and requires checking eigenvalues of each sub-matrix of the matrix \mathbf{E} . The random matrices \mathbf{E} , such as i.i.d. Gaussian entries, i.i.d. Bernoulli entries, i.i.d. sub-Gaussian entries, random Fourier ensemble, random subset of incoherent dictionary, Toeplitz, etc., have been proved to satisfy RIP condition. If $\mathbf{\Psi}$ is an identity matrix, M and N are large, then CS reconstruction is guaranteed to be robust with high probability if the matrix \mathbf{E} is a randomly under-sampled discrete Fourier transform operator [17-19, 24]. However, Fourier encoding is not necessarily well suited to CS reconstruction with arbitrary $\mathbf{\Psi}$ [24]. Practically, the SNR of readout cannot be uniform for measuring instruments. As a result, the use of non-Fourier encoding schemes for CS-MRI could also potentially yield benefits [24].

3.2.2. Circulant random matrices

Although i.i.d random matrices have been proved to satisfy the restricted isometry property (RIP) condition [17], the computation and memory usage are expensive for reconstructing MR images. Toeplitz and circulant matrices haven been shown to be almost as effective as the i.i.d. Gaussian random matrices in the context of CS, but require a significant reduction in computation

and storage [57-61]. In particular, a circulant matrix \mathbf{C} is a special Toeplitz matrix and has the form,

$$\mathbf{C} = \begin{pmatrix} h_1 & h_2 & \cdots & h_n \\ h_n & h_1 & \cdots & h_{n-1} \\ \vdots & \vdots & \ddots & \vdots \\ h_2 & h_3 & \cdots & h_1 \end{pmatrix}, \quad (20)$$

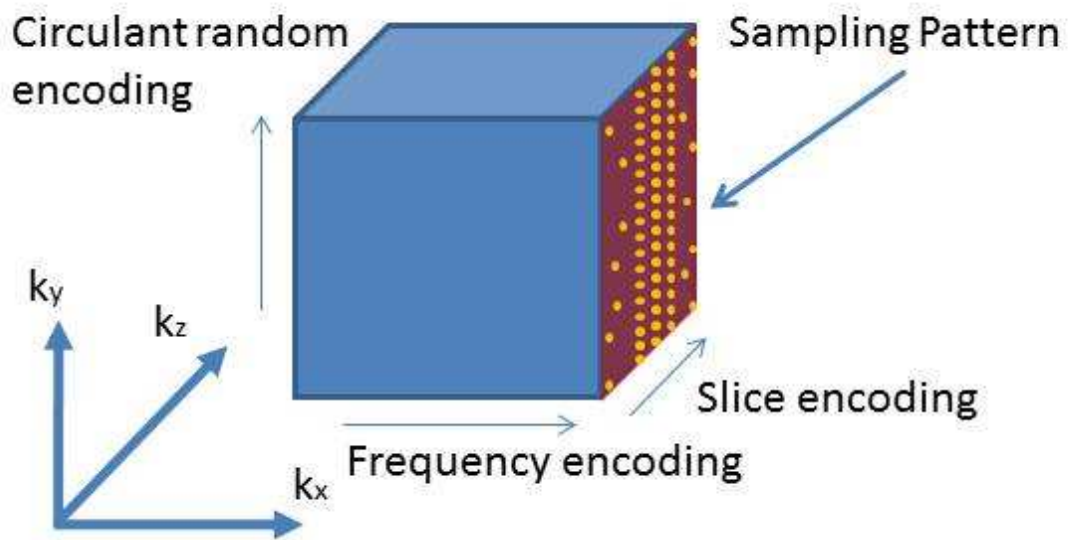
where h_1, h_2, \dots, h_n are the complex numbers and n is the size of matrix. This matrix \mathbf{C} is known to be decomposed into $\mathbf{C} = n^{-1/2} \mathbf{F}_1^* \mathbf{\Sigma} \mathbf{F}_1$, where the matrix \mathbf{F}_1 expresses the 1D Fourier matrix, and $\mathbf{\Sigma} = \text{diag}([\sigma_1, \sigma_2, \dots, \sigma_n])$ is a diagonal matrix whose non-zero entries are the 1D Fourier transform of vector $h = [h_1, h_2, \dots, h_n]$. Such a decomposition suggests that multiplication of the circulant matrix \mathbf{C} with one signal x (equivalent to circular convolution) can be efficiently calculated by a point-wise production of two length- n vectors in the Fourier domain. A fast algorithm for CS reconstruction has also been developed for circulant measurements based on this property [61]. Here, in our design, σ_i 's are chosen as complex numbers with uniform magnitudes and random phases which is uniformly distributed on $[0, 2\pi]$. Such a choice can further reduce computation, and guarantee to generate the enough excitations to decrease aliasing artifacts. When the raw data are reconstructed, a linear matrix equation is mainly solved. The equation is given: $\mathbf{C}x = b$, where \mathbf{C} is a circulant square matrix of size $N \times N$. Usually, we can solve this equation with the inverse matrix of \mathbf{C} , $x = \mathbf{C}^{-1}b$, but its computation is very slow which needs to calculate the inverse matrix of \mathbf{C} and Gaussian elimination. Because \mathbf{C} is a circulant square matrix, we also can solve this equation with the transposition matrix of \mathbf{C} , $x = \mathbf{C}^T b$, but it also needs to calculate Gaussian elimination. However, we can write the equation as the circulant convolution $c * x = b$, where c is the first column of \mathbf{C} , and the vector c , x and b are cyclically extended in each direction. Using the results of the circular

convolution theorem, we can use the discrete Fourier transform to transform the cyclic convolution into component-wise multiplication $F_n(c * x) = F_n(c)F_n(x) = F_n(b)$, so that, to solve the equation $Cx = b$ can become calculating, $x = F_n^{-1} \left[\left(F_n(b)_v / F_n(c)_v \right)_{v \in Z_g} \right]^T$ [62], where Z_g is a cyclic group. If the fast Fourier transform is used, this algorithm is much faster than the standard Gaussian elimination. If the sizes of x , c and b are all N , the computational complexity of this algorithm is $O(N \log N)$. If the raw dataset is a three-dimensional k -space data, this algorithm is used to decode circulant random encoding along one direction and the fast Fourier transform is applied along the other two directions. Here, we assume that the size of the fully-sampled data is $N \times N \times M$ along X , Y and Z directions. If the data size is a cube dataset, M is equal to N ; otherwise M is less than N . The computational complexity of the proposed method for this 3D k -space data is $O(MN^2 \log N)$, which is comparable with the computational complexity of the inverse fast Fourier transformation (IFFT), $O(MN^2 \log N)$. Therefore, the decoding computational complexity of the proposed method is the same as the conventional Fourier-encoded method.

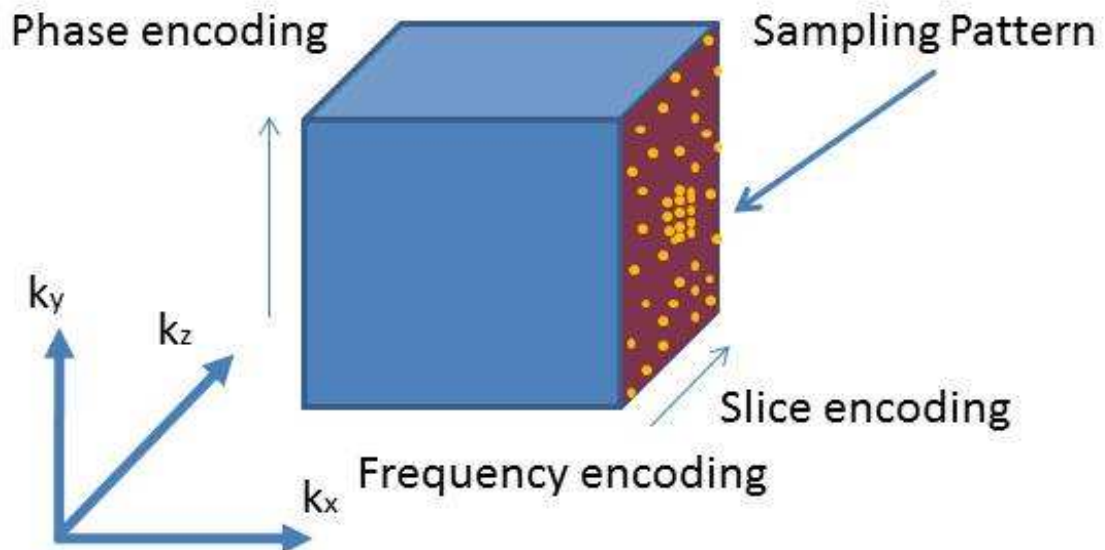
3.2.2. Hybrid Encoding Scheme

Our objective is to design one MR physical-implementable hybrid encoding scheme for 2D and 3D imaging which are superior to the conventional Fourier encoding in the CS reconstruction framework. Actually, the commercial MRI hardware constraints always require fully sampling along readout directions, hence we cannot undersample in k -space to accelerate the image reconstruction along the readout direction. Therefore, to implement the proposed non-Fourier encoded method, we mix the expected Circulant random encoding and the conventional Fourier encoding in 2D imaging to achieve 1D accelerations and 3D imaging to achieve 2D accelerations.

Otherwise, in the CS reconstruction framework, 2D Hybrid-encoded imaging cannot be compared with the 2D Fourier-encoded imaging under the fair sampling situations of the low and high frequency domains, as seen as Fig.8. And only 3D Hybrid-encoded imaging (a) can ensure the fair sampling situations comparing to the 3D Fourier-encoded imaging (b). Therefore, we just discuss the 3D imaging of Hybrid and Fourier encoding.



(a)



(b)

Fig.8 Illustration of the sampling acquisitions of the 3D Hybrid encoding (a) and 3D Fourier encoding (b) methods. The sampling patterns of Hybrid and Fourier are separately based on the characters of the raw k -space datasets. Without loss of generality, X is assumed to be the readout, Y is assumed to be the circulant random encoding or phase encoding, and Z is assumed to be the slice encoding. The undersampling is in the k_y - k_z plane of k -space. Hybrid has a variable density random sampling is used along the k_z direction, and a uniform random sampling is along the k_y direction. Fourier encoding has a variable density random sampling is used along the k_z direction, and a variable random sampling is along the k_y direction.

As the CS reconstruction of the 3D Fourier-encoded imaging, the CS reconstruction of the 3D Hybrid-encoded imaging is also in the Y-Z plane for under-sampled raw k -space datasets per slice along the X direction, because the raw k -space data along X direction which usually is the readout direction must be fully sampled. Assuming the vectored image to be reconstructed in the Y-Z plane as \mathbf{f} , the encoding matrix \mathbf{H} can be written as the Kronecker product of a circulant random matrix (i.e., \mathbf{C} in Eq. (20)) and a 1D Fourier transform matrix. The matrix \mathbf{H} has a block circulant structure with each block being a Fourier transform matrix. The original vectored image \mathbf{f} , can be reconstructed from the undersampled data \mathbf{b} by solving,

$$\arg \min_{\mathbf{f}} \{ \|\mathbf{b} - \mathbf{H}_u \mathbf{f}\|_2^2 + \lambda_1 \|\mathbf{W}\mathbf{f}\|_1 + \lambda_2 \text{TV}(\mathbf{f}) \} \quad (21)$$

where all notations are the same as in Eq. (13) except that the Fourier matrix \mathbf{F} is replaced by the circulant-Fourier encoding matrix \mathbf{H} ; \mathbf{H}_u is the subset matrix of the circulant-Fourier encoding matrix \mathbf{H} ; \mathbf{W} is the wavelet transform matrix; $\text{TV}(\cdot)$ is total variation; λ_1 and λ_2 are constant regularization parameters; $\|\cdot\|_1$ is the L-1 norm and $\|\cdot\|_2$ is the L-2 norm. To solve the optimized problem, nonlinear conjugate gradient method is applied to minimize the target function in the Eq.

(31). Actually, there are still some methods [61, 62] used to accelerate the image reconstructions because of the special property of the Toeplitz structure.

3.2.3. Pulse Sequence Design

According to the MR physics of magnetization with small tip angles [63], the excitation profile should satisfy the following equation, when the situation of the small tip angles,

$$M(\mathbf{r}) = j\gamma M_0(\mathbf{r}) \int_0^T B_1(t) e^{j\mathbf{k}(t) \cdot \mathbf{r}} \cdot dt . \quad (22)$$

where, γ is the gyromagnetic ratio; \mathbf{r} is a unit vector in the k -space; $B_1(t)$ is a magnetic field created from an RF coil which oscillates at the Larmor frequency; $M_0(\mathbf{r})$ is the initial equilibrium magnetization, usually along Z direction; $M(\mathbf{r})$ is the nuclear magnetization; $\mathbf{k}(t)$ is a trajectory in k -space, which is usually the area of the remaining gradient,

$$\mathbf{k}(t) = \frac{\gamma}{2\pi} \int_t^T \mathbf{G}(\tau) d\tau . \quad (23)$$

Where $\mathbf{G}(\tau)$ is the gradient vector in the pulse sequences, which usually should satisfy the equation, $\mathbf{G}(t) = [G_x(t) \quad G_y(t) \quad G_z(t)]^T$.

The Eq.(22) means that $B_1(t)$ can satisfy the Fourier transform at small tip angles, whatever the random pulse or other. But at the large tip angles, this Fourier transform cannot be exactly guaranteed. Usually, they are the small tip angles when the tip angles are not over 30° ; otherwise, they are the larger tip angles [64-69]. But this conclusion is just drawn from the conventional SINC pulse as the RF pulses which have the constant flip angles. The random pulse as the RF pulses do have variant flip angles instead of the constant flip angles, which only have the

conception of the average flip angles. Whatever, $B_1(t)$ should be less than an upper bound for satisfying the Fourier transform, and also larger than a lower bound for gaining the cognizable signal over background noise. Therefore, in terms of experimental experiences, the maximum amplitude of $B_1(t)$ should be the 1/4~1/3 of the maximum amplitude of 90° RF pulses.

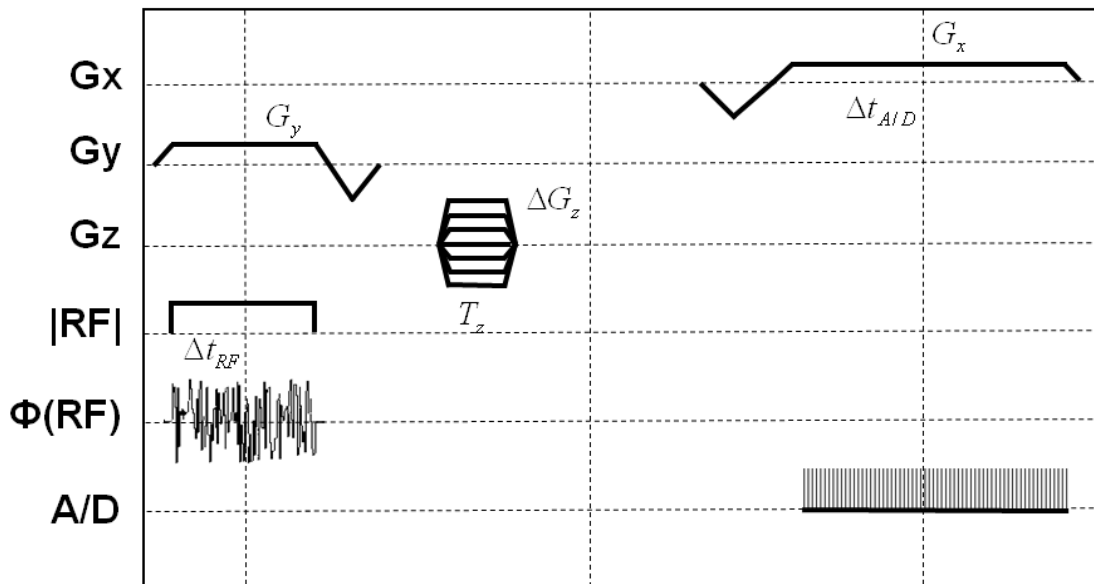


Fig. 9 Timing diagram of the pulse sequence for the proposed 3D hybrid encoding scheme. The RF pulses are complex numbers with uniform magnitudes and random phases. G_y is turned on simultaneously as the RF pulses. After the RF excitation, the slice encoding gradient G_z is turned on along z followed by the readout gradient G_x along x .

The pulse sequence designed for the proposed circulant random encoding is shown in Fig. 9. Specifically, a random pulse with a constant magnitude and random phases after Fourier transformation is applied as the excitation profiles of the RF pulses. Each random RF pulse generates a random excitation profile along the Y direction. Along Y direction, a fixed gradient G_y is turned on to generate random flip angles along the Y direction. To construct the circulant

structure for the random encoding, a linear phase shift is applied in image domain at subsequent excitations. The linear phase shift is designed such that the excitations from consecutive excitations are spatially shifted by a single pixel along the Y direction.

Each excitation corresponds to a row of the circulant random encoding matrix \mathbf{C} in Eq. (20). As seen on Fig. 8, the amplitudes and phases are shifted, TR by TR, to implement circulant random encoding along Y axis. In general, a B_1 field applied on-resonance for a finite time is called an ‘RF pulse.’ The RF excitation will allow controlling the magnetization vector. If the simplest envelop is a rectangular pulse with the amplitude B_1 and the duration τ_p , yielding a simple RF burst. In the rotation frame, the B_1 filed generated by the RF excitation is given by, $B_1(t) = B_1^e(t) e^{j\varphi}$. Here, $B_1^e(t)$ is the envelop of $B_1(t)$ and φ is its initial phase. The final tip angle α after an RF excitation pulse of the duration τ_p is given by

$$\alpha = \gamma \int_0^{\tau_p} B_1^e(t) dt, \quad (24)$$

if assuming the initial phase $\varphi = 0$. For the special case of a rectangular, the tip angle is $\alpha = \gamma B_1 \tau_p$. However, the final tip angle α after an RF excitation pulse of the duration τ_p for random encoding cannot be calculated directly. If $B_1(t)$ are real numbers, the tip angle α can be calculated by the Eq. (24). For example, the root mean square flip angle [24] can be computed as the tip angle α . However, if $B_1(t)$ are complex numbers, the final tip angle α cannot be calculated by the Eq. (24) after an RF excitation pulse of the duration τ_p . So the simulation with the Bloch equations [1, 43, 66, and 84] should be applied to calculate the final tip angle α . The Bloch simulation shows that the final tip angle α is variant each TR, different from the constant tip angle α of Fourier encoding.

After the RF excitation, the slice encoding gradient G_z is still turned on along Z axis followed by the readout gradient G_x along X axis. If assuming the field of view FOV_f of readout, the gyromagnetic ratio γ and the bandwidth BW for the receiver digitizer, the amplitude G_x of the G_x gradient is equal to,

$$G_x = \frac{BW}{\gamma FOV_f}. \quad (25)$$

If an isotropic cubic FOV, the gradients should satisfy the following equation,

$$G_y \Delta t_{RF} = G_x \Delta t_{readout} = \Delta G_z T_z. \quad (26)$$

For a non-isotropic cubic FOV, such as the data size of $X \times Y \times Z$ is $256 \times 256 \times 32$, the gradients are designed depend on the corresponding scalar size per voxel. Here, G_y is the amplitude of G_y gradient along Y direction; G_x is the amplitude of G_x gradient along X direction; ΔG_z is the variant amplitude of slice ending along Z direction; Δt_{RF} and $\Delta t_{readout}$ are the durations of RF excitation and readout acquisition, and T_z is the duration of G_z gradient. Usually, Δt_{RF} is a constant value which satisfies the multiple of the data size along Y direction, and G_x has been calculated by the Eq. (25). Here, $\Delta t_{readout}$ satisfies $\Delta t_{readout} = 1/BW$, thus G_y can be calculated by the Eq. (26). It means that if hoping to raise the amplitude of the gradient G_y , rBW should be decreased. Otherwise, if decreasing G_y , rBW should be increased.

As seen as Fig.10, to realize 2D imaging, we have demonstrated the feasibility of Toeplitz random encoding in 2D imaging using MR experiments in our prior work [26, 27]. For 2D hybrid-encoded imaging the sequence is realized as the Fig. 4, which is based on spin echo pulse sequence and has the 180° RF pulse to implement the slice selection along Z direction. There is a corresponding gradient simultaneously with the 180° RF pulse along Z direction. To guarantee the signal quality of readout, the two crushers should be applied because the 180° RF pulse may

not be exactly 180° , and it may not refocus everything at time TE as we expect. The crusher gradient after the 180° RF pulse destroys the free induction decay (FID), the one before the 180° RF pulse is to balance the one after. Otherwise, especially for reconstruction, it will change the shift direction of the encoding matrix \mathbf{C} , if the 180° RF pulse is added into the pulse sequence. Because, the 180° RF pulse reverses the magnetization vector direction in the transverse plane, the reverse circulant shifting direction of the encoding matrix \mathbf{C}^* should be equal to,

$$\mathbf{C}^* = \begin{pmatrix} h_1 & h_2 & \cdots & h_n \\ h_2 & h_3 & \cdots & h_1 \\ \vdots & \ddots & \ddots & \vdots \\ h_n & h_1 & \cdots & h_{n-1} \end{pmatrix}. \quad (27)$$

where h_1, h_2, \dots, h_n are the complex numbers and n is the matrix size, which is the actual image size along the Y direction.

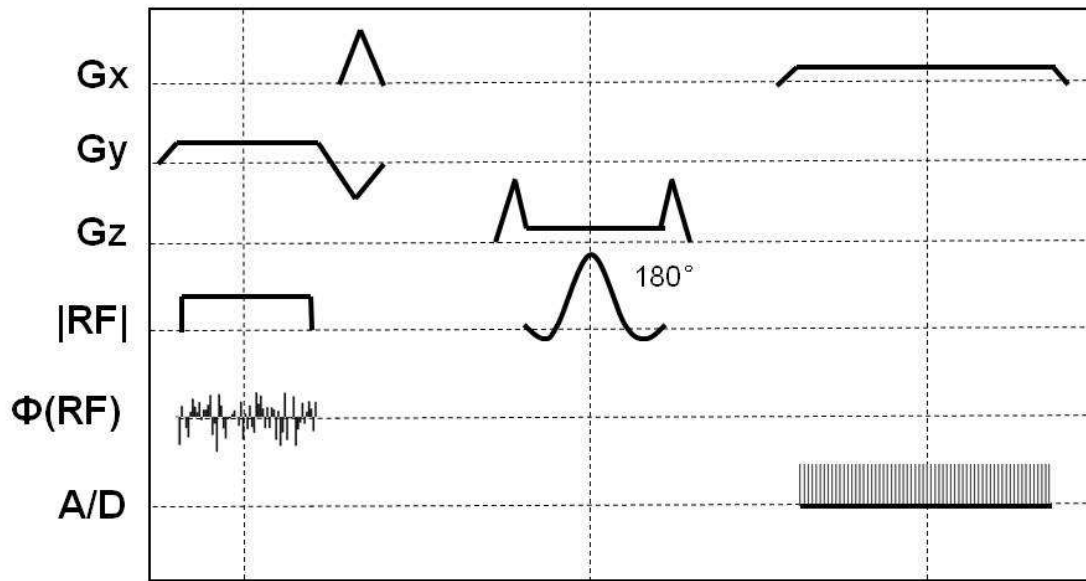


Fig. 10 Timing diagram of the pulse sequence for the proposed 2D hybrid encoding scheme. It's based on spin echo pulse sequence and has the 180° RF pulse to implement the slice selection along Z direction. There is a corresponding gradient simultaneously with the 180° RF pulse along Z direction. There are two crusher gradients to destroy the free induction decay (FID).

3.2.4. Bloch Equation Simulation

The Bloch equations are a set of macroscopic equations that are used to calculate the nuclear magnetization in the classical nuclear magnetic resonance (NMR). Because its solution includes T1 and T2 relaxation time and precession, its simulation is the most accurate way to study the effect of pulse sequence on magnetization. These phenomenological equations were introduced by Felix Bloch in 1946 [85]. Here T1 is the spin-lattice relaxation time, and various tissues with the body have different T1 values; T2 is the spin-spin relaxation time, and various tissues with the body have different T2 values; usually, T1 is larger than T2. If assuming that $\mathbf{M}(t)$ is the nuclear magnetization which should satisfy the equation, $\mathbf{M}(t) = [M_x(t) \ M_y(t) \ M_z(t)]^T$ and $\mathbf{B}(t)$ is the magnetic field which should satisfy the equation $\mathbf{B}(t) = [B_x(t) \ B_y(t) \ B_z(t)]^T$, then the Bloch equations are as follows:

$$\begin{cases} \frac{dM_x(t)}{dt} = \gamma(\mathbf{M}(t) \times \mathbf{B}(t))_x - \frac{M_x(t)}{T_2} \\ \frac{dM_y(t)}{dt} = \gamma(\mathbf{M}(t) \times \mathbf{B}(t))_y - \frac{M_y(t)}{T_2} \\ \frac{dM_z(t)}{dt} = \gamma(\mathbf{M}(t) \times \mathbf{B}(t))_z - \frac{M_z(t) - M_0}{T_1} \end{cases}, \quad (28)$$

where γ is the gyromagnetic ratio and $\mathbf{M}(t) \times \mathbf{B}(t)$ is the cross product of $\mathbf{M}(t)$ and $\mathbf{B}(t)$. M_0 is the steady state nuclear magnetization when $t \rightarrow \infty$. The Eq. (28) is for the Larmor precession of the nuclear magnetization $\mathbf{M}(t)$ in the external magnetic field $\mathbf{B}(t)$. The relaxation terms which are the established physical processes of transverse and longitudinal relaxation of nuclear magnetization $\mathbf{M}(t)$, are equal to,

$$\left(-\frac{M_x}{T_2} \quad -\frac{M_y}{T_2} \quad -\frac{M_z - M_0}{T_1} \right). \quad (29)$$

According to the Eq. (28), there are spin-lattice and spin-spin relaxation. Spin-lattice relaxation is the mechanism by which the z component of the magnetization vector comes into thermodynamic

equilibrium with its surroundings (the "lattice"). It is characterized by the spin-lattice relaxation time, named as T1. Spin-spin relaxation is the mechanism by M_{xy} which is $M_{xy} = M_x + jM_y$, the transverse component of the magnetization vector, exponentially decays towards its equilibrium value of zero. It is a time constant characterizing the signal decay, named as T2.

Therefore, according to the different measurement requirements, there are T1 weighted, T2 weighted scans, T2* weighted scans and proton density weighted scans using different TE and TR parameters on different pulse sequences. T1 weighted scans refer to a set of standard scans. T1 weighted images can be obtained by setting short TR (TR<750ms) and TE (TE<40ms) values in conventional SE sequences, while in GRE Sequences they can be obtained by using flip angles of larger than 50° while setting TE values to less than 15ms. T2 weighted scans are another basic type. T2 weighted images can be obtained by setting long TR (TR>1500ms) and TE (TE>75ms) values in conventional SE sequences, while in GRE sequences they can be obtained by using flip angles of less than 40° instead of 90° while setting TE values to above 30ms. T2* weighted scans use a GRE sequence, with long TE and long TR. Proton density weighted scans try to have no contrast from either T2 or T1 decay, the only signal change coming from differences in the amount of available spins (hydrogen nuclei in water). It uses a SE or sometimes a GRE sequence, with short TE and long TR.

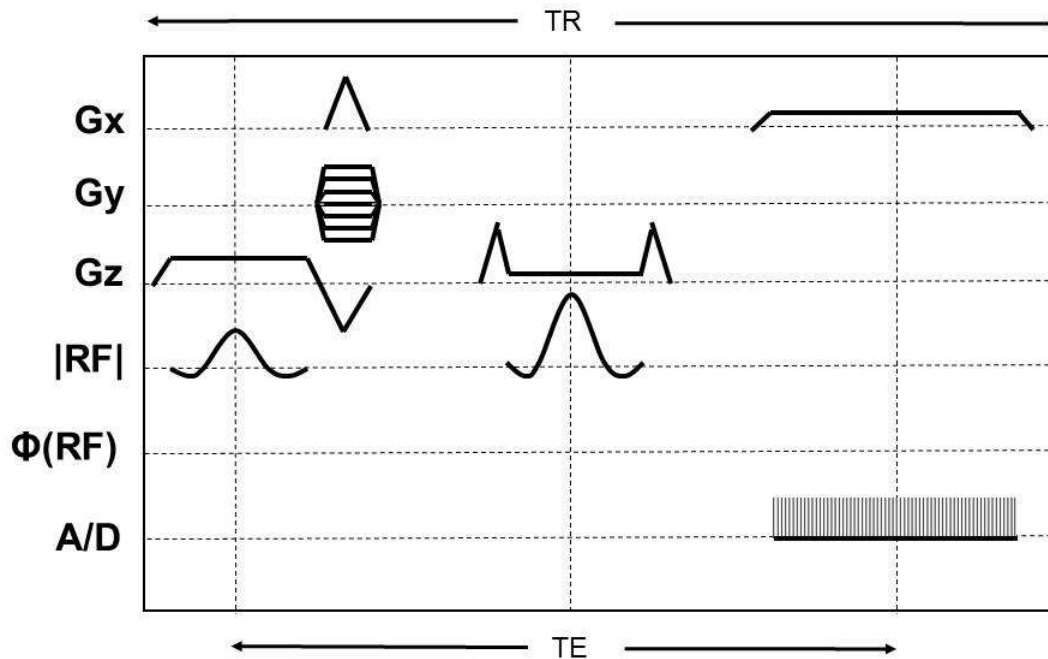


Fig. 11 Timing diagram of the traditional SE pulse sequence. The SE sequence has a steady-state magnetization. And the SE sequence has a 90-degree excitation and a 180-degree refocusing pulse that is $TE/2$ after the 90-degree pulse sequence.

The SE sequence is the most commonly used pulse sequence in clinical imaging, as seen as Fig.11. The SE sequence which has a steady-state magnetization, consists of two radiofrequency pulses, a 90-degree excitation and a 180-degree refocusing pulse that is $TE/2$ after the 90-degree pulse sequence. With each repetition, a k -space line is filled with a different phase encoding. The 180° rephasing pulse eliminates field inhomogeneity and chemical shift effects at the echo to obtain an echo that is weighted in T_2 and not in T_2^* . Proper selection of the TE time of the pulse sequence can help to control the amount of T_1 or T_2 contrast present in the image.

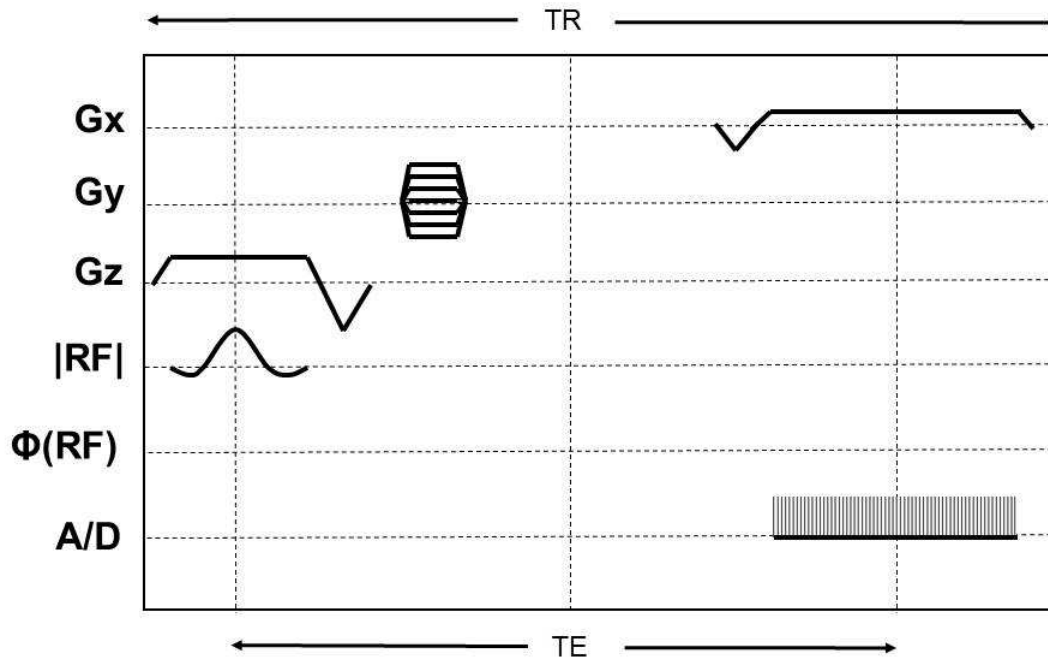


Fig. 12 Timing diagram of the traditional GRE pulse sequence. The GRE sequence has a non-steady-state magnetization and only a 90-degree excitation.

The GRE sequence is generated by using a pair of bipolar gradient pulses which has a non-steady-state magnetization consists of an excitation and readout as usual, as seen as Fig.12. There is no refocusing 180° pulse and the data are sampled during a gradient echo, which is achieved by dephasing the spins with a negatively pulsed gradient before they are rephased by an opposite gradient with opposite polarity to generate the echo. The flip angle of the excitation is typically between 0° and 90° , which also be slowly increased during data acquisition. With a small flip angle there is a reduction in the value of transverse magnetization that will affect subsequent RF pulses. However, at the end of sequence is a spoiler-gradient basically a gradient that tried to completely dephase the transverse magnetization across voxel. GRE techniques are very common. It is useful to compare their contrast characteristics to the other sequences here. GRE sequences have a lower SAR, are more sensitive to field inhomogeneity and have a reduced crosstalk. Gradient Recalled Acquisition in Steady State (GRASS) sequence is one of GRE

sequences with low flip angles and without the spoiler pulse. As a result, any transverse magnetization still present at the time of the next RF pulse is incorporated into the steady state. GRASS uses a RF pulse that alternates in sign. Because there is still some remaining transverse magnetization at the time of the RF pulse, a RF pulse of a degree flips the spins less than a degree from the longitudinal axis. Spoiled Gradient Recalled (SPGR) sequence is similar to the spoiled GRASS sequence. The spoiled gradient recalled (SPGR) acquisition in steady state uses semi-random changes in the phase of the radio frequency (RF) pulses to produce a spatially independent phase shift.

The proposed Hybrid encoding pulse sequence is simulated using the Bloch equations. The RF pulses are from the circulant matrix C , as seen as Eq. (20), which has some complex numbers with uniform constant magnitudes and random initial phases which is uniformly distributed on $[0, 2\pi]$. The RF pulses are actually the Fourier transformation of every column of the circulant matrix C . Each random RF pulse generates a random excitation at every TR along the Y direction. A gradient G_y is turned on along Y direction, simultaneously with the RF pulse. Others are as same as SE or GRE pulse sequences. As seen as the Fig. 13, the dephasing gradient after the G_y gradient can affect the phase of the k -space raw data. Actually it will change the position of the field-of-view (FOV) in the image domain. Without the dephasing gradient seen Fig.13 (a, c) and with the dephasing gradient seen Fig.13 (b, d), the image can also be well decoded or reconstructed. The Bloch equation simulation shows that the distribution of the k -space raw dataset will variant because of the amplitude of the dephasing gradient.

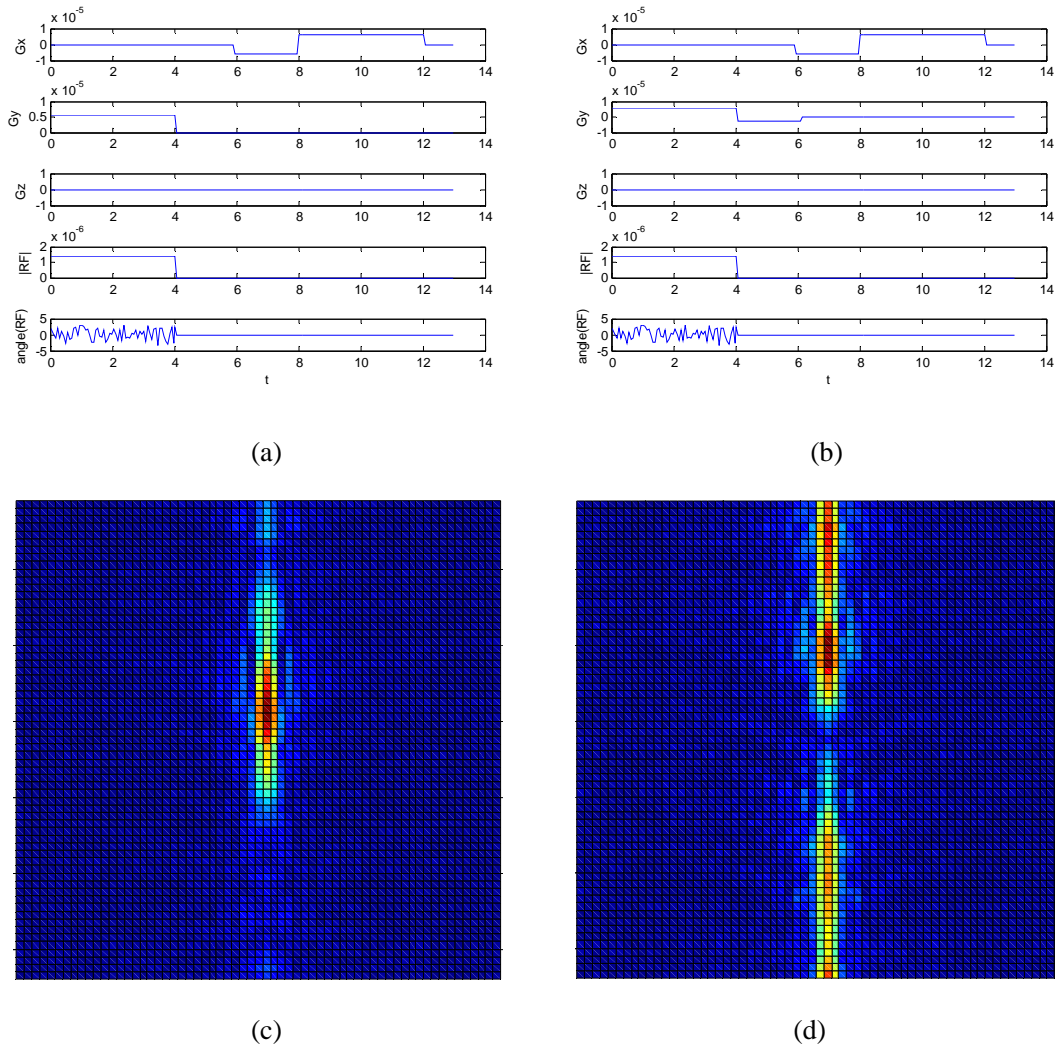


Fig. 13 Timing diagrams without dephasing gradient (a) and with dephasing gradient (b) and k -space raw data without dephasing gradient (c) and with dephasing gradient (d) of the proposed Hybrid encoding pulse sequence

3.2.5. Pulse Sequence Implementation

The proposed 3D Hybrid encoding methods have been implemented on the 1.5 and 3.0 Tesla GE SIGNA MR Systems at GE Healthcare, Waukesha, WI. The system hardware consists from two parts: the host and target. The target usually is the SIGNA MR system, and the host usually is the workstation system. The host running on Linux OS is used to set scan prescription, image

displaying and post-processing. The target is used to generate waveform excitation, data acquisition, filtering and reconstruction. The components of the target can directly control the elements in the magnet room. Sometimes they referred to as Transceiver Processing and Storage (TPS), Acquisition Processing System (APS), Application Gateway Processor (AGP), Digital Receiver Filter (DRF), Interface & Remote Function (IRF), Scan Control Processor (SCP), Array Processor (AP) and Sequence Related Functions/Trigger & Rotational Functions (SRF/TRF), as seen as Fig. 14. In general, the MR excitation unit consists of the x, y, and z MR gradient magnet coils, as well as RF transmitter and receiver coils. The TPS unit controls pulses to all MR gradient magnet coils, as well as RF coils, and receives (acquires and stores) MR data according to the pulse sequence software. The Host computer serves as the user interface (as seen as Fig. 15), image database, and communication gateway for the system console. A computer is connected to the SIGNA computer system via a switched Ethernet network using the TCP/IP protocol, which downloads the k -space raw data, and reconstruct images on the MATLAB platform. The 3D Hybrid encoding pulse sequence types was developed based on gradient-recalled echo pulse sequences, as seen as Fig. 16. The amplitude of the RF pulse is constant, and the phase of RF pulse and the amplitude of the X, Y and Z gradients obey the rulers and calculations described on the Chapter 3.2.3. According to the pulse sequences as seen as Fig. 16, the actual pulse sequences can add some additional components to become the proposed pulse sequences based on 3D GRASS or 3D SPGR pulse sequences. Actually the proposed Hybrid encoding pulse sequence based on 3D GRASS pulse sequence has not spoiler pulse, but the proposed Hybrid encoding pulse sequence based on 3D SPGR pulse sequence has spoiler pulse. The actual experimental results shows that the proposed Hybrid encoding pulse sequences based on 3D SPGR has less aliasing artifacts and larger amplitudes of the RF pulses than the proposed Hybrid encoding pulse sequences based on 3D GRASS pulse sequence.

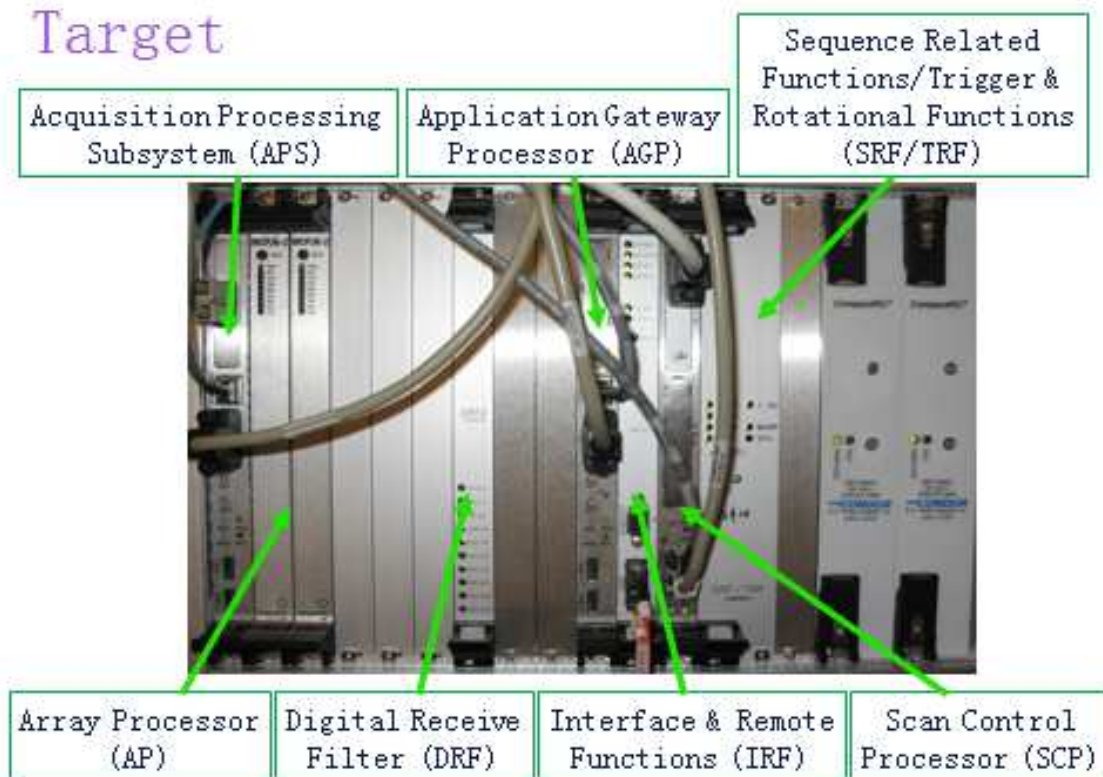


Fig. 14 Basic components of the target in GE SIGNA MR Systems. They are Transceiver Processing and Storage (TPS), Acquisition Processing System (APS), Application Gateway Processor (AGP), Digital Receiver Filter (DRF), Interface & Remote Function (IRF), Scan Control Processor (SCP), Array Processor (AP) and Sequence Related Functions/Trigger & Rotational Functions (SRF/TRF).

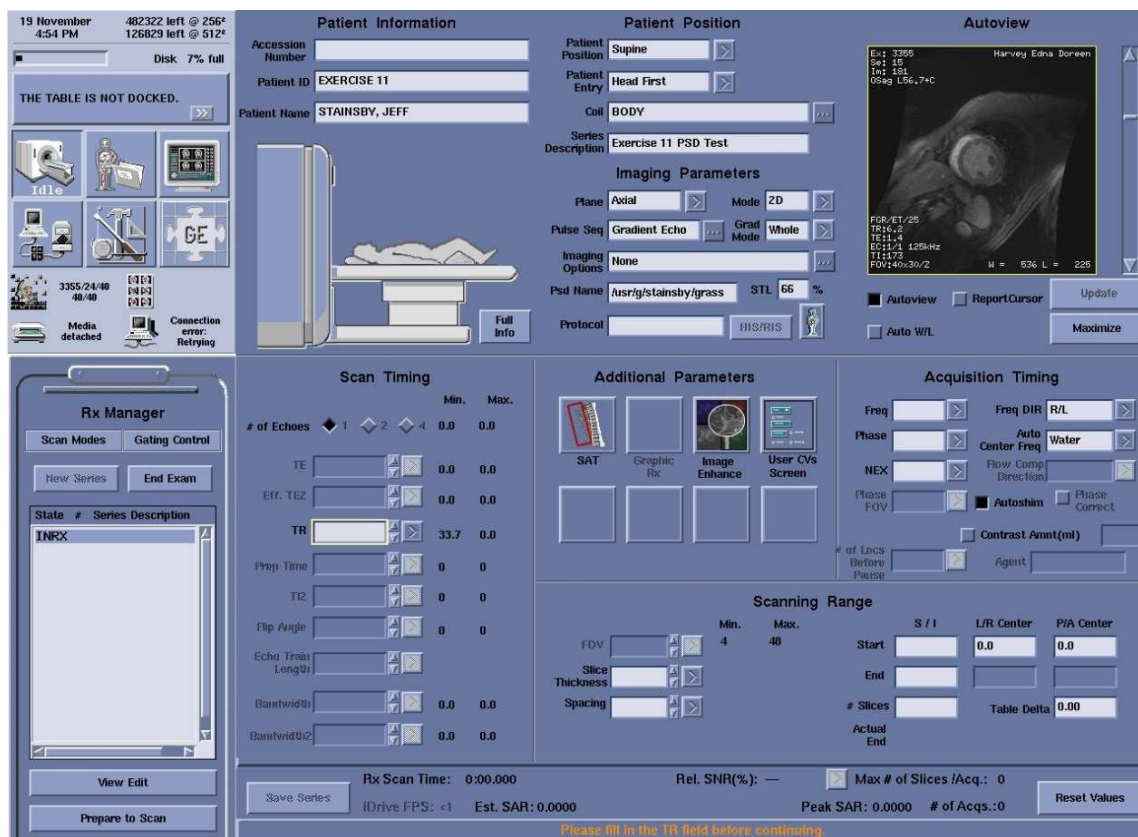


Fig. 15 Human interface of the host computer. The pulse sequences are controlled by the parameters on the human interface on the host computer, such as TE, TR, FOV, BW, thickness, flip angle, spacing, etc.

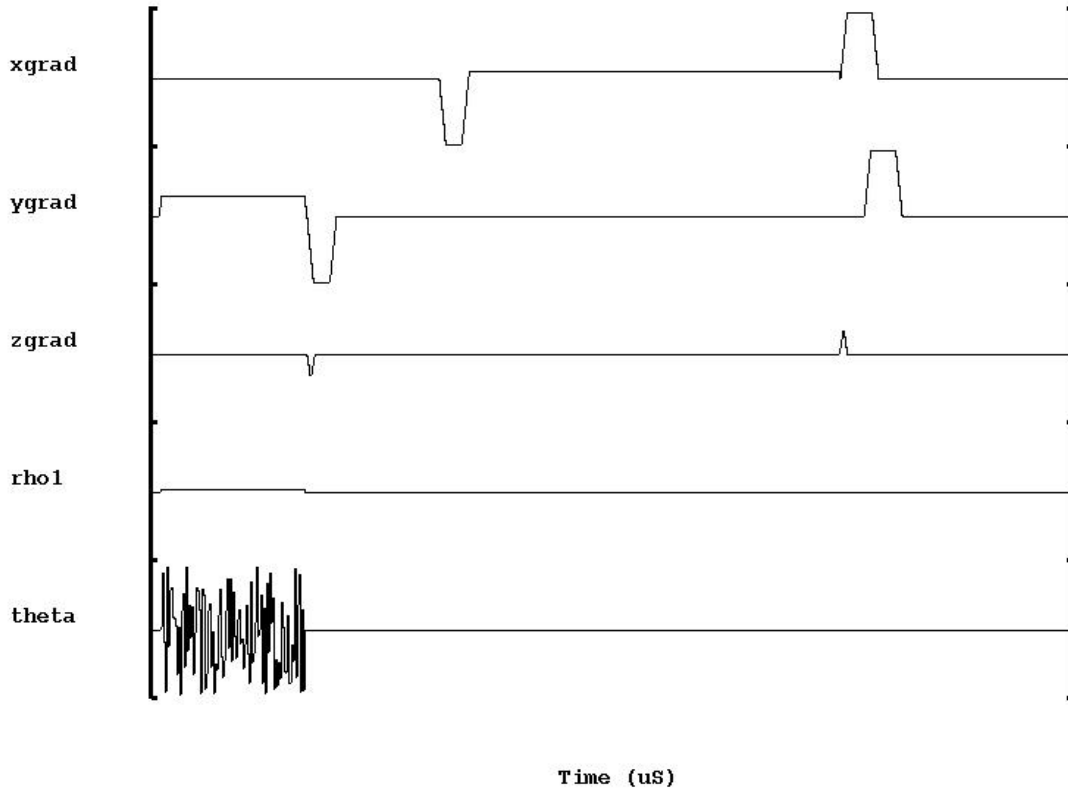


Fig. 16 Actual timing digram of the proposed 3D Hybrid encoding pulse sequence. It has circulant random encoding along Y axis, slice encoding along Z axis, and frequency encoding along X axis.

3.3 Pseudo 2D Random Sampling in CS MRI

We design a practical random sampling pattern for conventional Cartesian MRI that performs similarly to the 2D random sampling pattern on SparseMRI [19]. The 2D random sampling uses a 2D variable-density sampling pattern with denser sampling near the center of the k -space. The probability function for sampling at a location \vec{r} in k -space is [19]:

$$p(\vec{r}) = \begin{cases} 1 & r \leq R_d \\ \frac{1}{(1-r)^p} & r > R_d \end{cases} \quad (30)$$

where $r = \|\vec{r}\|_2$, $\vec{r} = [r_x \ r_y]^T$, and R_d is a real number and $0 < R_d < 1$. Since the 2D random sampling cannot be physically implemented in conventional MRI scanners, 1D random sampling is adopted instead. The 1D random sampling uses a 1D variable-density sampling scheme with denser sampling near the center of the k -space. The corresponding probability function is:

$$p(\vec{r}) = \begin{cases} 1 & r \leq R_d \\ \frac{1}{(1-r_x)^p} & r > R_d \end{cases} \quad (31)$$

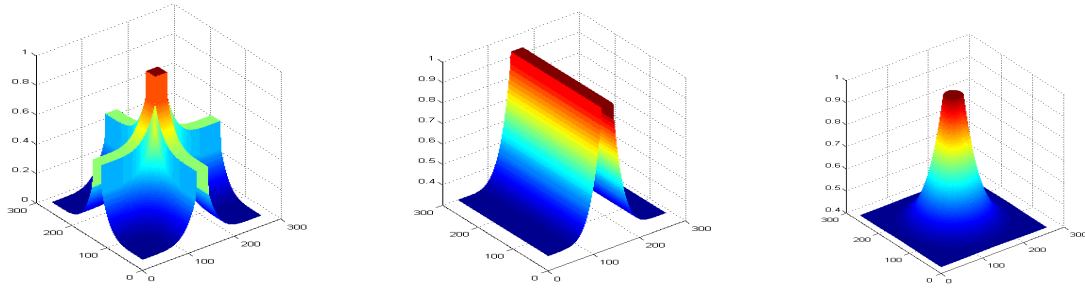
where the parameters are defined as same as Eq. (30).

Our proposed sampling scheme adopts a distribution function different from either 2D or 1D random sampling. It uses two 1D variable-density sampling that are orthogonal to each other in Cartesian k -space, also with denser sampling near the center of the k -space. The corresponding probability function is:

$$p(\vec{r}) = \begin{cases} 1 & r \leq R_d \\ \frac{a}{(1-r_x)^p} + \frac{1-a}{(1-r_y)^p} & r > R_d \end{cases} \quad (32)$$

where the parameters are defined as same as Eq. (30). a is a constant that depend on the number of sampling lines along k_x direction of k -space.

Fig. 17 compares the probability functions of the three random sampling patterns. It is obvious that the proposed pseudo 2D random sampling is closer to the 2D random sampling than the 1D random sampling is. As a result, the proposed pseudo 2D random sampling should outperform the 1D random sampling in CS reconstruction.



(a) pseudo 2D random sampling

(b) 1D Random Sampling

(c) 2D Random Sampling

Fig. 17 Probability function (top row) and the corresponding sampling pattern (bottom row) of the three random sampling patterns.

In conventional Cartesian MRI, the phase encoding gradient and frequency encoding gradient are applied on orthogonal directions in k -space [69]. The amplitude of the phase encoding gradient is changed at each excitation to sample a different line in k -space. The 1D random sampling can be easily implemented by changing the amplitudes of the phase encoding randomly. However, it is extremely difficult (if not impossible) to implement 2D random sampling which requires simultaneous change of the phase encoding and frequency encoding gradients randomly. In current commercial MR systems, gradients of pulse sequences are limited by maximum amplitude and maximum slew-rate. In addition, high gradient amplitudes and rapid switching can produce peripheral nerve stimulation.

The proposed pseudo 2D random sampling scheme can be implemented on a conventional MRI scanner as easily as the 1D scheme. To realize the proposed sampling scheme, both the amplitude and the direction of the phase encoding gradient have to be changed. For example, if the total N lines are to be acquired, the first N_1 lines are acquired with phase encoding along k_x

direction and frequency encoding along k_y direction, and the rest $(N-N_I)$ lines with phase encoding along k_y direction and frequency encoding along k_x direction. In either case, these data are randomly undersampled only along the phase encoding direction, while keeping the frequency encoding direction to be fully sampled. The value of N depends on the undersampling factor to achieve, and the value of N_I is equal to $a \cdot N$, where a is the constant in Eq. (32).

Fig. 18 shows the timing diagram of the pulse sequences for the proposed pseudo 2D random sampling. The gradients shown in solid red represent the 1D random sampling sequence with phase encoding along y and frequency encoding along k_x direction. In the proposed pseudo 2D random sampling, we alternate between the gradients in solid red and those in dashed green. It corresponds to alternatively switching phase and frequency encoding directions.

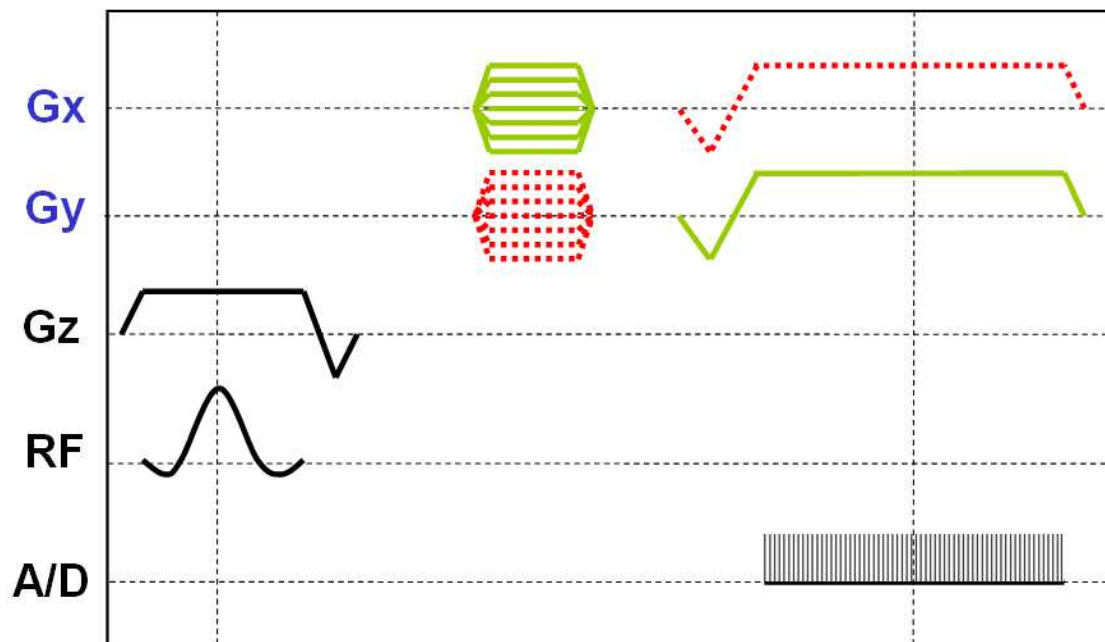


Fig. 18 Timing diagram of the pulse sequences for the pseudo 2D random sampling scheme. Dynamically swap red and green directions to alternatively change phase encoding and frequency encoding directions on real physics k -space.

As seen in Fig. 17 (a), at certain locations of the k -space, the data are acquired twice – one from the horizontal lines and the other from the vertical lines. The two values are averaged to represent the value of the data at this point at the ideal situation. There are a total of $N_l \times (N - N_l)$ such points. Although there is redundancy in such data acquisition, the averaging can improve the signal to noise ratio of the acquired data and thus the reconstructed image. With the data acquired using the proposed sampling scheme, the image is reconstructed by the following nonlinear convex program [19, 70-71],

$$\arg \min_{\mathbf{f}} \{ \|\Psi \mathbf{f}\|_1 + \alpha \cdot TV(\mathbf{f}) \} \quad s.t. \quad \|\mathbf{F}_u \mathbf{f} - \mathbf{b}\|_2 < \varepsilon \quad (33)$$

where \mathbf{f} is the sparse image to be reconstructed and is presented as a vector; Ψ denotes the linear operator that transforms the image from a pixel representation into a sparse representation, such as wavelet transform; \mathbf{b} is the acquired k -space data; \mathbf{F}_u is Fourier Transform associated with the proposed under-sampling pattern; $TV(\cdot)$ is total-variation function; ε controls the fidelity of reconstruction to the measured data. Here, the threshold parameter ε is usually set below the expected noise level.

4. Simulations and Experiments

4.1 Cross-GRAPPA

The proposed Cross-GRAPPA was evaluated using simulation, phantom experiment, and two *in vivo* experiments. All reconstruction schemes were implemented in MATLAB (MathWorks, Natick, MA) on an HP XW8400 workstation with 2.33GHz CPU and 2GB RAM. The SoS reconstruction from the fully sampled data was used as the reference image for comparisons. The proposed Cross-GRAPPA method was compared with the conventional GRAPPA. The

reconstructed images with different ORFs and number of ACS lines were shown for visual comparison of noise and artifacts. The coefficient of 4 blocks and 5 columns was employed for all reconstructions. On the following results, “Cross” means the proposed Cross-GRAPPA.

The objective of the simulation is to demonstrate the performance of the proposed method under the ideal condition when the ACS and undersampled data are exactly consistent. A set of fully acquired *in vivo* data was used to simulate the acquisition pattern of the proposed Cross-GRAPPA method by manually omitting the “missing data”. The data set was obtained from a 3T commercial MR scanner (GE Healthcare, Waukesha, WI) with an 8-channel head coil (Invivo, Gainesville, FL) using a 2D spin echo (SE) sequence (TE/TR = 11/700ms, matrix size = 256×256 , FOV = 220mm^2). Informed consent was obtained from the volunteer in accordance with the institutional review board policy. Both GRAPPA and Cross-GRAPPA were performed at ORFs of 2, 3 and 4 with 8, 12 and 16 ACS lines respectively. In addition, we also distribute a fixed number of ACS lines to both parallel and orthogonal directions with different ratios. An ORF of 4 and total of 16 ACS lines were used. It is expected to find an optimal ratio for such a combination.

A phantom experiment was carried out to demonstrate the performance of the proposed method in absence of the chemical shift effects of *in vivo* study. A uniform water phantom was scanned using a gradient echo (GRE) sequence (TE/TR = 10/100 ms, 31.25 kHz bandwidth, matrix size = 256×256 , FOV = 250mm^2) on a 3T commercial scanner (GE Healthcare, Waukesha, WI) with an 8-channel head coil (Invivo, Gainesville, FL). Two sets of fully sampled data were acquired separately with two orthogonal readout directions. One dataset was manually reduced to generate the undersampled acquisition and the other was reduced to obtain the cross-sampled ACS data for Cross-GRAPPA. The first dataset was used for conventional GRAPPA. Results for both conventional GRAPPA and Cross-GRAPPA were compared with different number of ACS lines at an ORF of 4. The comparison is to find the least number of ACS lines required for each method to suppress aliasing artifacts.

Two *in vivo* experiments were performed on a 3T commercial MR scanner (GE Healthcare, Waukesha, WI) with an 8-channel head coil (Invivo, Gainesville, FL) to validate the proposed method in presence of all practical conditions. Brain was chosen to be the anatomical region of interest in this study due to minimal chemical-shift effects. All data were acquired in accordance with the institutional review board policy. Similar to the phantom experiments, each *in vivo* experiment acquired two sets of fully sampled data with orthogonal readout directions. The first experiment uses a spin-echo sequence with parameters $TE/TR = 10/550$ ms, 31.25 kHz bandwidth, matrix size = 256×256 , FOV = 220 mm^2 , and the other one uses a spin-echo sequence with $TE/TR = 14/500$ ms, 62.5 kHz bandwidth, matrix size = 256×256 , FOV = 240 mm^2 . Conventional GRAPPA and Cross-GRAPPA were both performed at the ORFs of 2, 3 and 4 with 8, 8, 10 ACS lines, respectively. We also compare conventional GRAPPA and Cross-GRAPPA with an increasing number of ACS lines at an ORF of 4 to find the least number required for artifacts-free reconstruction.

4.1.1 Simulation

The reconstruction results of GRAPPA and Cross-GRAPPA are shown in Fig. 19. Cross-GRAPPA performs similar to GRAPPA at a low ORF of 2, but significantly reduces the aliasing artifacts in GRAPPA with only very few ACS lines at higher ORFs. This is because at low ORFs, the coefficients can be calibrated accurately with a small amount of ACS data along the direction that is undersampled. The increase of ACS data along the undersampled direction by Cross-GRAPPA does not reduce the aliasing artifacts. At high ORFs, calibration of the coefficients demands more ACS data along the undersampled direction than those along the fully sampled direction, and thus the benefit of Cross-GRAPPA becomes more evident. On the other hand, it is also seen that the reduced aliasing artifacts in Cross-GRAPPA is at the cost of slightly reduced SNR. Data co-registration is not necessary here for simulation because both the ACS and

undersampled data are obtained from an acquisition with the same readout directions. In summary, the simulations show when the data are perfectly consistent, Cross-GRAPPA requires fewer ACS lines than GRAPPA to suppress the aliasing artifacts.

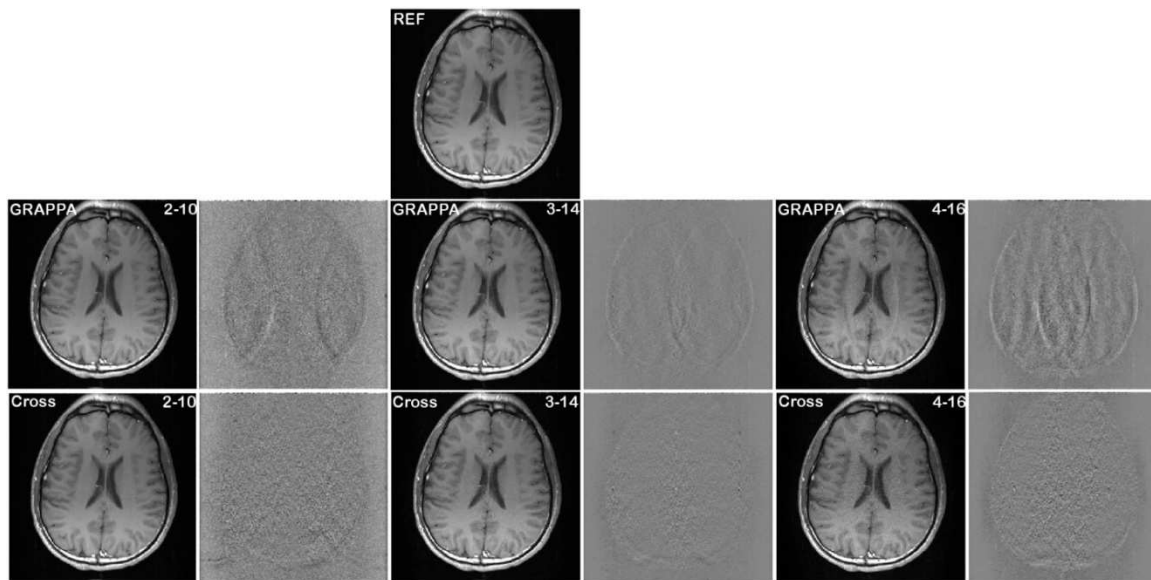


Fig. 19 GRAPPA and Cross-GRAPPA reconstructions from 8-channel human brain data and their corresponding difference images with the reference. The ORFs of 2 with 10 ACS lines, 3 with 12 ACS lines, and 4 with 16 ACS lines (shown on the top-right corner) were used.

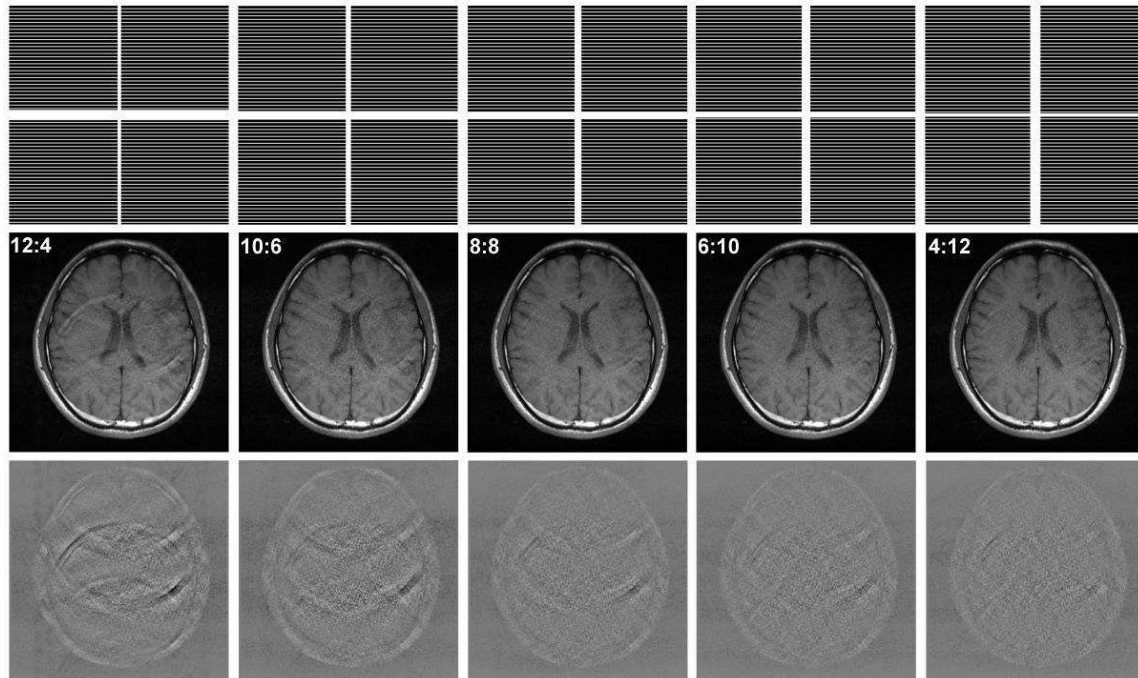


Fig. 20 Sampling patterns (top row), reconstructions (middle row) and their corresponding difference images (bottom row) with the reference when different combinations of parallel- and cross- sampled ACS lines. The ORF is 4 and total number of ACS lines is 16. The distributions among the parallel- and cross-sampled directions are 12:4, 10:6, 8:8, 6:10, and 4:12 from left to right.

The sampling patterns for a mix of both parallel- and cross-sampled ACS lines are shown in Fig. 20 top row. They can be viewed as intermediate transitions from conventional GRAPPA (all parallel ACS) to Cross-GRAPPA (all cross ACS) with conventional GRAPPA and Cross-GRAPPA being two extreme cases. Fig. 20 shows the results when both parallel- and cross-sampled ACS lines were combined for reconstruction. Different distributions between the two directions were used. The results demonstrate that the more cross-sampled ACS lines, the fewer the aliasing artifacts. It suggests that it is desirable to acquire all ACS lines in orthogonal when only few ACS lines are acquired.

4.1.2 Phantom Experiment

Fig. 21 shows the phantom reconstruction results comparing conventional GRAPPA and Cross-GRAPPA. For Cross-GRAPPA, the parameters δ_x , δ_y , α , and β for data co-registration were initialized to be -1.0, -1.0, 1.0, and 1.0, respectively. After data co-registration, the parameters δ_x , δ_y , α , and β were optimized to be -0.4653, -0.4425, 0.9987, and -0.0398, respectively. Although the optimization process generated parameters that are slightly different for different ORFs and ACS lines, the same set of values were used without degrading the image quality. It is seen that Cross-GRAPPA performs similarly to conventional GRAPPA when ORF is 2. As the ORF increases, conventional GRAPPA requires a much larger amount of ACS data along the undersampled direction. When the number of ACS lines is not sufficient, conventional GRAPPA reconstructions present aliasing artifacts. Cross-GRAPPA can significantly reduce these aliasing artifacts by maximizing the amount of ACS data along the undersampled direction without prolonging the ACS acquisition time. The consistent results with simulation suggest that the co-registration method can effectively align the data with orthogonal readouts for the phantom study.

In Fig. 22, we increase the number of ACS lines from 14 to 20, 24 and 26 for both conventional GRAPPA and Cross-GRAPPA with an ORF of 4. The reconstruction results show that conventional GRAPPA reconstruction improves with the number of ACS lines due to the increased calibration data along the undersampled direction. In contrast, Cross-GRAPPA remains almost the same. This is because more ACS lines in Cross-GRAPPA increases the amount of ACS data only along the fully sampled direction in reconstruction and is not contributing to artifacts reduction after saturation. Conventional GRAPPA needs at least 26 ACS lines to achieve a quality similar to that achieved by Cross-GRAPPA with as few as 14 ACS lines.

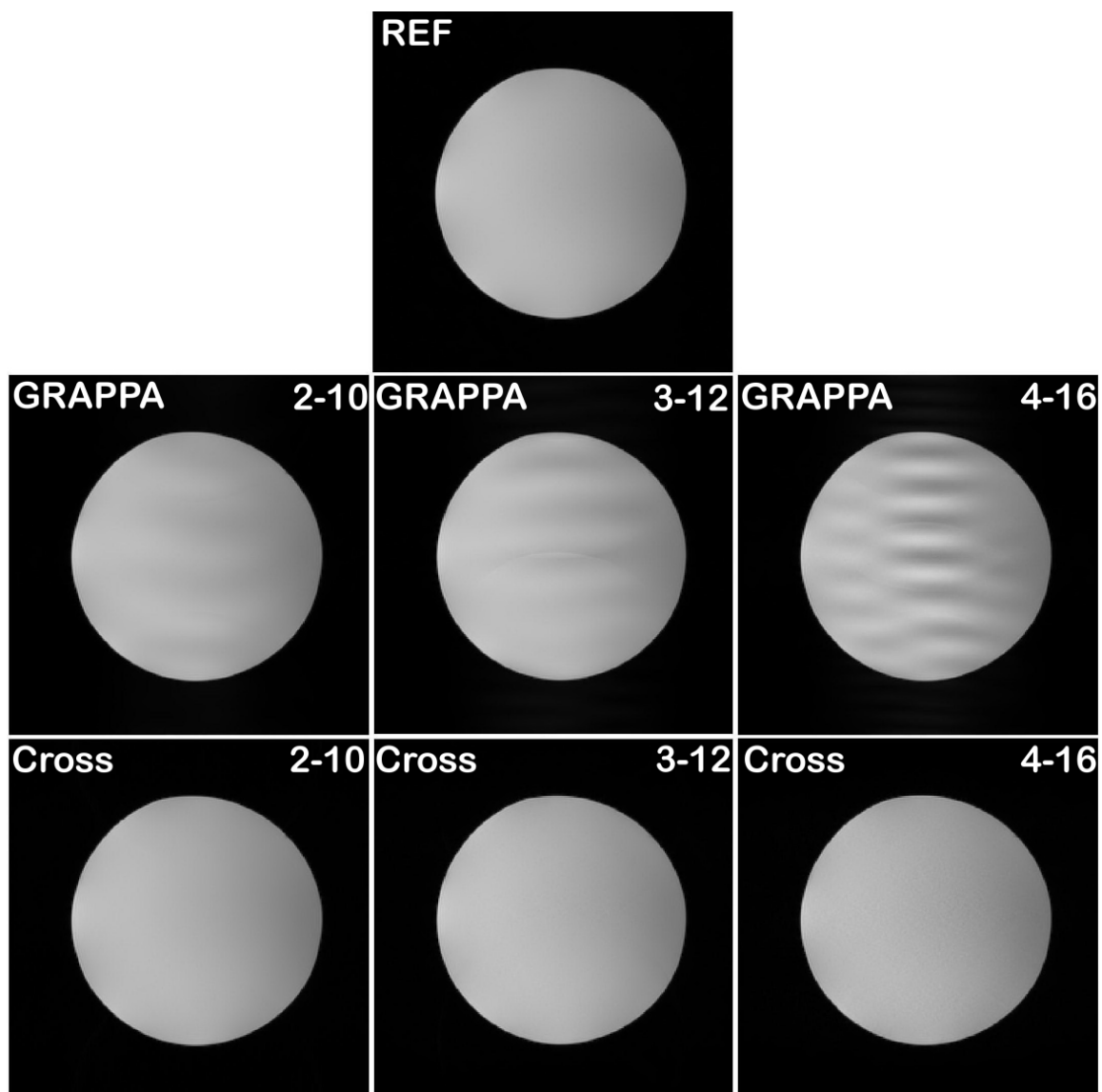


Fig. 21 GRAPPA and Cross-GRAPPA reconstructions from an 8-channel phantom experiment.

The top-right corner of each image shows the ORF-ACS combinations of 2-10, 3-12 and 4-16.

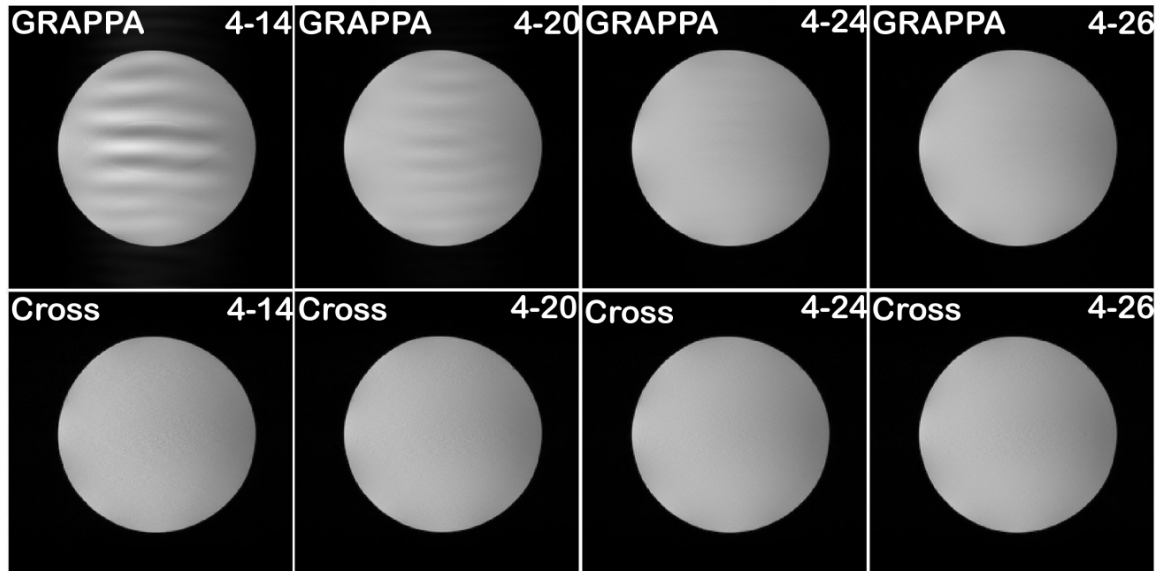


Fig. 22 Phantom results of GRAPPA (top) and Cross-GRAPPA (bottom) with an ORF of 4 and ACS lines of 14, 20, 24 and 26 from left to right. The results show that GRAPPA reconstruction improves with the number of ACS lines, while Cross-GRAPPA remains almost the same. GRAPPA needs at least 26 ACS lines to achieve a quality similar to that achieved by Cross-GRAPPA with as few as 14 ACS lines.

4.1.3 In Vivo Experiments

Fig. 23 shows conventional GRAPPA and Cross-GRAPPA reconstructions for the first experiment. For the proposed Cross-GRAPPA, the initial parameters δ_x , δ_y , α , and β for data co-registration were -1.0, -1.0, 1.0, and 1.0, respectively. After data co-registration, the optimized parameters δ_x , δ_y , α , and β were calculated to be -0.2792, -0.3155, 1.0909, and 0.3987, respectively. Consistent with the simulation and phantom studies, conventional GRAPPA and Cross-GRAPPA performs similarly well at an ORF of 2. At ORFs of 3 and 4, both present a higher level of noise, but Cross-GRAPPA suppresses much more aliasing artifacts than conventional GRAPPA with the same number of ACS lines.

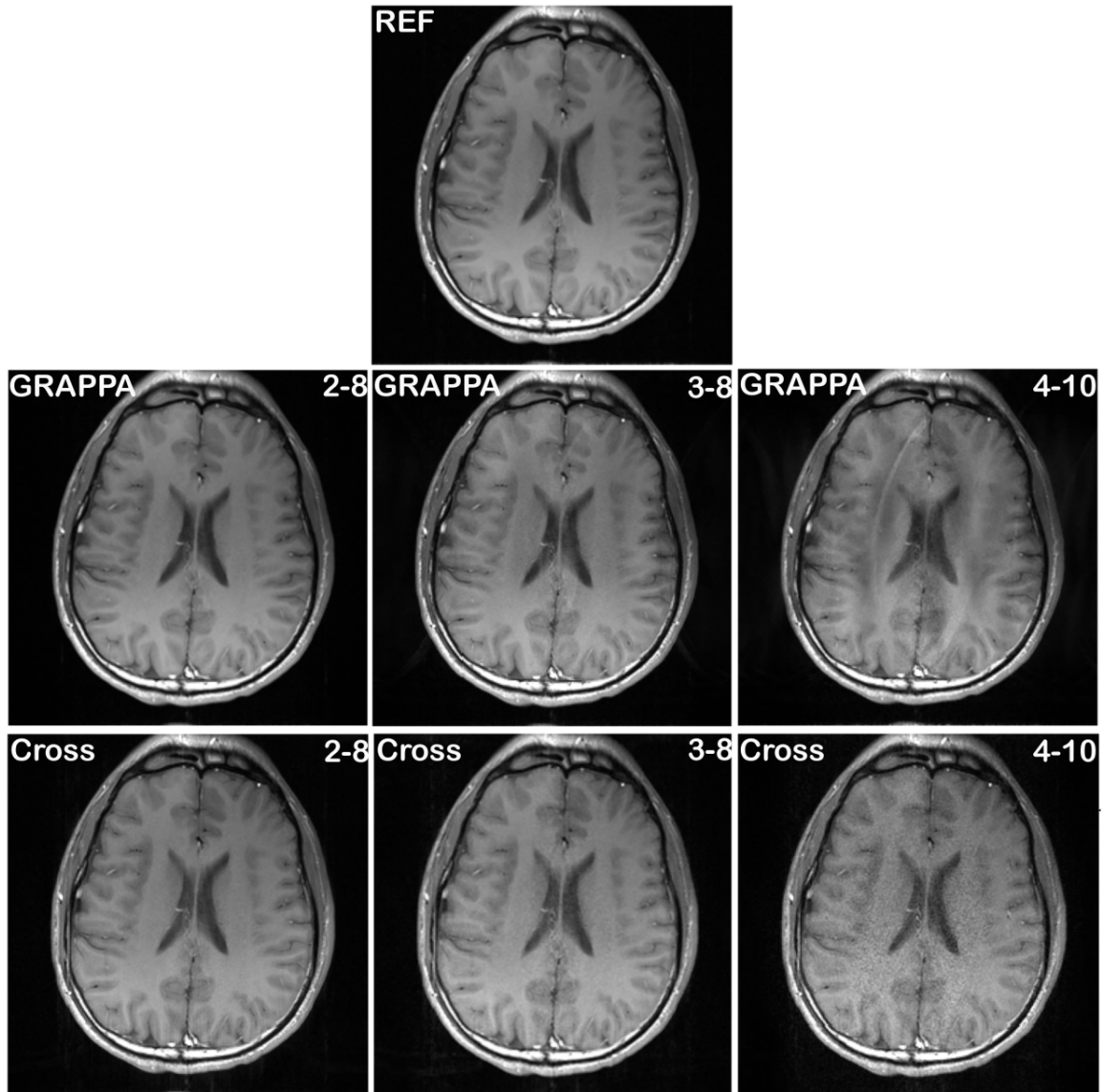


Fig. 23 GRAPPA and Cross-GRAPPA reconstructions of the first set of 8-channel *in vivo* data.

The top-right corner of each image shows the ORF-ACS combinations of 2-8, 3-8 and 4-10.

Fig. 24 compares conventional GRAPPA and Cross-GRAPPA with increasing numbers of ACS lines at an ORF of 4. The results show that GRAPPA reconstruction improves with the number of ACS lines, while Cross-GRAPPA barely changes. Even with 32 ACS lines, visible residual aliasing artifacts still present in conventional GRAPPA, while the artifacts are well suppressed in Cross-GRAPPA with only 10 ACS lines.

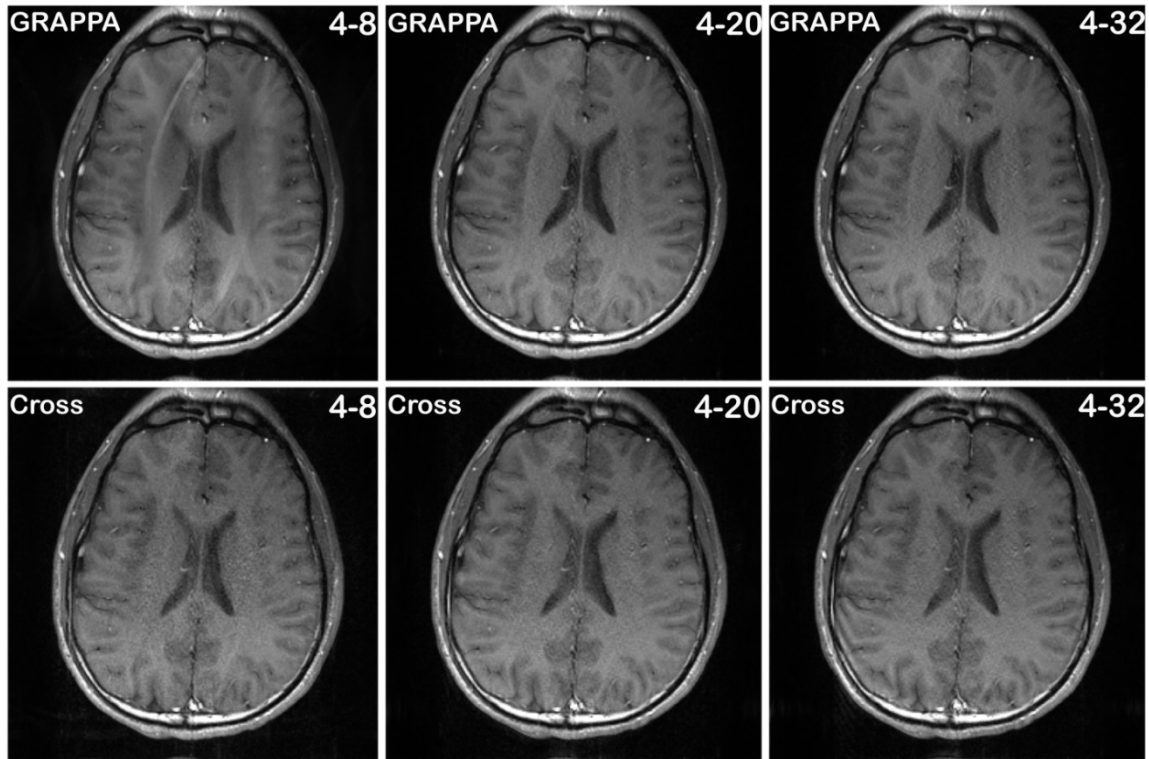


Fig. 24 GRAPPA and Cross-GRAPPA reconstructions of the first set of 8-channel brain data. The top-right corner of each image shows the ORF-ACS combinations of 4-8, 4-20 and 4-32.

Fig. 24 shows conventional GRAPPA and Cross-GRAPPA reconstructions for two slices of the other *in vivo* experiments. The co-registration parameters δ_x , δ_y , α , and β were calculated to be -0.4569, -0.5650, 1.0219, and 0.7661, respectively for the first slice (top row) and -0.7034, -0.5185, 0.9118, and 0.8956, respectively for the second one (bottom row). The reconstruction results of both slices demonstrate that Cross-GRAPPA suppresses more aliasing artifacts but presents more noise than conventional GRAPPA at the same ORF-ACS combination.

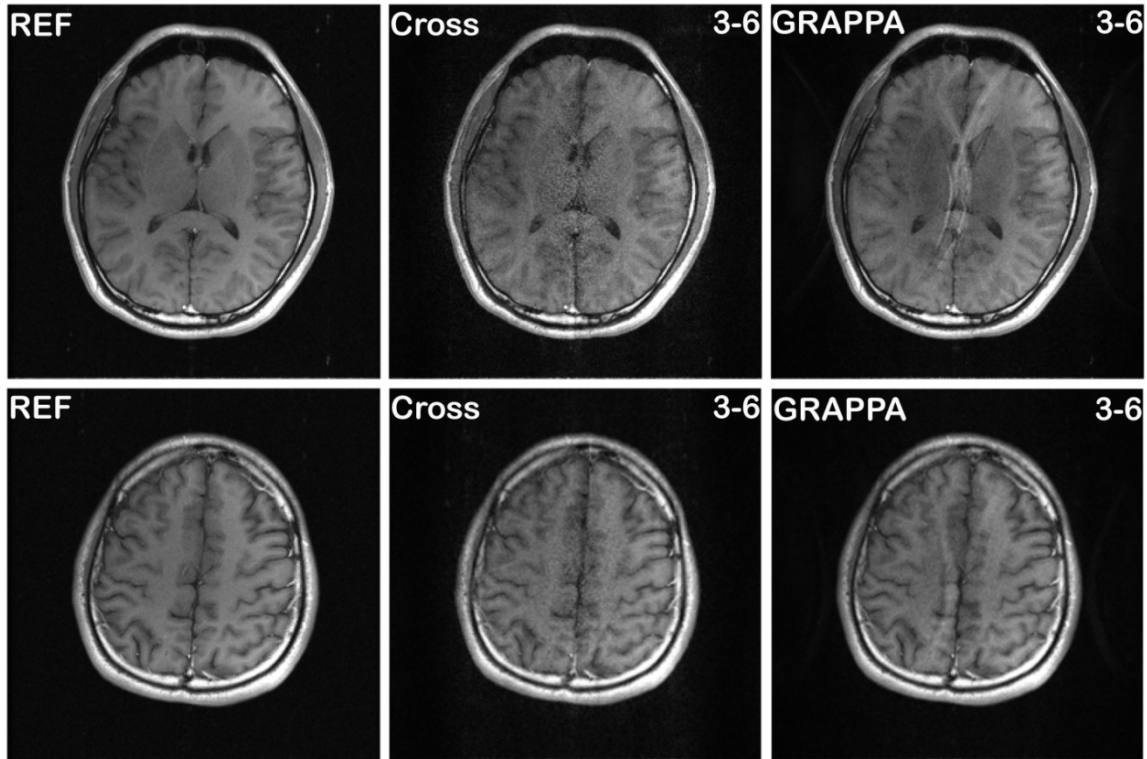


Fig. 24 GRAPPA and Cross-GRAPPA reconstructions of two slices for the second *in vivo* experiment at an ORF of 3 and ACS lines of 6. The results consistently show that Cross-GRAPPA can suppress more aliasing artifacts than GRAPPA but at the cost of degraded SNR when few ACS lines are acquired.

4.1.4 Noise Issue

The noise behavior of conventional GRAPPA reconstruction has been well investigated in Refs. [72-73]. Cross-GRAPPA has similar behavior such as spatially-varying noise but usually presents a higher level of noise. It is conjectured that this reduced SNR is due to the tradeoff between SNR and reduced aliasing artifacts in reconstruction, similar to the observation in SENSE regularization [74]. This conjecture is also based on the observation in the top row of Fig. 3 where conventional GRAPPA reconstruction with more (e.g., 30) ACS lines is noisier but has fewer artifacts than that with fewer (e.g., 10) lines. Mis-registration of the data with orthogonal

readouts does not seem to be the cause of increased noise because the reduced SNR of Cross-GRAPPA is also evident in simulation results in the bottom row of Fig. 20 where no mis-registration is present.

The higher level of noise in Cross-GRAPPA can be suppressed using methods like regularization [32], iterative optimization [37], or nonlinear GRAPPA [41]. As said before, nonlinear GRAPPA replaces the conventional linear fitting procedure with a nonlinear model to suppress noise in the final image [75]. The nonlinear fitting procedure can be directly used in Cross-GRAPPA reconstruction and the reconstruction results of the first set of *in vivo* data at the ORF of 4 is shown in Fig. 25. The optimized co-registration parameters δ_x , δ_y , α , and β were calculated to be -0.2793, -0.3148, 1.0914, and 0.3984. It is seen the nonlinear approach improves the SNR of Cross-GRAPPA. The improvement suggests that noise reduction methods can be easily integrated into the proposed cross-sampling framework to achieve even higher acceleration.

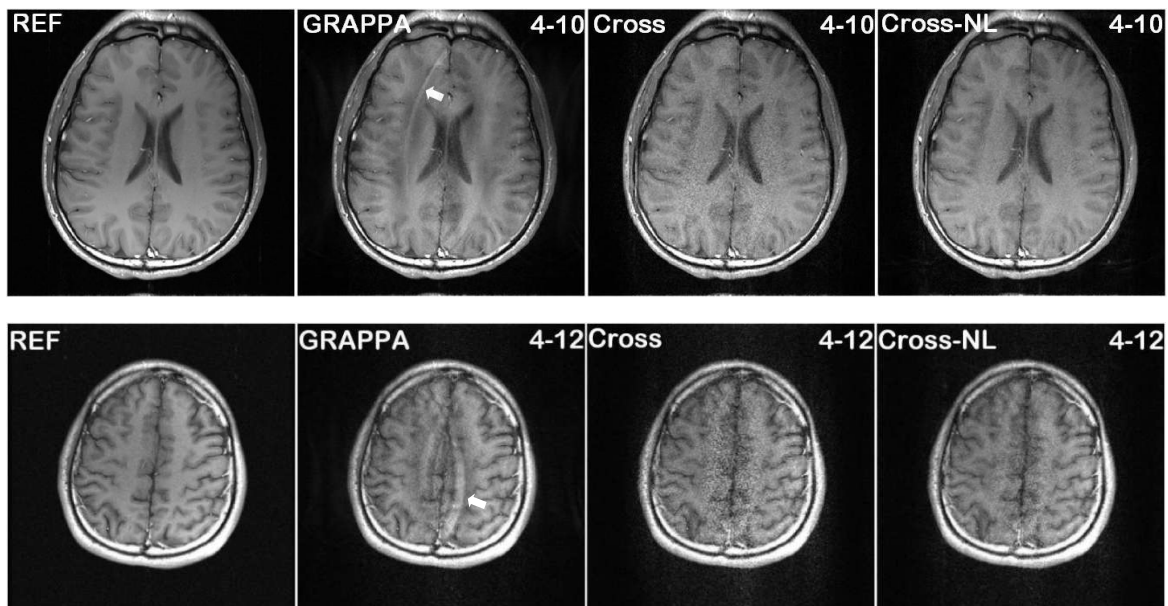
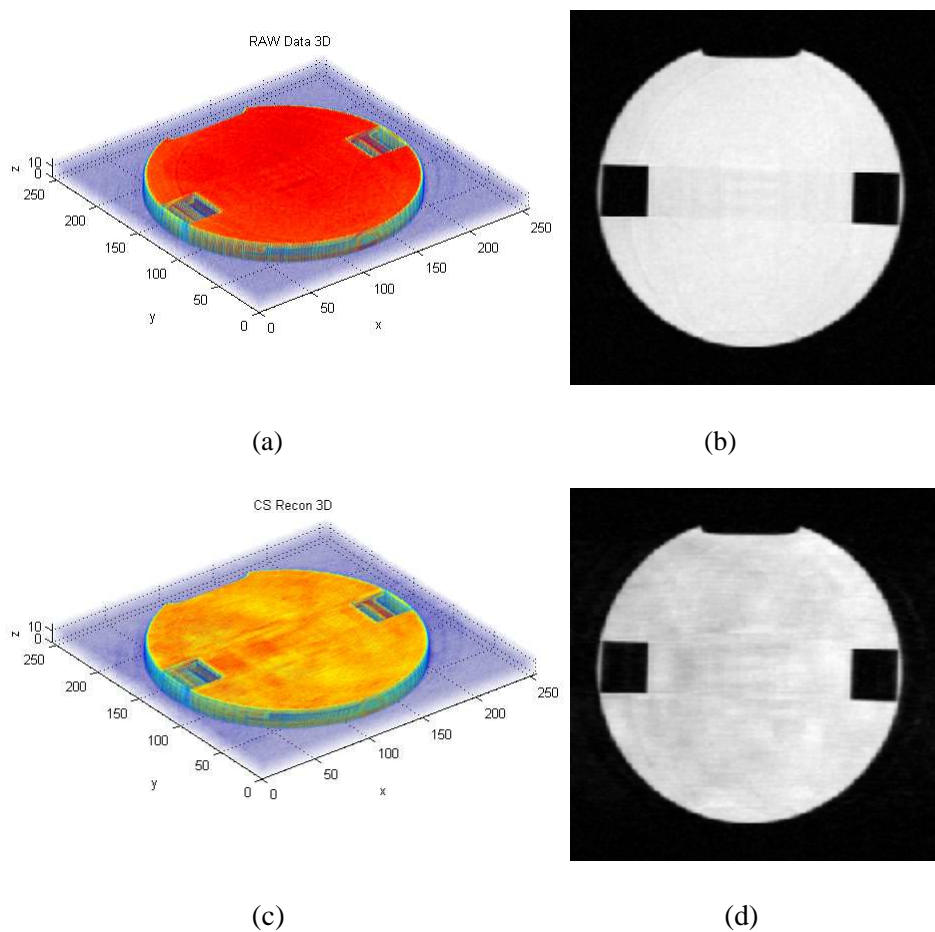


Fig. 25 MR image reconstruction comparisons of GRAPPA, Cross-GRAPPA (Cross) and Cross-GRAPPA with nonlinear GRAPPA (Cross-NL). The reconstructions use ORF-ACS combinations of 4-10 and 4-12.

4.2 Hybrid-Encoded MRI

4.2.1 Simulations of GE QA Phantom

We conducted the simulations of GE QA phantom to demonstrate the different performance of the proposed 3D Hybrid encoding and the conventional 3D Fourier encoding. The dataset of GE QA phantom was scanned by the 3.0T MRI scanners (GE Healthcare, Waukesha, WI) with 3D GRE pulse sequence. One-channel body coil was applied to acquire the k -space raw dataset. The reduction factors are both 2.0 for 3D Fourier encoding and 3D Hybrid encoding. As seen as the Fig. 26, the results demonstrate the CS recon of the proposed 3D Hybrid encoding is closer to the reference images than the CS recon of the conventional 3D Fourier encoding.



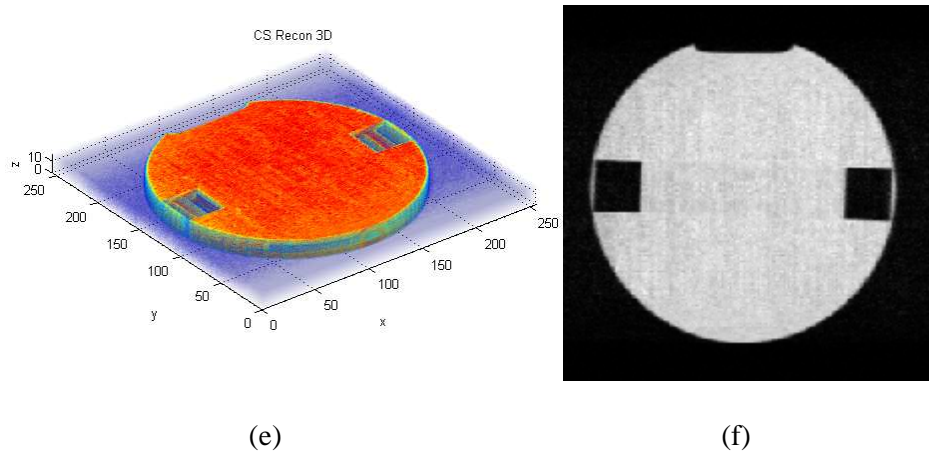


Fig. 26 3D MR images and one slice of images of the reference (a, b), the CS recon of Fourier encoding(c, d), and the CS recon of Hybrid encoding (e, f)

4.2.2 Simulations of Human Brain and Knee

We conducted the simulations of human brain and knee to demonstrate the different methods in the context of CS framework. For Fourier encoding, we followed the sampling scheme used in [19] where a 2D variable density random under-sampling pattern was used on Y-Z plane (as seen as Fig. 8(a)), which samples the low spatial frequency region densely with 2D variable density random sampling, but for Hybrid encoding, the a 2D hybrid variable density random under-sampling pattern was used on Y-Z plane (as seen as Fig.. 8(b)), which samples the low spatial frequency region densely with the random sampling mixing 1D variable density and 1D uniform random patterns. Non-linear conjugate gradient [19] algorithm was applied to reconstruct the image based on Eq. (13) for Fourier and Eq. (21) for hybrid encoding. Both wavelet transform and TV were adopted to sparsify the images. As seen as Fig. 27, two k -space raw datasets of 3D Hybrid (a) and Foureir (b) encoding, and their sampling patterns are illustrated. The right parallelograms are respectively sampling patterns of Fourier and Hybrid, and the white dots are coressponding sampling positions. They shows that the k -space raw data has been spreaded wildly in the 3D Hybrid encoding, which can benefit to apply CS reconstration [19].

Two 3D raw datasets (sagittal brain and knee) were used to simulate the proposed 3D Hybrid encoding and conventional Fourier encoding, scanned on a 3.0T commercial MR scanner (GE Healthcare, Waukesha, WI). The sizes of the simulated images both are $256 \times 256 \times 16$ and $256 \times 256 \times 32$ voxels. The 2D sampling patterns (as seen as Fig. 27) were done on the Y-Z plane from the full image size of 256×16 and 256×32 . The reduction factors which are about 2 and 3 were used to accelerate the data acquisition.

Fig. 28 (a, c, and d) compares the 3D reconstructed images for the brain dataset which has the reduction factor is 2.95. Fig. 28 (b, e and f) compares the 3D reconstructed images for the knee dataset which has the reduction factor is 3.39. Fig. 29 (a, c, and d) compares one slice of the reconstructed images on X-Y plane for the brain dataset which has the reduction factor is 2.95. Fig. 29 (b, e and f) compares one slice of the reconstructed images on X-Y plane for the knee dataset which has the reduction factor is 3.39.

Fig. 30 (a, c, and d) compares the 3D reconstructed images for the brain dataset which has the reduction factor is 1.89. Fig. 30 (b, e and f) compares the 3D reconstructed images for the knee dataset which has the reduction factor is 1.89. Fig. 31 (a, c, and d) compares one slice of the reconstructed images on X-Y plane for the brain dataset which has the reduction factor is 1.89. Fig. 31 (b, e and f) compares one slice of the reconstructed images on X-Y plane for the knee dataset which has the reduction factor is 1.89.

Table 1 compares the normalized mean square error (NMSE) and root mean square error (RMSE) between 3D Fourier and Hybrid encoding by different reduction factors. The results show that the proposed 3D Hybrid encoding method can reconstruct more high quality images than the conventional 3D Fourier encoding. And the proposed method is seen to visually preserve better resolutions and more details than the conventional 3D Fourier encoding method.

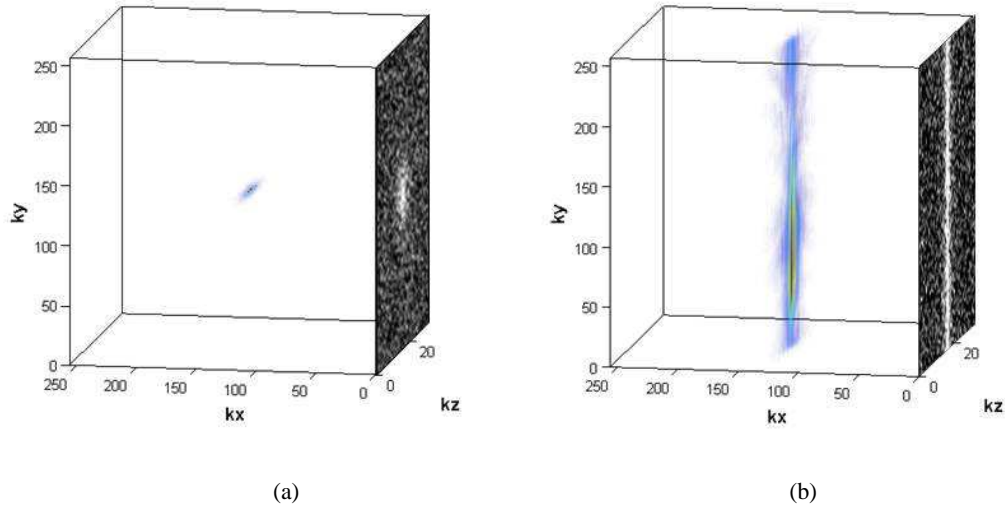
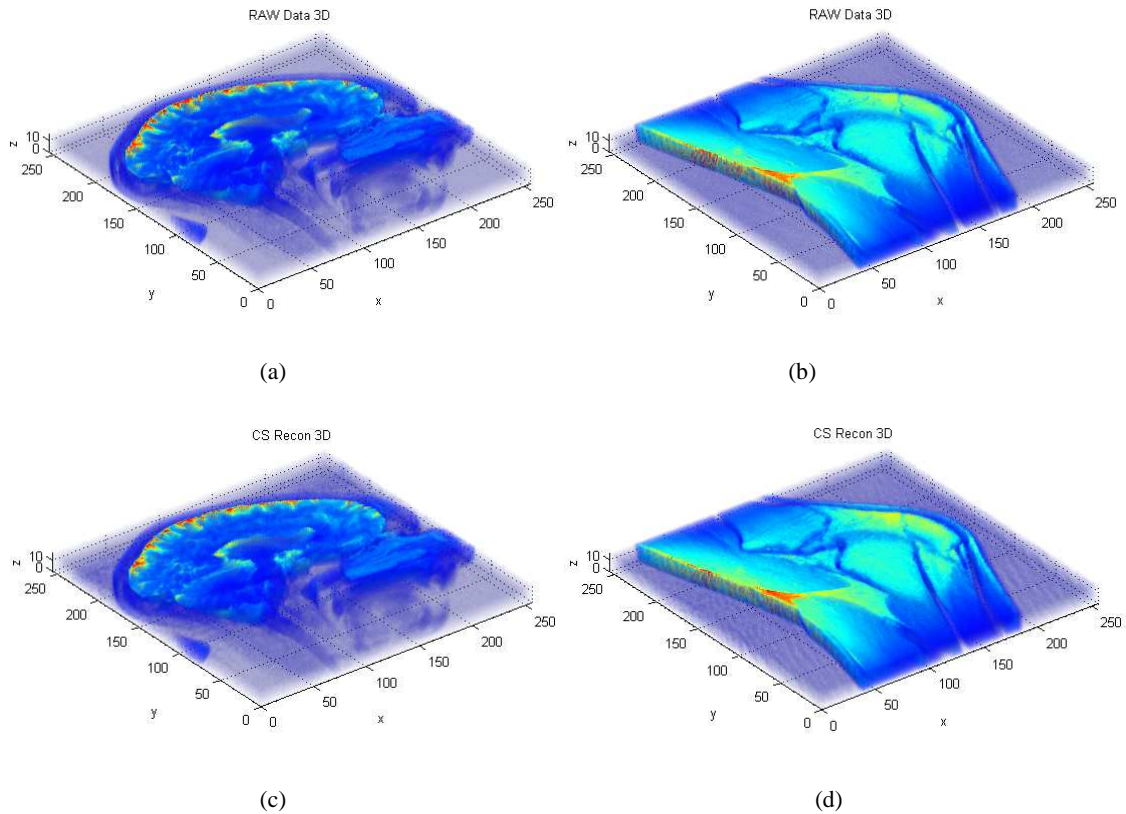


Fig.27 Illustration of the sampling patterns and k -space raw data of 3D Fourier (a) and Hybrid (b) encoding. The right parallelograms are respectively sampling patterns of Fourier and Hybrid, and the white dots are corresponding sampling positions.



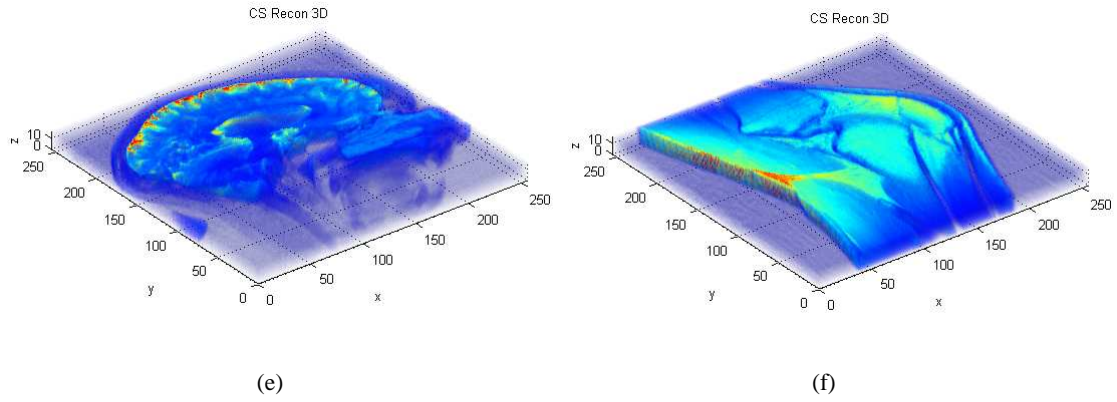
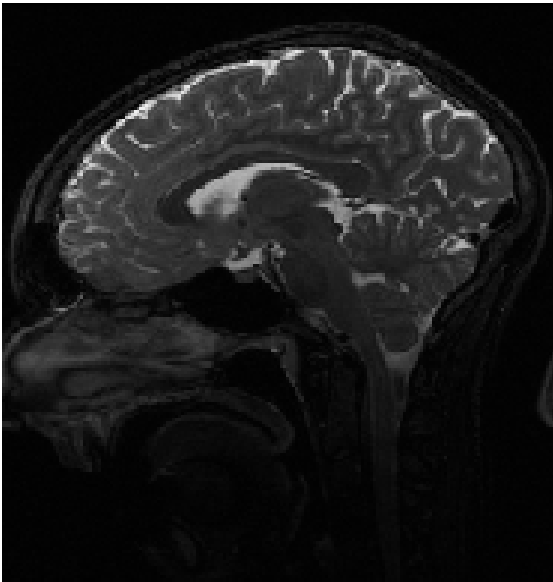
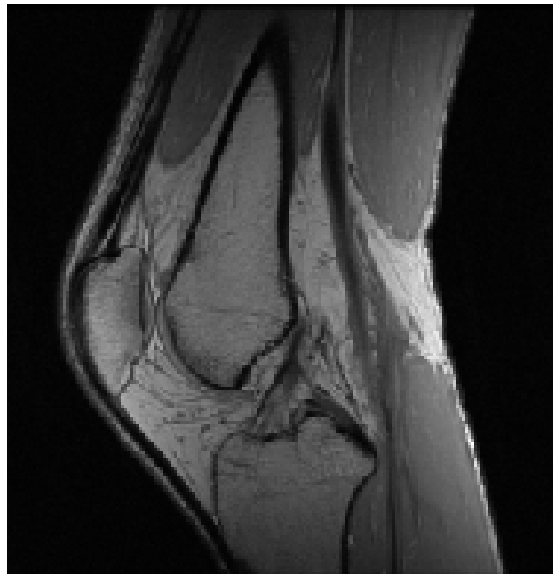


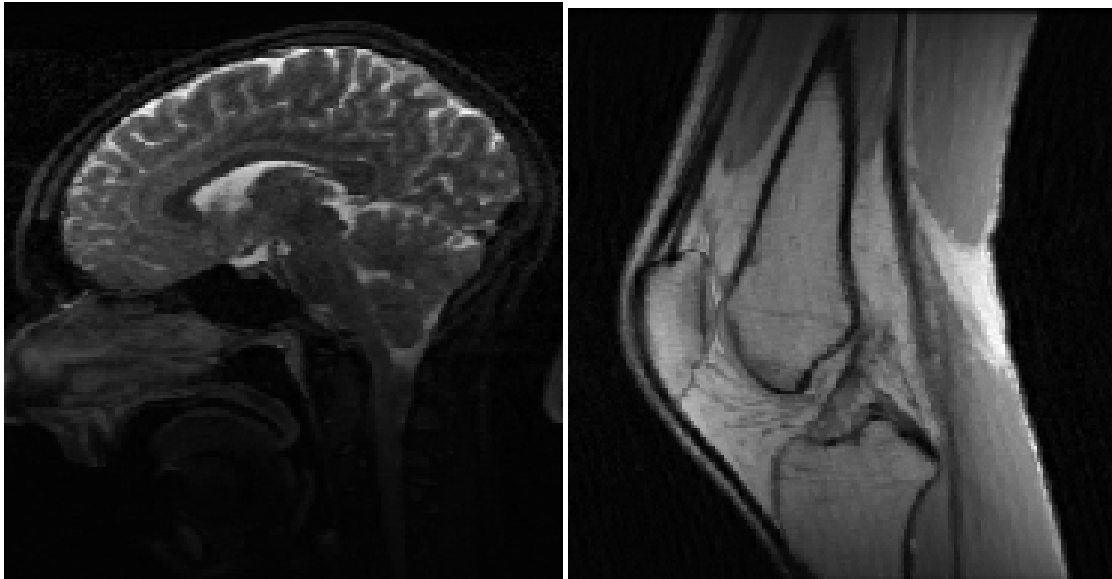
Fig. 28 3D $256 \times 256 \times 16$ images of brain (R=2.95) and knee (f) (R=3.39) of the reference (a, b), the CS recon of Fourier encoding(c, d), and the CS recon of Hybrid encoding (e, f)



(a)

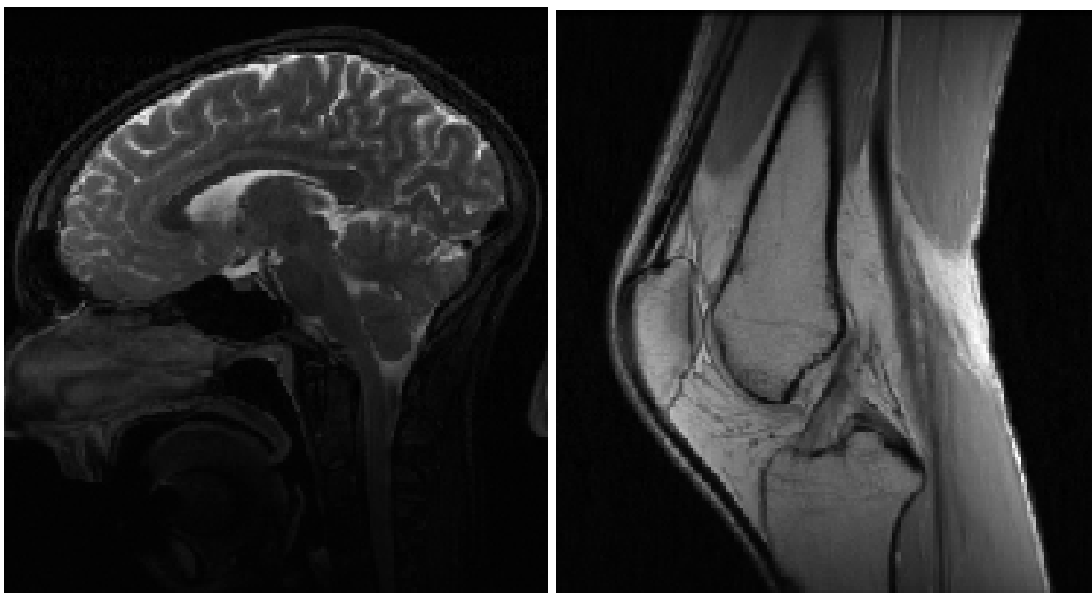


(b)



(c)

(d)



(e)

(f)

Fig.29 Illustration of one slice of the 3D $256 \times 256 \times 16$ reference (a, b) and the CS reconstruction 3D $256 \times 256 \times 16$ results (c, d, e and f) of sagittal human brain (e) ($R=2.95$) and knee (f) ($R=3.39$) comparing 3D Foureir encoding (c, d) and Hybrid encoding (e, f)

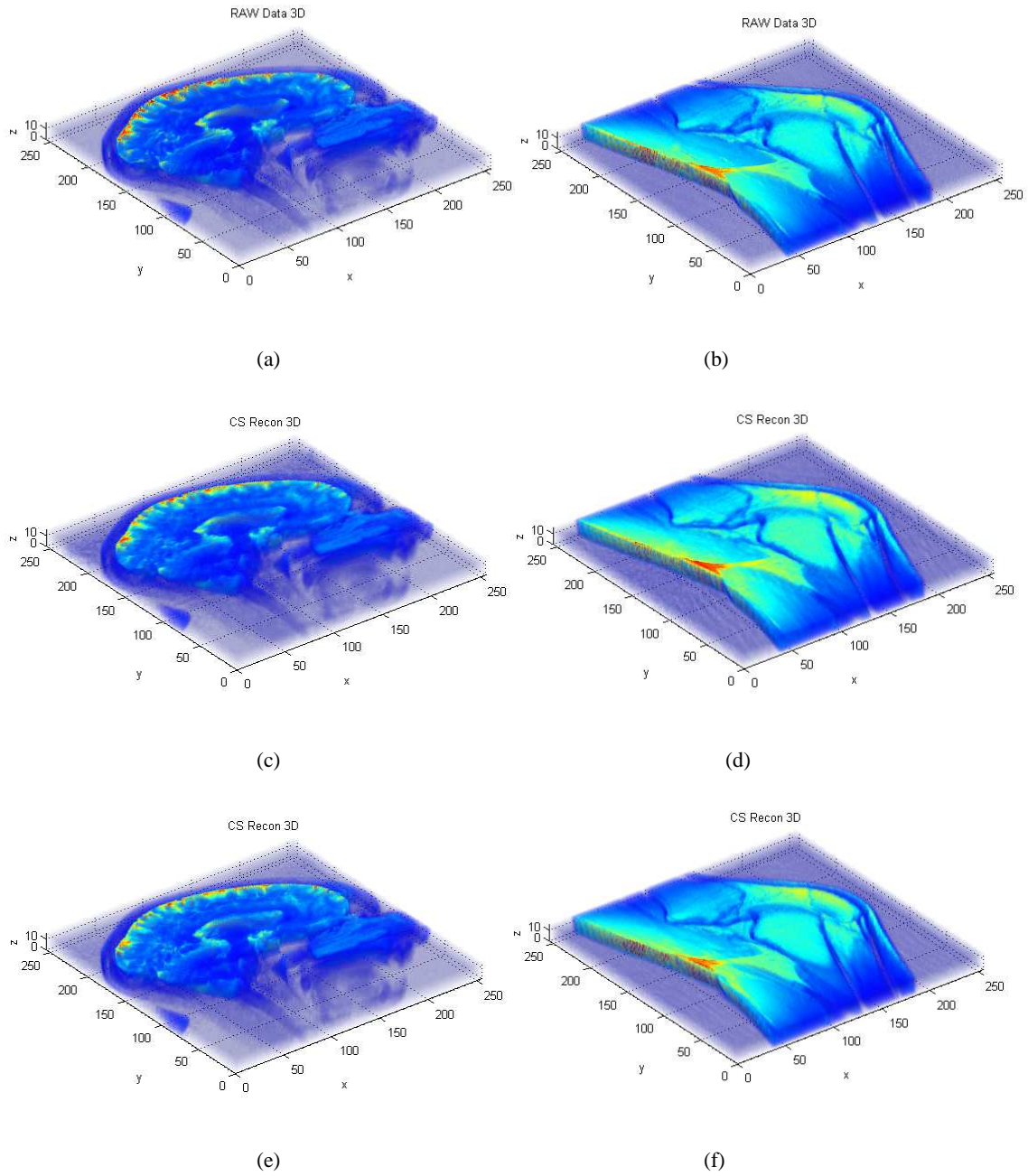
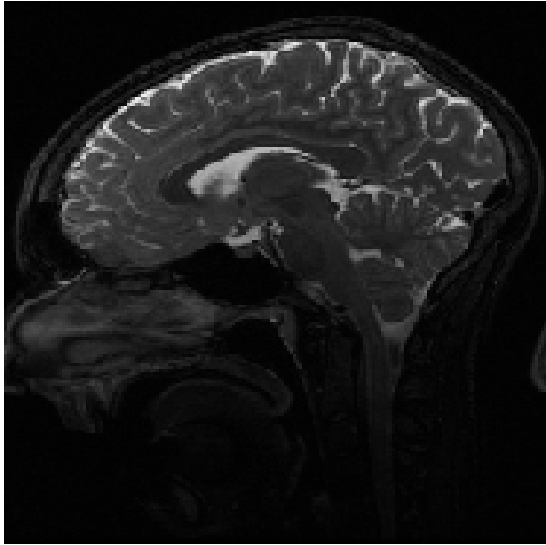
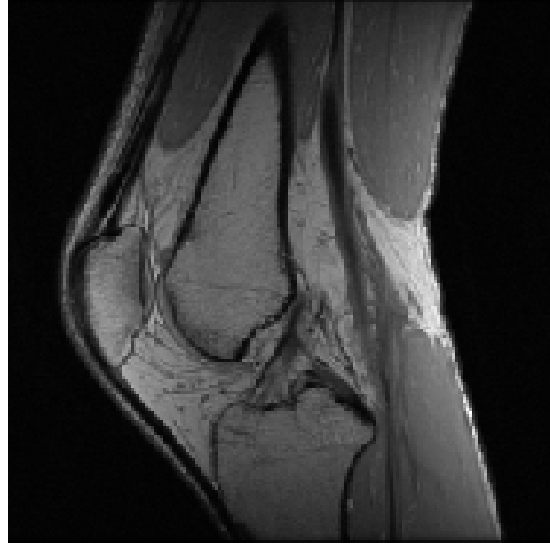


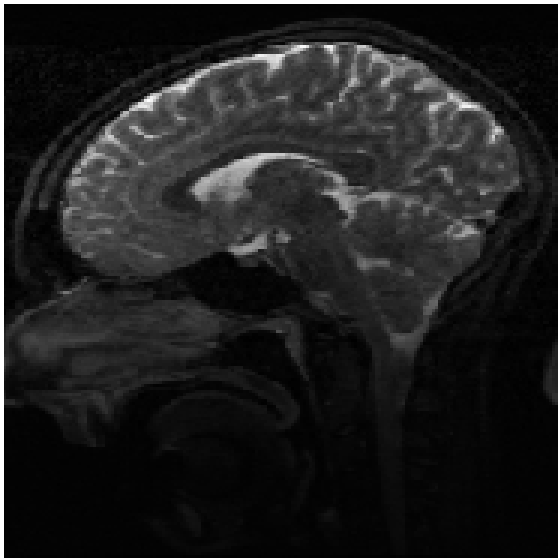
Fig. 30 3D $256 \times 256 \times 16$ images of brain ($R=1.89$) and knee (f) ($R=1.89$) of the reference (a, b), the CS recon of Fourier encoding(c, d), and the CS recon of Hybrid encoding (e, f)



(a)



(b)



(c)



(d)

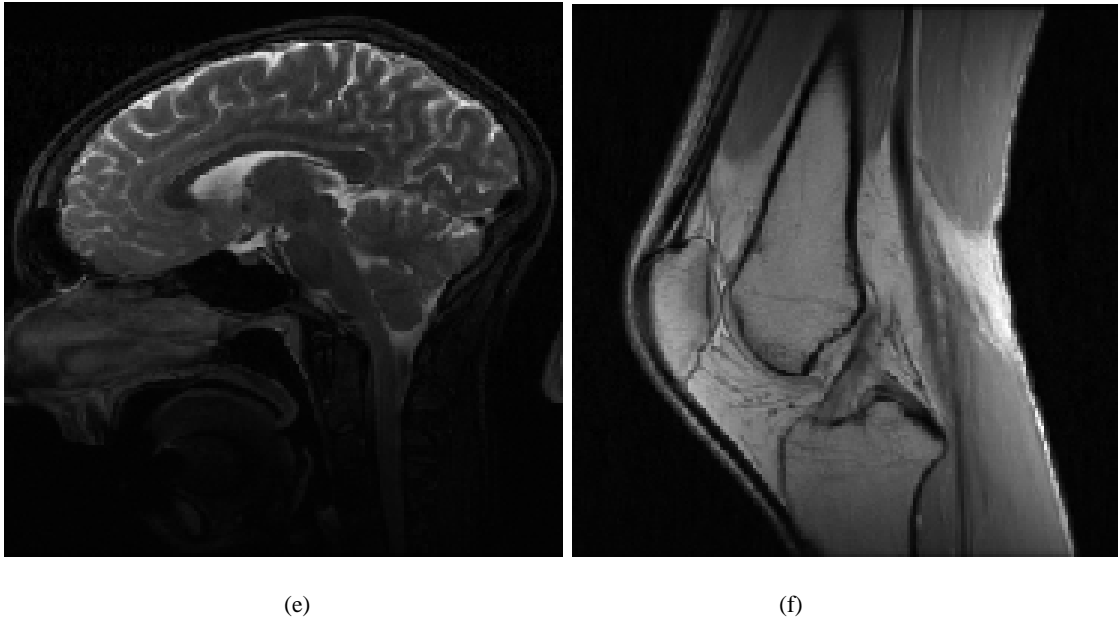


Fig.31 Illustration of one slice of the 3D $256 \times 256 \times 16$ reference (a, b) and the 3D $256 \times 256 \times 16$ CS reconstruction results (c, d, e and f) of sagittal human brain (e) ($R=1.89$) and knee (f) ($R=1.89$) comparing 3D Fourier encoding (c, d) and Hybrid encoding (e, f)

Type	Size	Method	NMSE		RMSE	
Reduction Factor			R=1.89	R=2.95	R=1.89	R=2.95
Brain	$256 \times 256 \times 16$	Fourier	0.0080	0.0120	0.0274	0.0337
		Hybrid	0.0060	0.0090	0.0238	0.0291
			R=1.97	R=3.10	R=1.97	R=3.10
Brain	$256 \times 256 \times 32$	Fourier	0.0065	0.0099	0.0240	0.0297
		Hybrid	0.0064	0.0092	0.0239	0.0287
			R=1.89	R=3.39	R=1.89	R=3.39
Knee	$256 \times 256 \times 16$	Fourier	0.0045	0.0077	0.0287	0.0374
		Hybrid	0.0022	0.0032	0.0200	0.0243

			R=1.97	R=3.44	R=1.97	R=3.44
Knee	256×256×32	Fourier	0.0053	0.0056	0.0300	0.0309
		Hybrid	0.0020	0.0034	0.0182	0.0239

Table 1. Simulation comparison of human brain and knee. The normalized mean square error (NMSE) and root mean square error (RMSE) between 3D Hybrid and Fourier encoding are calculated with different data sizes of $256 \times 256 \times 32$ and $256 \times 256 \times 16$, and reduction factors of 1.89, 1.97, 2.95, 3.10, 3.39 and 3.44.

4.2.1 Experiments of Phantoms

A ball phantom was scanned by the 1.5T MRI scanners (GE Healthcare, Waukesha, WI) with 3D GRASS pulse sequence and the 3D Hybrid encoding pulse sequences based on GRASS. One-channel body coil was applied to acquire the k -space raw dataset. As seen as the Fig. 32, the 3D $256 \times 256 \times 32$ results demonstrate the proposed 3D Hybrid encoding different from the conventional 3D Fourier encoding spread out the image energy in the k -space. The proposed method has some benefits for the CS reconstructions.

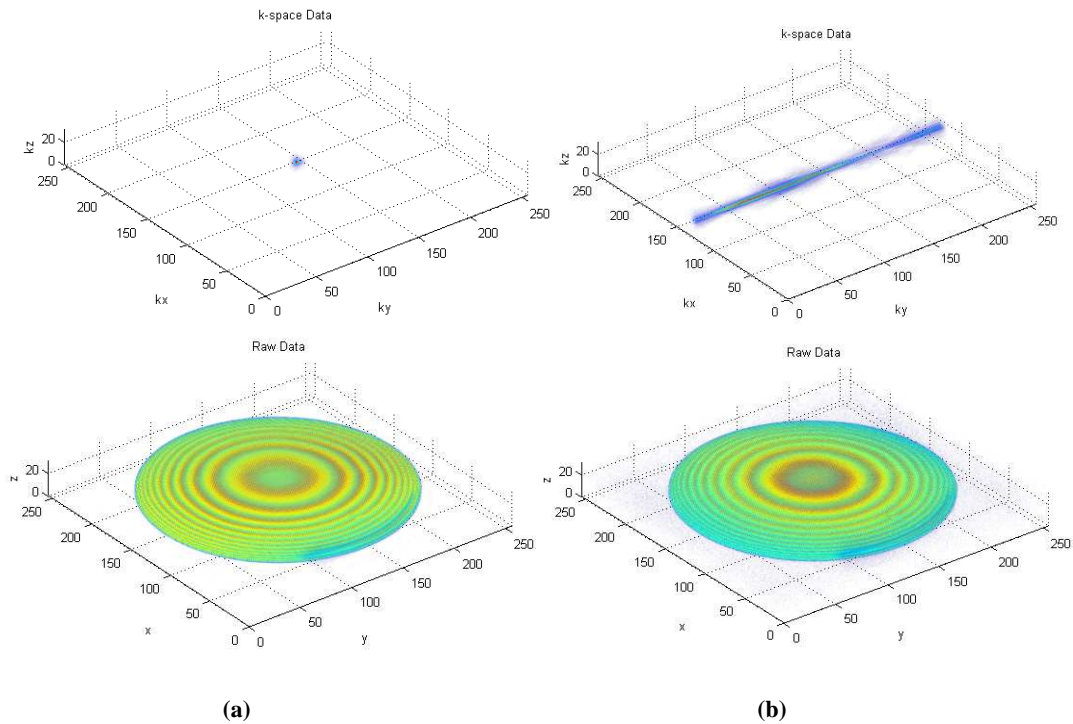


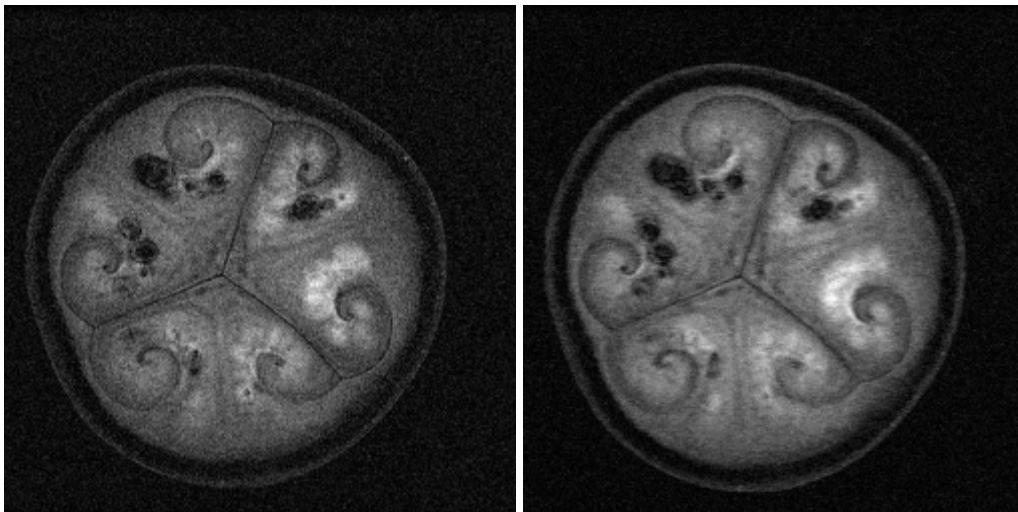
Fig. 32 *k*-space raw data and decoded image data of 3D Fourier (a) and Hybrid (b) encoding.

4.2.3 Experiments of Watermelon

In actual experiments, one watermelon was scanned on a 3.0T commercial MRI scanner (GE Healthcare, Waukesha, WI) with one standard body coil using both the 3D Hybrid encoding and Fourier encoding pulse sequences. For Hybrid encoding, a proposed pulse sequence based on a 3D GRASS pulse sequence (RF pulse duration: 1.536ms) was applied to sample *k*-space raw dataset. For Fourier encoding, the conventional 3D GRASS pulse sequence are applied as comparison (both with TE/TR: 5/15 ms; BW: 31.50 kHz; FOV: 24 cm²; thickness: 6.5 cm full data size: 256×256×32). The datasets were acquired with full Nyquist sampling and then manually under-sampled by removing some data points based on the designed sampling patterns (as seen as Fig. 27). Here, the 2D under-sampling was done on the Y-Z plane from the full size of 256×32.

Fig. 33 shows comparison of 3D CS reconstructions between the proposed 3D Hybrid encoding and the conventional 3D Fourier encoding. The reduction factors which are 2.07 and 3.0 were used to accelerate the data acquisitions. The proposed Hybrid method and the conventional Fourier method have same imaging time, and same parameters of the pulse sequences, such as, TE, TR, data size, thickness, FOV, etc.. The images reconstructed from the full data were used as the reference for comparison.

Table 2 compares the normalized mean square error (NMSE) and root mean square error (RMSE) between 3D Hybrid and Fourier encoding of the watermelon raw datasets, scanned by the proposed and conventional sequences. All experiments illustrate that the experimental results agree with the conclusion from simulations that the proposed 3D Hybrid encoding method can reconstruct more high quality images than the conventional 3D Fourier encoding, and the proposed method can visually preserve better resolutions and more details. The comparisons of the NMSE and RMSE also sustain these conclusions.



(a)

(b)

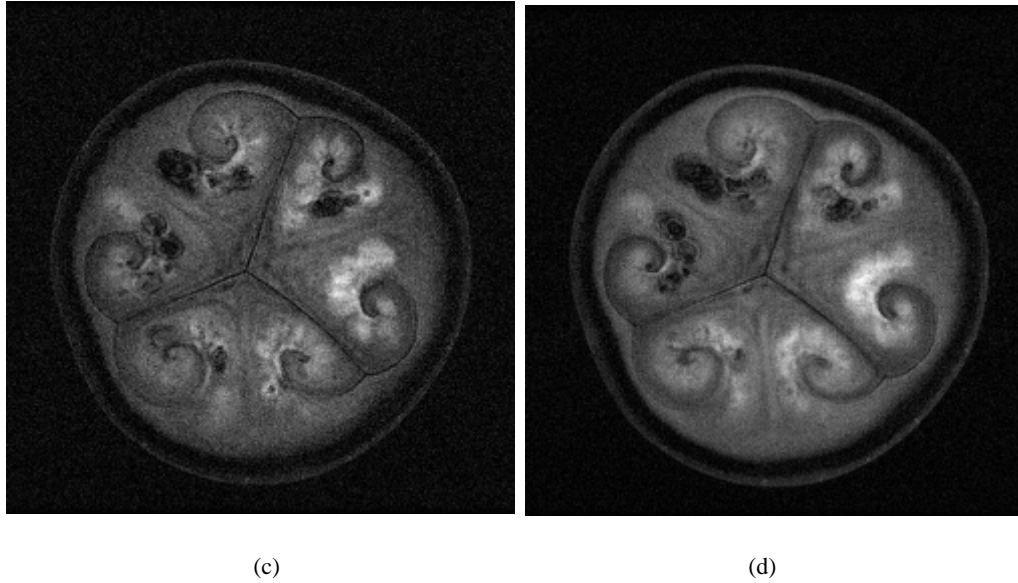


Fig.33 Comparison of one slice of the watermelon references(a,c) and CS reconstruction (R=3.0) watermelon results (b, d) of 3D Fourier (a,b) and Hybrid (c,d) encoding with the data size of $256 \times 256 \times 32$

Type	Size	Method	NMSE		RMSE	
Reduction Factor			R=2.07	R=3.00	R=2.07	R=3.00
Watermelon	$256 \times 256 \times 32$	Fourier	0.0161	0.0192	0.0435	0.0475
		Hybrid	0.0133	0.0167	0.0368	0.0413

Table 2. Comparison of 3D watermelon raw dataset. The normalized mean square error (NMSE) and root mean square error (RMSE) between 3D Hybrid and Fourier encoding are calculated with different data size of $256 \times 256 \times 32$, and reduction factors of 2.07 and 3.00.

4.2.4 In Vivo Experiments of Human Knee

In the first *in vivo* experiment, human knee was scanned on a 1.5T commercial MRI scanner (GE Healthcare, Waukesha, WI) with one standard 8-channel knee coil using both the 3D Hybrid encoding and 3D Fourier encoding pulse sequences. For Hybrid encoding, a proposed pulse

sequence based on a 3D GRASS pulse sequence (RF pulse duration: 6.144ms) is applied to scan. For Fourier encoding, the conventional 3D GRASS pulse sequence are applied as comparison (both with TE/TR: 15/40 ms; BW: 5.95 kHz; FOV: 20 cm²; thickness: 4.0 cm; full data size: 256×256×32; Flip angle: 5°). The datasets were acquired with full Nyquist sampling and then manually under-sampled by removing some data points based on the designed sampling patterns (as seen as Fig. 23). Here, the 2D under-sampling was done on the Y-Z plane from the full size of 256×32. A reduction factor of 2.0 was used to accelerate the data acquisitions. After recovering each channel under-sampled dataset, the SoS method was applied to compose the final reconstructed images. The SoS image from the full data were used as the reference for comparison.

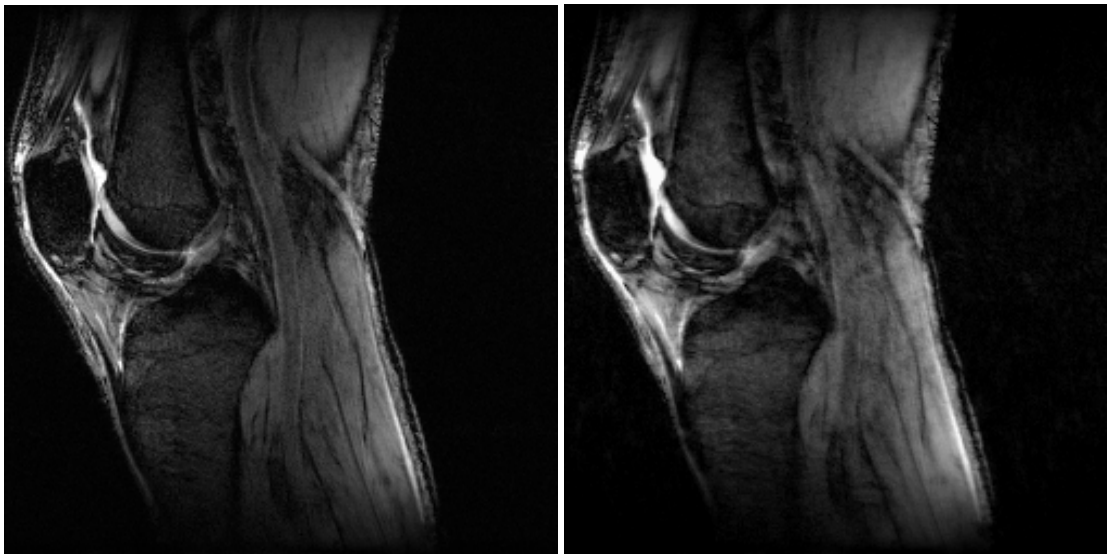
Fig. 34 shows comparison between the proposed 3D Hybrid encoding and the conventional 3D Fourier encoding. The proposed method and the conventional method both have same imaging time, and same parameters of the pulse sequences, such as, TE, TR, data size, thickness, FOV, spacing, etc.. The images reconstructed from the full data were used as the reference for comparison. According to the results, they show that the *in vivo* experiment agree with that the proposed Hybrid encoding preserves more details and sharp edges than the Fourier encoding.

In the second *in vivo* human knee experiment, human knee was scanned on a 3.0T commercial MRI scanner (UCSF, San Francisco, CA) with one HD 8-channel knee coil using both the 3D Hybrid-encoding and 3D Fourier encoding pulse sequences. For Hybrid encoding, a proposed pulse sequence based on a 3D GRASS pulse sequence (RF pulse duration: 1.536ms) is applied to sample. For Fourier encoding, the conventional 3D GRASS pulse sequence are applied as comparison (both with TE/TR: 5/26 ms; BW: 31.50 kHz; FOV: 20 cm²; thickness: 6.5 cm; full data size: 256×256×34; Flip angle: 10°). The datasets were acquired with full Nyquist sampling and then manually under-sampled by removing some data points based on the designed sampling patterns (as seen as Fig. 8). Here, the 2D under-sampling was done on the Y-Z plane from the full size of 256×34. A reduction factor of 2.0 was used to accelerate the data acquisitions. After

recovering each channel under-sampled dataset, the SoS method was applied to compose the final reconstructed images. The SoS image from the full data were used as the reference for comparison.

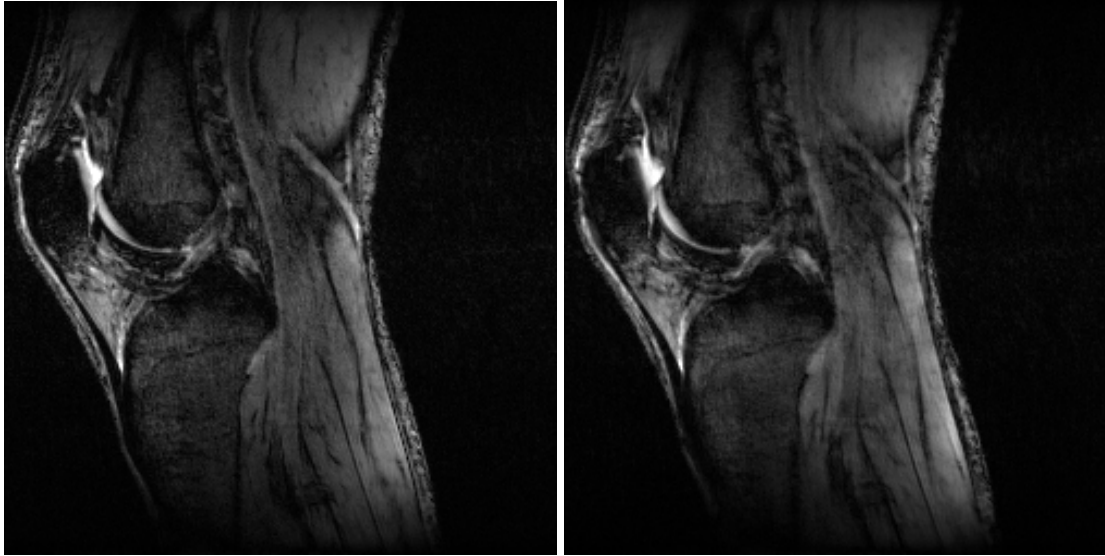
Fig. 35 shows comparison between the proposed 3D Hybrid encoding and the conventional 3D Fourier encoding. The proposed method and the conventional method both have same imaging time, and same parameters of the pulse sequences, such as, TE, TR, data size, thickness, FOV, spacing, etc.. The images reconstructed from the full data were used as the reference for comparison. According to the results, they show that the *in vivo* experiment agree with that the proposed Hybrid encoding preserves more details and sharp edges than the Fourier encoding.

Table 3 compares the normalized mean square error (NMSE) and root mean square error (RMSE) between 3D Hybrid and Fourier encoding of $256 \times 256 \times 34$ *in vivo* human knee raw datasets from the second *in vivo* human knee experiment. The comparisons of the NMSE and RMSE illustrate that the proposed 3D Hybrid encoding method can recover more high quality images than the conventional 3D Fourier encoding, and the proposed method can visually preserve better resolutions and more details.



(a)

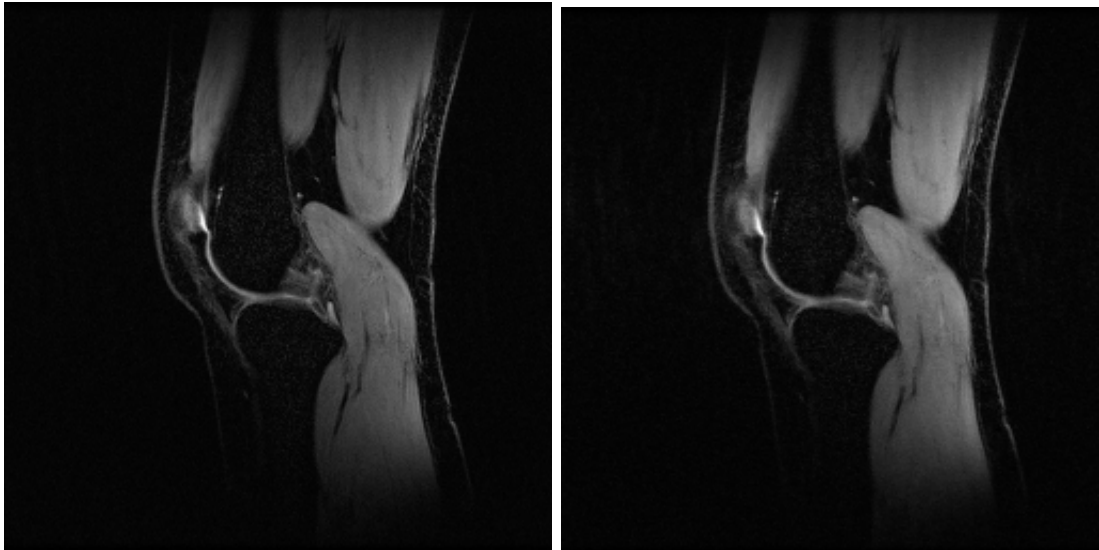
(b)



(c)

(d)

Fig.34 Illustration of one slice of the references (a, c) and CS reconstruction ($R=2.1$) in vivo knee results (b, d) of 3D Fourier encoding (a,b) and Hybrid (c,d) with the data size of $256 \times 256 \times 32$



(a)

(b)

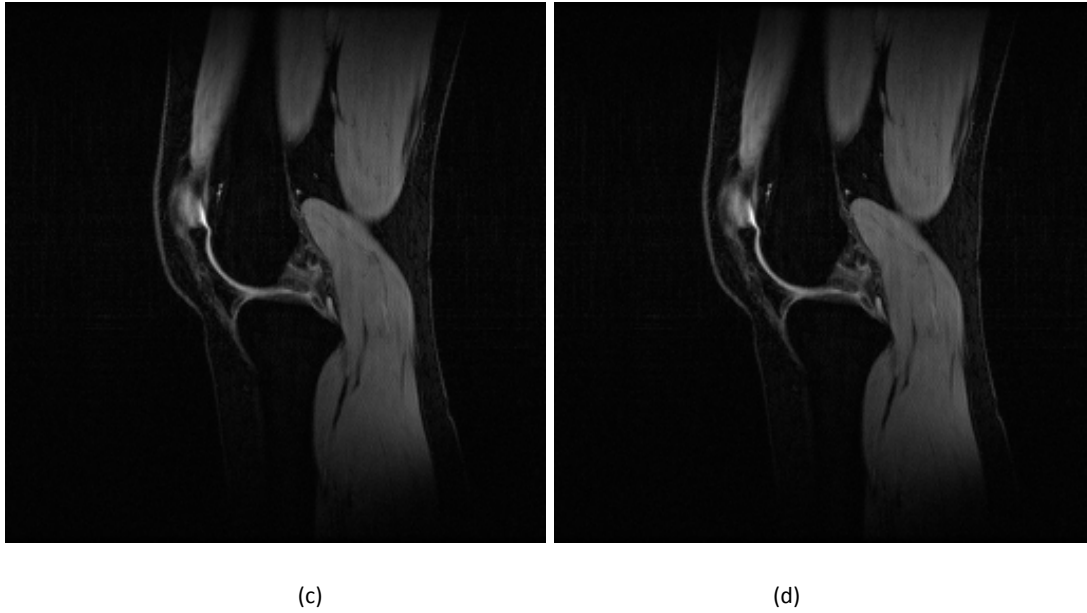


Fig.35 Illustration of one slice of the references (a, c) and CS reconstruction (R=2.0) in vivo knee results (b, d) of 3D Fourier encoding (a,b) and Hybrid (c,d) with the data size of $256 \times 256 \times 34$

Type	Size	Method	NMSE		RMSE	
Reduction Factor			R=1.99	R=2.99	R=1.99	R=2.99
<i>in vivo</i> knee	$256 \times 256 \times 34$	Fourier	2.6e-3	0.0129	1.1e-2	0.0253
		Hybrid	8.2e-11	0.0119	1.8e-6	0.0222

Table 3. Comparison of 3D *in vivo* human knee raw dataset. The normalized mean square error (NMSE) and root mean square error (RMSE) between 3D Hybrid and Fourier encoding are calculated with different data size of $256 \times 256 \times 34$, and reduction factors of 1.99 and 2.99.

4.3 Pseudo 2D Random Sampling

4.3.1 Bloch Simulation

Bloch simulations were carried out to compare the reconstruction results of the proposed pseudo 2D random sampling with the existing 1D random sampling and the desired ideal 2D random sampling. For validating the proposed pulse sequences, Bloch simulation [66] was done to demonstrate the feasibility of all sampling schemes by the conventional existing pulse sequences and the proposed pulse sequence designed in Fig. 18. A Shepp-Logan phantom is used as the desired object. The image of size 128×128 is reconstructed from the simulated data using the nonlinear conjugate gradient (NCG) algorithm and wavelet transformation. Fig. 36 shows the reconstruction results with the proposed sampling, the existing 1D sampling and the ideal 2D random sampling. Because the desired ideal 2D random sampling cannot be implemented by the existing pulse sequences, its full k -space data are from the Bloch simulation of the existing 1D random sampling and its sampling pattern is manually generated on computers. The sampling patterns of the existing 1D random sampling and the pseudo 2D random sampling both have their Bloch corresponding simulations realized by the existing pulse sequences and the proposed pulse sequence designed in Fig. 18. Here, all reduction factors are 2.0. The initial recon image by zero filling with density compensation (zfw/dc) of the 1D random sampling shows undersampling artifacts (ripples horizontally in background), but the initial recon image by zero filling with density compensation (zfw/dc) of the proposed pseudo 2D random sampling is seen to be as free artifacts as the initial image by zero filling with density compensation (zfw/dc) of the ideal 2D random sampling. The CS recon results by total variation (TV) illustrate the pseudo 2D random sampling is closer to the ideal 2D random sampling than the existing 1D random sampling.

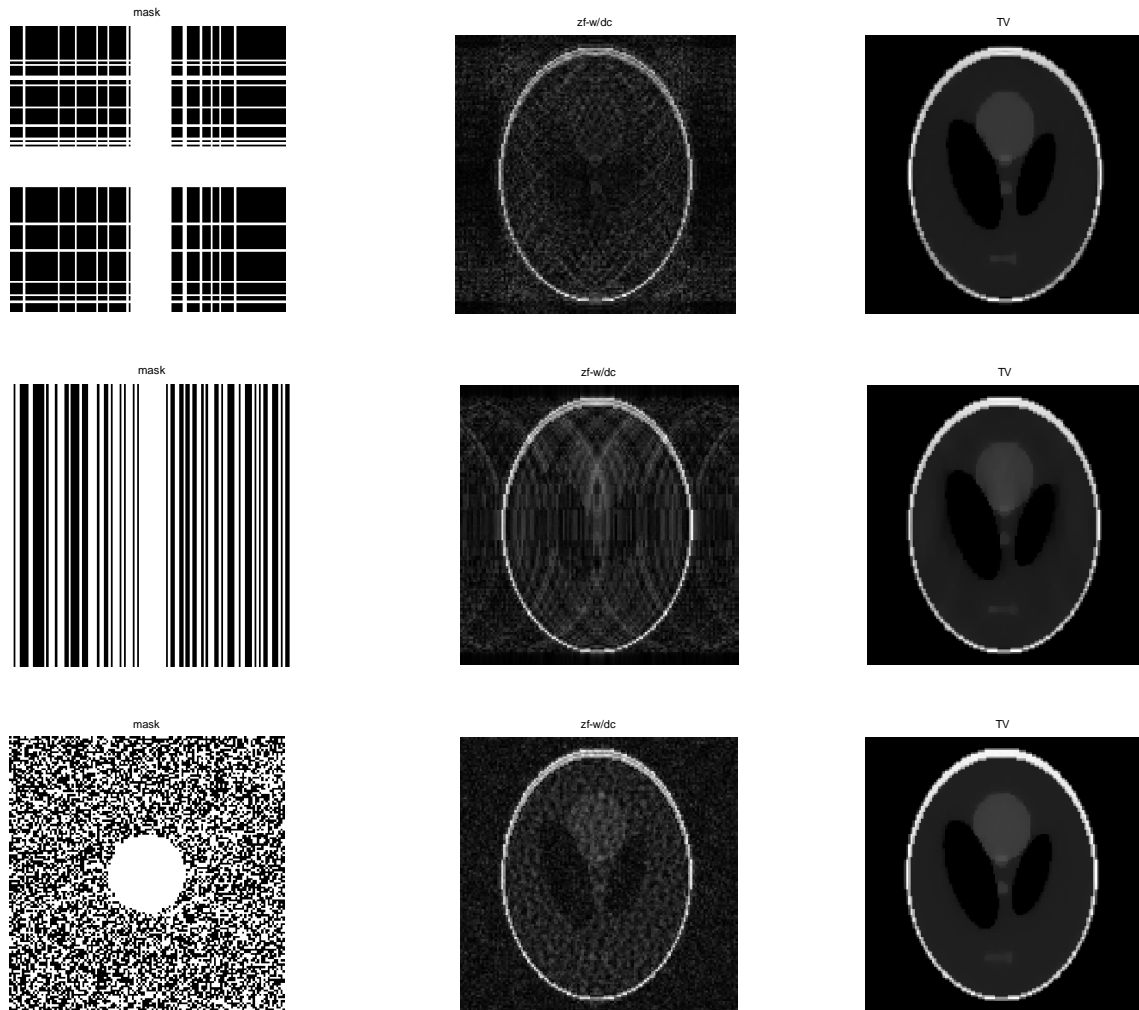


Fig. 36 Comparison of the proposed pseudo 2D random sampling scheme (1st row) and the existing 1D (2nd row) and 2D (3rd row) random sampling scheme. Mask means sampling pattern; zfw/dc means recon by zero filling with density compensation; TV means recon by total variation. The image size is 128×128 , and the reduction factor is 2.

4.3.2 Simulation of GE QA phantom

In the simulation with experimental data as seen as Fig. 37, a GE QA phantom was scanned using a gradient echo pulse sequence. The k -space data were acquired in full with size of 256×256 and then manually sampled by the proposed, existing and ideal sampling schemes to

simulate the desired reduction factors. Identity transform was used as the sparse representation in Eq. (33). The reduction factors of 2 and 2.86 were used. The nonlinear conjugate gradient (NCG) algorithm and total variation (TV) as Ref. [19] are used to reconstruct results. The recon results show that the proposed pseudo 2D random sampling scheme performs similar to the ideal 2D random sampling scheme, and is superior to the existing 1D random sampling scheme.

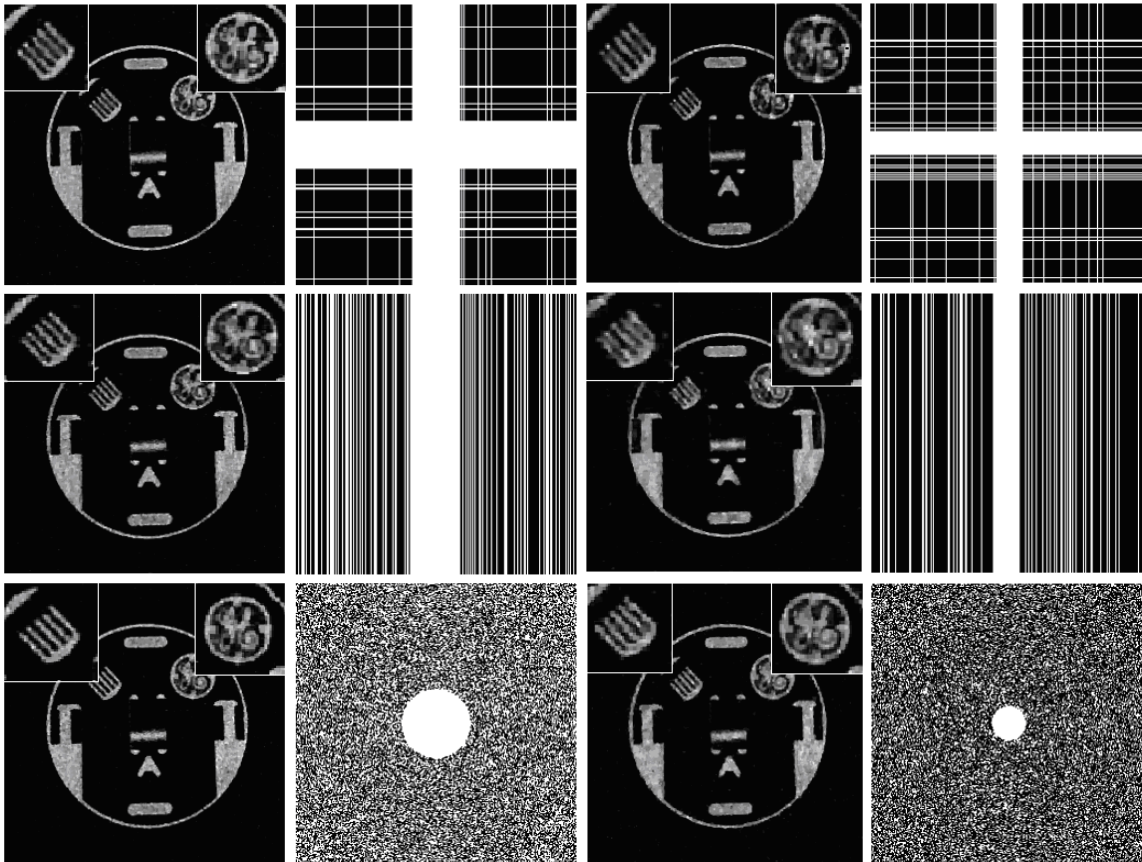


Fig. 37 GE QA Phantom reconstruction results and the corresponding sampling patterns of the pseudo 2D, 1D random and 2D random sampling methods. A reduction factor of 2 (left) and 2.86 (right) is used.

5. Discussions and Future Works

Previously, we present and study the three proposed schemes to accelerate imaging speed and improve image quality. Although these methods have been further studied, there are still some challenging issues required to be overcome. The following problems are discussed and further researched to enhance the current proposed schemes in the future.

5.1 Co-registration and 3D Acquisition of Cross-GRAPPA

Currently, a simple model is used in this study to characterize the inconsistency between data acquired with orthogonal readouts. This model is primarily for the inconsistency caused by eddy current and may not be able to correct the inconsistency due to other effects. The superior results of Cross-GRAPP in our study suggest the model is sufficiently appropriate for brain experiments due to its relatively low chemical shift effects. In addition, spin echo sequence is preferred to gradient echo sequence for Cross-GRAPP. This is because gradient echo sequence is known to be more susceptible to field inhomogeneity and chemical shift effects, and thus the swapping of phase and frequency encoding directions in Cross-GRAPPA results in more significant inconsistency between the data acquired with orthogonal readout directions. The inconsistency can be reduced by increasing the readout bandwidth, increasing the acquisition matrix, or using an in phase TE. The model for registering the data with orthogonal readout directions primarily considers misalignment in k -space. It works well in the brain region as shown in this study. More comprehensive co-registration methods, such as those in Refs. [76-79], will be studied for challenging scenarios (e.g., gradient echo sequence or regions with significant fat) in future work. In addition, the Nelder-Mead algorithm [53, 54] used for data registration is known to be heuristic and can converge to a non-stationary point. More sophisticated nonlinear minimization algorithms will also be explored. The idea of localized calibration was used in Ref. [42] with

some success. Similar idea can be used in Cross-GRAPPA where full ACS data are available along the undersampled direction and can be divided into subsets for local calibration. Optimization of the size of subsets needs further study.

In clinical applications, GRAPPA with 3D acquisition has gained more and more interests in recent studies [80-82]. The proposed Cross-GRAPPA can be easily extended from 2D to 3D acquisitions. Fig. 38 illustrates the sampling patterns of 3D GRAPPA and 3D Cross-GRAPPA, assuming the readout direction for conventional GRAPPA is k_x . In 3D Cross-GRAPPA, the ACS lines need to be orthogonal to k_x direction, and thus can be acquired either along k_y , k_z or a combination of both directions as shown in Fig. 38(b). A comprehensive study of 3D Cross-GRAPPA is beyond the scope of this paper and will be further investigated in future work.

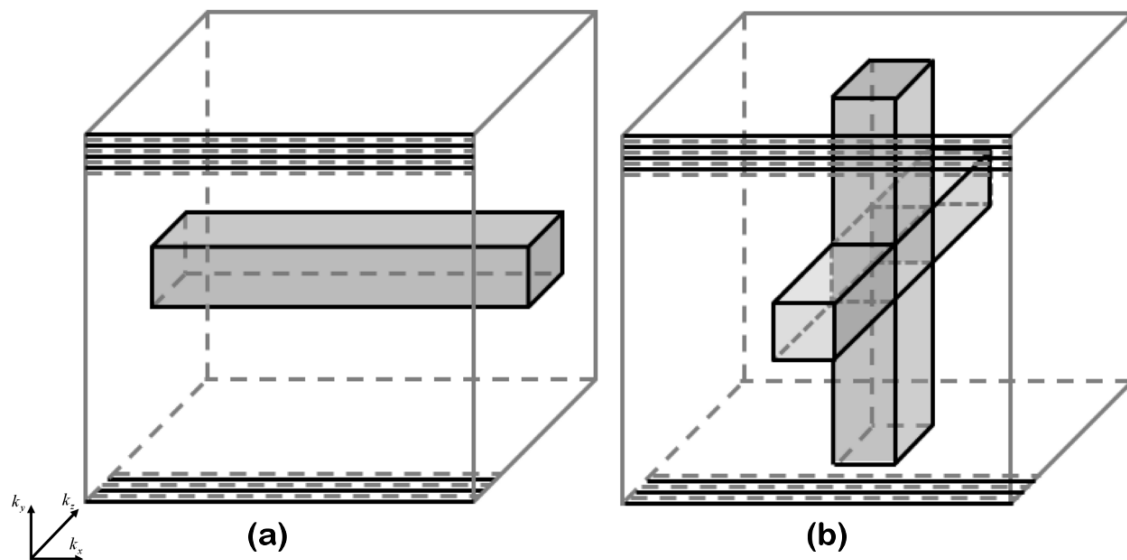


Fig. 38 Illustrations of sampling schemes for 3D GRAPPA (a) and 3D Cross-GRAPPA (b). The solid black lines represent fully sampled readout lines, the dash gray lines represent missing lines, and the gray boxes represent 2D fully sampled ACS regions.

5.2 Contrast of Hybrid-Encoded MRI

The current studies of the proposed Hybrid-encoded method show that it suggests a significant improvements comparing to the conventional Fourier-encoded method. But there are some problems required to be further discussed.

Firstly, the differences of the flip angles of the proposed method are not stable for any masses, such as water, fat, muscle, whiter matter, gay matter, etc. However, the differences of the flip angles of the conventional Fourier encoding method are stable. It means that the images from Hybrid encoding and Fourier encoding have difference contrasts because of the relations among all kinds of materials.

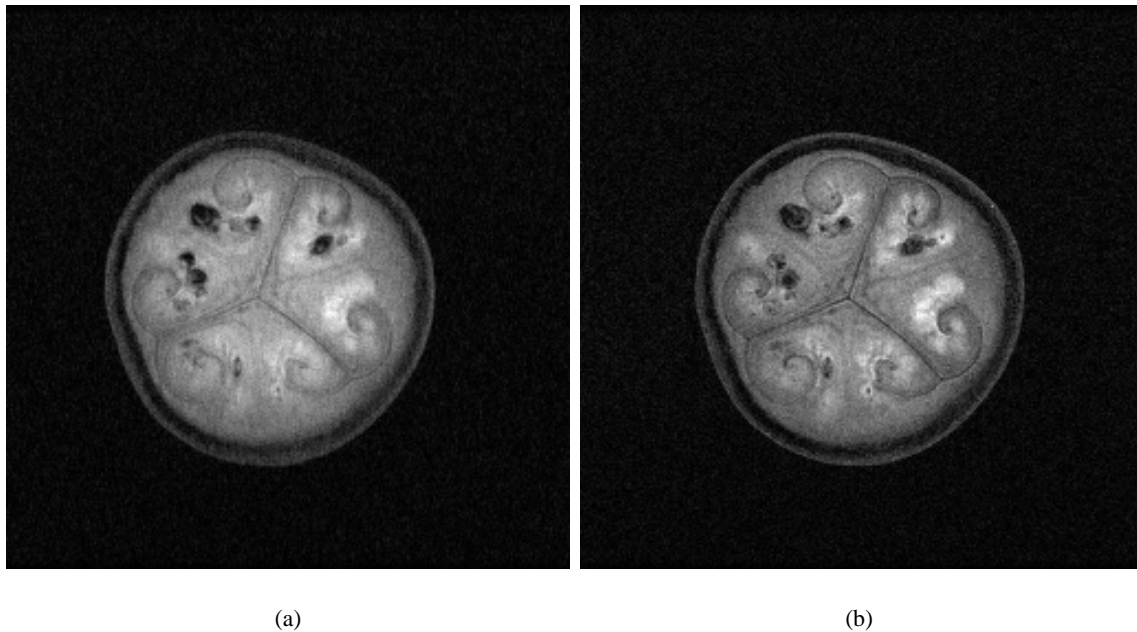


Fig.39 Actual axial watermelon experiments of 3D Fourier (a) and Hybrid (b) encoding methods.

The raw data size is $256 \times 256 \times 32$.

In the Axial watermelon experiments, human knees were scanned on a 1.5T MRI scanner (GE Healthcare, Waukesha, WI) with one channel body coil using both the proposed 3D pulse

sequence (RF pulse duration: 1.536ms) shown in Fig. 14 and the conventional 3D GRASS pulse sequence (TE/TR: 3/10 ms; BW: 125.0 kHz; FOV: 28 cm²; Flip angle = 5°; data size: 256×256×32). The experimental results illustrate that the contrasts of Hybrid encoding and Fourier encoding in some *in vivo* clinical experiments are totally different as seen as Fig. 39.

Secondly, the resolutions of Hybrid encoding and Fourier encoding have some distinctions. Usually, the receiver bandwidths of the pulse sequences are fixed in MRI scanners. The Hybrid encoding is equal for sampling every line along X direction per TR; but the Fourier encoding is variant. That is to say, the Fourier encoding will lose the signals in the high frequency region, because the receiver bandwidth is not enough large. However, the receiver bandwidth of the Hybrid encoding is enough since the *k*-space dataset has been incoherent and spread widely in the *k*-space. Therefore, the Hybrid encoding method can reserve more signals in the high frequency region than the Fourier encoding method.

Some *in vivo* experimental data are actually sampled from the commercial GE MRI scanners and the decoding were implemented in MATLAB (MathWorks, Natick, MA) on an HP XW8400 workstation with 2.33GHz CPU and 2GB RAM. In the first *in vivo* Axial experiments, human knees were scanned on a 1.5T MRI scanner (GE Healthcare, Waukesha, WI) with 8-channel standard knee coil using both the proposed 3D pulse sequence (RF pulse duration: 1.536ms) shown in Fig. 16 and the conventional 3D GRASS pulse sequence (TE/TR: 5/26 ms; BW: 5.96 kHz; FOV: 15 cm²; Flip angle = 5°). The decoded images from the raw *k*-space data of 256×256×34 was compared with the Fourier-encoded dataset. The Sum-of-Square (SoS) method is applied to combine decoded 8-channel datasets in image domain. Fig. 40 and 41 show comparison between the Hybrid method and Fourier encoding without fat saturation. The experimental results illustrate that the Hybrid method change the contrast between fat and water, and fat is suppressed more by the proposed Hybrid method than Fourier encoding. At the same time, the decoding speed of Hybrid is as similar as decoding Fourier.

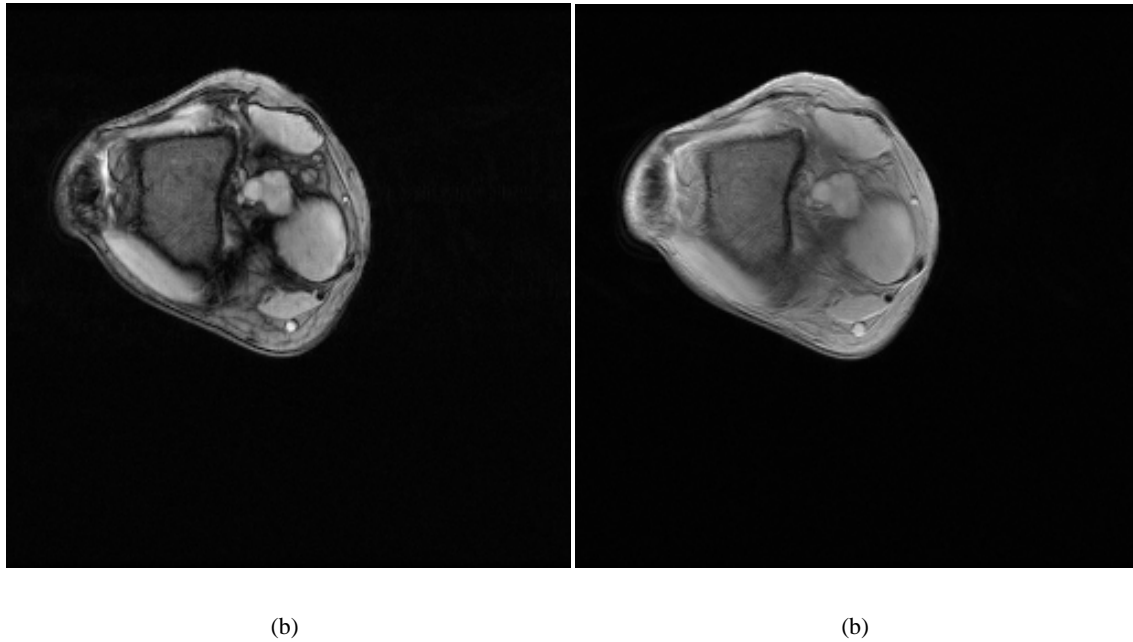


Fig.40 Axial *in vivo* human knee experiments of the 3D Hybrid (a) and Fourier (b) encoding methods without fat saturation.

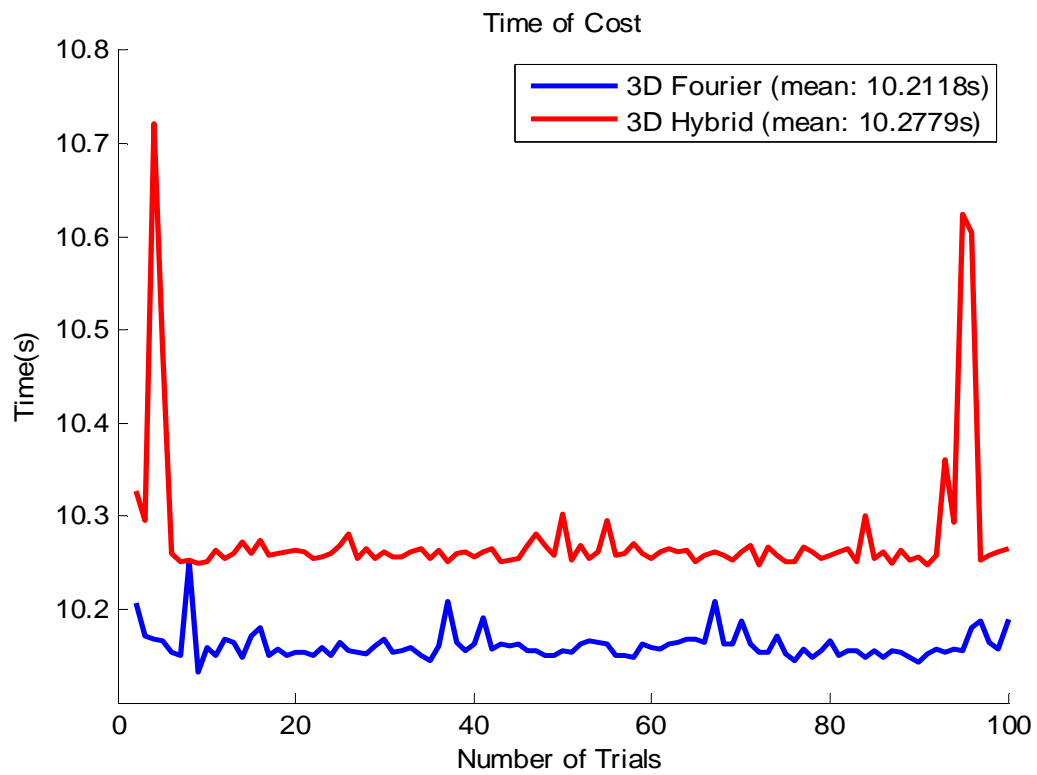


Fig.41 Time cost of 3D Fourier encoding using fast Fourier transform and 3D Hybrid encoding using the fast algorithm without fat saturation

In the second Sagittal *in vivo* experiments, human knees were scanned on a 3T commercial MRI scanner (UCSF, San Francisco, CA) with 8-channel HD knee coil using both the proposed 3D spoiled pulse sequence (RF pulse duration: 1.536ms) shown in Fig. 3 and the conventional 3D SPGR pulse sequence (TE/TR: 5/26 ms; BW: 31.25 kHz; FOV: 20 cm²; Flip angle = 18°). The decoded images from the raw *k*-space data of 256×256×32 was compared with the Fourier-encoded dataset. The Sum-of-Square (SoS) method is used to sum decoded 8-channel datasets in image domain. Fig. 42 and 43 compare one of slices between the Hybrid and Fourier methods without fat saturation. The Sagittal *in vivo* experimental results illustrate that the Hybrid method change the image contrast, and fat is suppressed more by the proposed Hybrid method than the conventional Fourier encoding method. Simultaneously, Hybrid decoding speed is as similar as Fourier decoding.



Fig.42 Sagittal *in vivo* human knee experiments of the 3D Hybrid (a) and Fourier (b) methods without fat saturation.

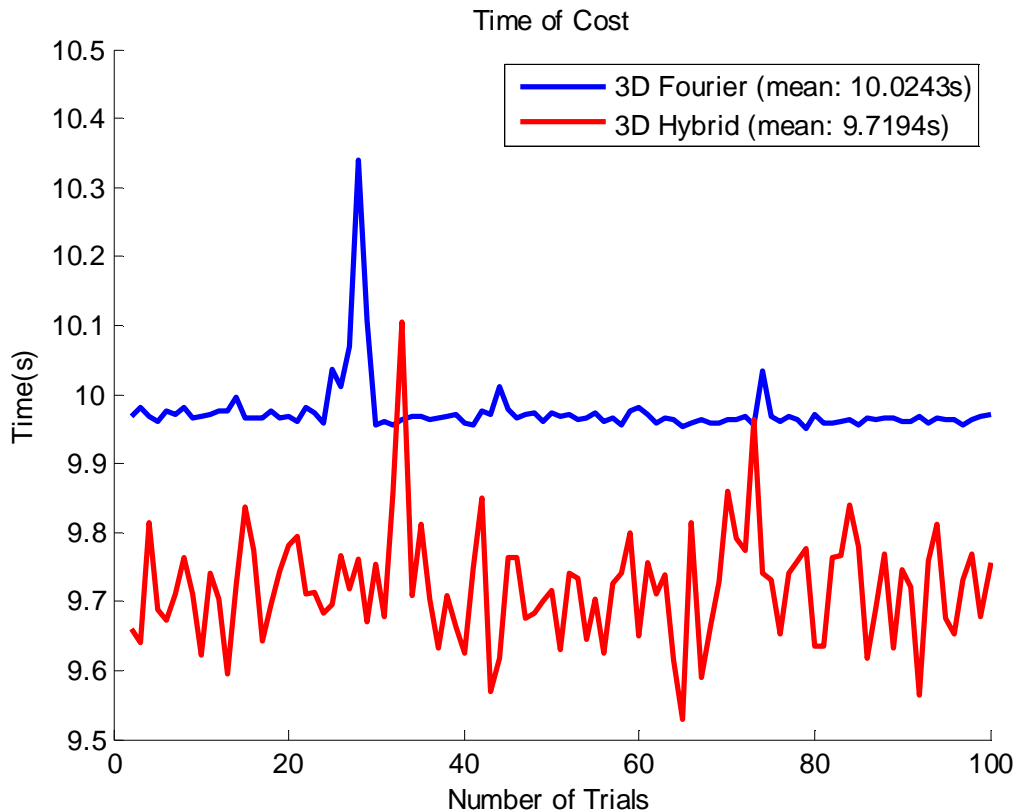


Fig.43 Time cost with 3D Fourier encoding using fast Fourier transform and 3D Hybrid encoding using the fast algorithm without fat saturation

Fig. 44 and 45 show comparison between the proposed method and Fourier encoding with and without fat saturation. Here, we compare the average k -space raw datasets between the proposed method and Fourier encoding with fat saturation and without fat saturation. The decoding images show that the proposed 3D Hybrid encoding method can change k -space raw data and preserve the data in the high frequency region. One slice of the images shows that the proposed 3D Hybrid encoding method can achieve different contrasts from the conventional 3D Fourier encoding method. The proposed method exploits a special non-Fourier random encoding pulse sequence to generate inhomogeneous B1 field, thus the signal contrast of fat and other tissues is changed comparing the conventional Fourier encoding method. Because, spatially varying flip angles across the FOV may lead to B1 inhomogeneity that result in an insufficient fat

sat pulse and thus lead to incompletely saturated fat signal [86]. However, this theoretical expiation is still fuzzy for clinic applications, further studies should be done in the future.

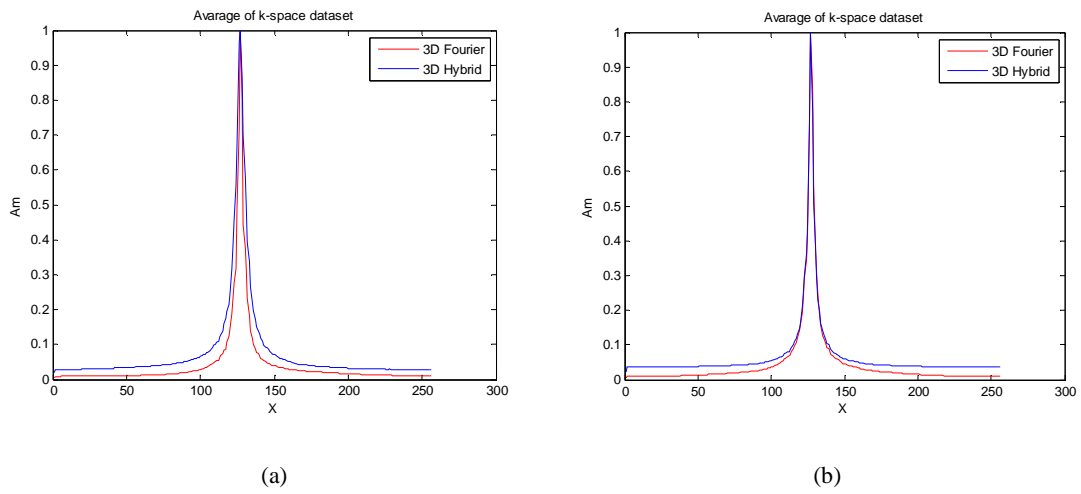


Fig. 44 Comparison of average k -space data of 3D Fourier and Hybrid encoding without fat saturation (a) and with fat saturation (b)





Fig. 45 Comparison of decoded images of 3D Fourier (a, b) and Hybrid (c, d) encoding without fat saturation (a, c) and with fat saturation (b, d).

5.3 Co-registration of Pseudo 2D Random Sampling

Currently, the co-registration model is not employed for Pseudo 2D random sampling. In common Bloch simulation, the co-registration model is also not required. However, for most actual experiments, the co-registration model is necessary for better reconstructions. Although, some applications without co-registration models are successfully completed, such as Hyperpolarization imaging [83], it is necessary to apply the co-registration model between the two orthogonal data for general imaging. Here, we can use the co-registration model as similar as the model of Cross-GRAPPA in Eq. (7). We need exploit the intersection points from the two orthogonal directions, to align the two raw datasets into one combined data, which will be used to recover by CS algorithms.

6. Summary

In sum, we overview our proposed schemes and completed works.

Firstly, we propose a new Cross-GRAPPA method for parallel imaging. The method improves conventional GRAPPA by integrating the new cross sampling and data co-registration procedure with the conventional calibration and reconstruction procedure. The method can reconstruct images from fewer amounts of ACS data than conventional GRAPPA, especially at the high ORFs. The phantom and *in vivo* human brain imaging experiments have demonstrated the advantages of this proposed approach. We anticipate that the proposed Cross-GRAPPA scheme can bring benefits to other 2D and 3D GRAPPA applications.

Secondly, we propose a novel 3D hybrid random encoding scheme which integrates the benefits of both random encoding and Fourier encoding. The Fourier encoding with variable density sampling ensures signals with high SNR to be sampled densely, while random encoding spreads out the signal energy to allow high spatial frequency to be sampled adequately for preserving resolution. The circulant structure for random encoding also can allow efficient reconstruction algorithms. The computational complexity of CS reconstruction is about the same for both hybrid and Fourier encodings. The simulations and real experiments both have illustrated that the proposed hybrid encoding scheme outperforms Fourier encoding in preserving resolutions. We anticipate that the proposed hybrid encoding scheme can be applied into current applications of Fourier-encoded CS MRI.

Thirdly, we present a random Cartesian sampling technique for applications of CS in conventional MRI. The simulation results have shown promising results to accelerate imaging speed with high reconstruction quality. We anticipate that the real experiments can also achieve better reconstruction results than the actual 1D and ideal 2D random sampling.

7. Reference

- [1] Webb A. Introduction to biomedical imaging. New York: IEEE Press; 2003. p.157.
- [2] Ljunggren S. A simple graphical representation of Fourier-based imaging methods. *J Magn Reson* 1983; 54: 338-343.
- [3] Twieg DB. The k-trajectory formulation of the NMR imaging process with applications in analysis and synthesis of imaging methods. *Med Phys* 1983; 10(5): 610-621.
- [4] Blaimer M, Breuer F, Mueller M, Heidemann RM, Griswold MA, Jakob PM. SMASH, SENSE, PILS, GRAPPA: how to choose the optimal method. *Top Magn Reson Imaging* 2004; 15(4): 223-236.
- [5] Roemer PB, Edelstein WA, Hayes CE, Souza SP, Mueller OM. The NMR phased array. *Magn Reson Med* 1990; 16(2):192-225.
- [6] Heidemann RM, Ozsarlak O, Parizel PM, et al. A brief review of parallel magnetic resonance imaging. *Eur Radiol* 2003; 13: 2323-2337.
- [7] Pruessmann KP, Weiger M, Scheidegger MB, Boesiger P. SENSE: Sensitivity encoding for fast MRI. *Magn Reson Med* 1999; 42(5):952-962.
- [8] Griswold MA, Jakob PM, Nittka M, et al. Partially parallel imaging with localized sensitivities (PILS). *Magn Reson Med* 2000; 44:602-609.
- [9] King KF. ASSET-Parallel Imaging on the GE Scanner. In: 2nd International Workshop on Parallel MRI, Zurich, 2004.
- [10] Sodickson DK, Manning WJ. Simultaneous acquisition of spatial harmonics (SMASH): Fast imaging with radiofrequency coil arrays. *Magn Reson Med* 1997; 38(4):591-603.
- [11] Jakob PM, Griswold MA, Edelman RR, et al. AUTO-SMASH: a selfcalibrating technique for SMASH imaging: SiMultaneous Acquisition of Spatial Harmonics. *MAGMA*. 1998; 7:42-54.
- [12] Heidemann RM, Griswold MA, Haase A, et al. VD-AUTO-SMASH imaging. *Magn Reson*

- Med. 2001; 45:1066-1074.
- [13] Bydder M, Larkman DJ, Hajnal JV. Generalized SMASH imaging. *Magn Reson Med.* 2002; 47:160-170.
- [14] Wang J, Kluge T, Nittka M, et al. Parallel acquisition techniques with modified SENSE reconstruction mSENSE. In Proc. of the First Würzburg Workshop on Parallel Imaging Basics and Clinical Applications, Würzburg, Germany, 2001:89.
- [15] Kyriakos WE, Panych LP, Kacher DF, et al. Sensitivity profiles from an array of coils for encoding and reconstruction in parallel (SPACE RIP). *Magn Reson Med.* 2000; 44:301-308.
- [16] Griswold MA, Jakob PM, Heidemann RM, Nittka M, Jellus V, Wang J, Kiefer B, Haase A. Generalized autocalibrating partially parallel acquisitions (GRAPPA). *Magn Reson Med.* 2002; 47(6):1202-1210.
- [17] Candès EJ, Romberg J, Tao T. Robust uncertainty principles: Exact signal reconstruction from highly incomplete frequency information. *IEEE Trans. Information Theory* 2006; 52: 489-509.
- [18] Donoho D. Compressed sensing. *IEEE Trans. on Information Theory* 2006; 52: 1289-1306.
- [19] Lustig M, Donoho D, Pauly JM. Sparse MRI: The application of compressed sensing for rapid MR imaging. *Magn. Reson. Med.* 2007; 58: 1182-1195.
- [20] Gamper U, Boesiger P, Kozerke S. Compressed sensing in dynamic MRI. *Magn Reson Med.* 2008; 59: 365-373.
- [21] Liang D, Liu B, Wang J, Ying L. Accelerating SENSE using compressed sensing. *Magn. Reson. Med.* 2009. 62: 1574-1584.
- [22] Lustig M, Pauly JM. SPIRiT: Iterative self-consistent parallel imaging reconstruction from arbitrary k-space. *Magn Reson Med* 2010; 64(2):457-471.
- [23] Wang H, Liang D, King KF, Nagasekar G, Chang Y, Ying L. Improving GRAPPA using cross-sampled autocalibration data. *Magn Reson Med.* 2011; in press.

- [24] Haldar JP, Hernando D, Liang ZP. Compressed sensing in MRI with Non-Fourier encoding. *IEEE Trans. Medical Imaging* 2011; 30: 893-903.
- [25] Sebert F, Zou YM, Ying L. Compressed sensing MRI with random B1 field. In Proc. of the 16th ISMRM annual meeting, pp. 3151, May 2008.
- [26] Wang H, Liang D, King KF, Ying L. Toeplitz random encoding for reduced acquisition using compressed sensing. In Proc. of the 17th ISMRM annual meeting, pp. 2669, Apr. 2009.
- [27] Liang D, Xu G, Wang H, King KF, Xu D, Ying L. Toeplitz random encoding MR imaging using compressed sensing. In Proc. of the 6th IEEE ISBI conference, Boston, MA, USA, 2009, p. 270-273.
- [28] Wong E, "Efficient randomly encoded data acquisition for compressed sensing," in Proc. Int. Soc. Magn. Reson. Med., 2010, p. 4893.
- [29] Wiaux Y., Puy G., Gruetter R., Thiran J.-P., DeVillie D. V., Vandergheynst P., "Spread spectrum for compressed sensing techniques in magnetic resonance imaging," in *Proc. IEEE Int. Symp. Biomed. Imaging*, 2010, pp. 756–759.
- [30] Wang H, Liang D, King KF, Ying L. Three-dimensional hybrid-encoded MRI using compressed sensing. In Proc. of the 9th IEEE ISBI conference, Barcelona, Spain, Apr. 2012.
- [31] Wang H, Liang D, Ying L. Pseudo 2D random sampling for compressed sensing MRI. In Proc. of the 31st IEEE EMBS annual conference, Minneapolis, Minnesota, USA, 2009. p. 2672-2675.
- [32] Qu P, Wang C, Shen GX. Discrepancy-based adaptive regularization for GRAPPA reconstruction. *J. Mag Reson Imaging* 2006; 24(1):248-255.
- [33] Wang Z, Wang J, Detre JA. Improved data reconstruction method for GRAPPA. *Magn Reson Med.* 2005; 54(3):738-742. Erratum in: *Magn Reson Med.* 2006; 56(1):234.
- [34] Huo D, Wilson DL. Robust GRAPPA reconstruction and its evaluation with the perceptual difference model. *J. Mag Reson Imaging* 2008; 27(6):1412-1420.

- [35] Huang F, Li Y, Vijayakumar S, Hertel S, Duensing GR. High-pass GRAPPA: a image support reduction technique for improved partially parallel imaging. *Magn Reson Med* 2008; 59(3):642-649.
- [36] Nana R, Zhao T, Heberlein K, LaConte SM, Hu X. Cross -validation-based kernel support selection for improved GRAPPA reconstruction. *Magn Reson Med* 2008; 59(4):819-825.
- [37] Zhao T, Hu X. Iterative GRAPPA (iGRAPPA) for improved parallel imaging reconstruction. *Magn Reson Med* 2008; 59(4):903-907.
- [38] Blaimer M, Gutberlet M, Kellman P, Breuer FA, Kostler H, Griswold MA. Virtual coil concept for improved parallel MRI employing conjugate symmetric signals. *Magn Reson Med* 2009; 61(1):93-102.
- [39] Honal M, Bauer S, Ludwig U, Leupold J. Increasing efficiency of parallel imaging for 2D multislice acquisitions. *Magn Reson Med* 2009; 61(6):1459-1470.
- [40] Chen Z, Zhang J, Yang R, Kellman P, Johnston LA, Egan GF. IIR GRAPPA for Parallel MR Image Reconstruction. *Magn Reson Med* 2010; 63(2):502-509.
- [41] Chang Y, Liang D, Ying L. A nonlinear GRAPPA method for improving SNR. In Proc. of the 19th ISMRM annual meeting, Stockholm, Sweden, 2010. p. 4906.
- [42] Park J, Zhang Q, Jellus V, Simonetti O, Li D. Artifact and noise suppression in GRAPPA imaging using improved k-space coil calibration and variable density sampling. *Magn Reson Med* 2005; 53(1):186-193.
- [43] Haacke EM, Brown RW, Thompson MR, Venkatesan R. *Magnetic resonance imaging physical principles and sequence design*. New York: Wiley-Liss; 1999. p 569-617.
- [44] Schultz CL, Alfidi RJ, Nelson AD, Kopiwoda SY, Clampitt ME. The effect of motion on two-dimensional Fourier transformation magnetic resonance images. *Radiology* 1984; 152(1):117-121.
- [45] Welch EB, Felmlee JP, Ehman RL, Manduca A. Motion correction using the k-space phase difference of orthogonal acquisitions. *Magn Reson Med* 2002; 48(1):147-156.

- [46] Kruger DG, Slavin GS, Muthupillai R, Grimm RC, Riederer SJ. An orthogonal correlation algorithm for ghost reduction in MRI. *Magn Reson Med* 1997; 38(4):678-686.
- [47] Pipe JG. Motion correction with PROPELLER MRI: Application to head motion and free-breathing cardiac imaging. *Magn Reson Med* 1999; 42(5): 963-969.
- [48] Atkinson D, Hill DL, Stoye PN, Summers PE, Clare S, Bowtell R, Keevil SF. Automatic compensation of motion artifacts in MRI. *Magn Reson Med* 1999; 41(1):163-170.
- [49] Lee KJ, Barber DC, Paley MN, Wilkinson ID, Papadakis NG, Griffiths PD. Image-based EPI ghost correction using an algorithm based on projection onto convex sets (POCS). *Magn Reson Med* 2002; 47(4):812-817.
- [50] Skare S, Newbould RD, Nordell A, Holdsworth SJ, Bammer R. An auto-calibrated, angularly continuous, two-dimensional GRAPPA kernel for PROPELLER trajectories. *Magn Reson Med* 2008; 60(6):1457-1465.
- [51] Stevick JW, Harding SG, Paquet U, Ansorge RE, Carpenter TA, Williams GB. Gaussian process modeling for image distortion correction in echo planar imaging. *Magn Reson Med* 2008; 59(3):598-606.
- [52] Tamez-Pena JG, Totterman S, Parker KJ. MRI isotropic resolution reconstruction from two orthogonal scans. In *Proc. SPIE Medical Imaging 2001: Image Processing*; 4322:87-97.
- [53] Nelder JA, Mead R. A simple method for function minimization. *Comput J* 1965; 7:308-313.
- [54] Davidon WC. Variable Metric Method for Minimization. *SIAM J Optimization* 1991; 1:1-17.
- [55] Candès EJ, Romberg J. Sparsity and incoherence in compressive sampling. *Inverse Problems* 2007; 23: 969-985.
- [56] Rudelson M, Vershynin R. On sparse reconstruction from Fourier and Gaussian measurements. *Comm. Pure Appl. Math.* 2008; 61: 1025-1045.
- [57] Bajwa W, Haupt J, Raz G, Wright S, Nowak R. Toeplitz-structured compressed sensing

- matrices, In Proc. of IEEE Workshop on SSP, pp. 294-298, Oct. 2007.
- [58] Sebert F, Zou YM, Ying L. Toeplitz block matrices in compressed sensing and their applications in imaging. In Proc. of the 5th International Conference on ITAB, pp. 47-50, Jul. 2008.
- [59] Romberg J. Compressive sensing by random convolution. *SIAM J. Imaging Sci.* 2009; 2: 1098-1128.
- [60] Rauhut H. Circulant and toeplitz matrices in compressed sensing. In Proc. of SPARS, Apr. 2009.
- [61] Yin W, Morgan S, Yang J, Zhang Y. Parctical compressive sensing with Toeplitz and circulant matrices. In Proc. of SPIE VCIP, pp. 7740K-7740K-10, Jul. 2010.
- [62] Glub G., VanLoan C.F., "*Matrix computations*," The Johns Hopkins University Press, Baltimore, 1996.
- [63] Pauly J, Nishimura D, Macovski A. A k-space analysis of small-tip-angle excitation. *J. Magn. Reson.* 1989; 81: 43-56.
- [64] Zientara GP, Panych LP, Jolesz FA. Near-optimal spatial encoding for dynamically adaptive MRI: Mathematical principles and computational methods. *Magn Reson Med* 1999; 10(2):151-165.
- [65] Panych LP, Zientara GP, Jolesz FA. MR image encoding by spatially selective RF excitation: An analysis using linear response models. *Int. J. Imag. Syst. Tech.* 1999; 10:143-150.
- [66] Liang ZP, Lauterbur PC. Principles of magnetic resonance imaging: A signal processing perspective. IEEE Press, New York, USA, 2000.
- [67] Mitsouras D, Hoge WS, Rybicki FJ, Kyriakos WE, Edelman A, Zientara GP. Non-Fourier-encoded parallel MRI using multiple receiver coils. *Magn Reson Med* 2004; 52(2): 321-328.
- [68] Saiviroonporn P. Adaptive non-Fourier spatial encoding for dynamic MRI, PhD thesis,

Boston University, 1997.

- [69] Bernstein MA, King KF, Zhou XJ. Handbook of MRI pulse sequences. Boston, MA: Academic Press, 2004.
- [70] Chartrand R. Exact reconstruction of sparse signals via nonconvex minimization. *IEEE Signal processing Letters* 2007; 14(10):707-710.
- [71] Fischer A, Breuer F, Blaimer M, Seiberlich N, Jakob PM. Introduction of a nonconvex compressed sensing algorithm for MR imaging. In Proc. of the 16th ISMRM annual meeting, Toronto, Canada, 2008:1487.
- [72] Huang F, Duensing GR. A theoretical analysis of errors in GRAPPA. In Proceedings of the 14th ISMRM Annual Meeting, Seattle, Washington, USA, 2006. p. 2468.
- [73] Thunberg P, Zetterberg P. Noise distribution in SENSE- and GRAPPA-reconstructed images: a computer simulation study. *Magn Reson Imaging* 2007; 25:1098-1094.
- [74] Liu B, King FK, Steckner M, Xie J, Sheng J, Ying L. Regularized sensitivity encoding (SENSE) reconstruction using Bergman iterations. *Magn Reson Med* 2009; 61(1):145-152.
- [75] Wang H, Chang Y, Liang D, King KF, Nagasekar G, Ying L. Cross Sampled Nonlinear GRAPPA for Parallel MRI. In Proc. of the 21st ISMRM Annual Meeting, Melbourne, Australia, May 2012.
- [76] Cho ZH, Nalcioglu O, Park HW, Ra JB, Hilal SK. Chemical-shift artifact correction scheme using echo-time encoding technique. *Magn Reson Med* 1985; 2(3):253-261.
- [77] Glover G, Schneider E. Three-point dixon technique for true fat/water decomposition with B0 inhomogeneity correction. *Magn Reson Med* 1991; 18(2): 371-383.
- [78] Altbach MI, Trouard TP, Van de Walle R, Theilmann RJ, Clarkson E, Barrett HH, Gmitro AF. Chemical-shift imaging utilizing the positional shifts along the readout gradient direction. *IEEE Trans Med Imaging* 2001; 20(11):1156-1166.
- [79] Goelman G, Liu S, Fleysher R, Fleysher L, Grossman RI, Gonen O. Chemical-shift artifact reduction in hadamard-encoded MR spectroscopic imaging at high (3T and 7T) magnetic

- fields. *Magn Reson Med* 2007; 58(1):167-173.
- [80] Griswold MA, Blaimer M, Breuer F, Heidemann RM, Mueller M, Jakob PM. Parallel magnetic resonance imaging using the GRAPPA operator formalism. *Magn Reson Med* 2005; 54(6):1553-1556.
- [81] Blaimer M, Breuer FA, Mueller M, Seiberlich N, Ebel D, Heidemann RM, Griswold MA, Jakob PM. 2D-GRAPPA-operator for faster 3D parallel MRI. *Magn Reson Med* 2006; 56(6):1359-1364.
- [82] Arunachalam A, Samsonov AA, Block WF. Self-calibrated GRAPPA method for 2D and 3D radial data. *Magn Reson Med* 2007; 57:931-938.
- [83] Sharif B, Li D, Wagner S. Temporal acceleration in hyperpolarization imaging using image-domain compressed sensing. In *Proceedings of the 20th ISMRM Annual Meeting, USA, 2011*. p. 2468.
- [84] Prince JL, Links JM. *Medical imaging signal and systems*. Pearson Education Press, New Jersey, USA, 2006.
- [85] Bloch F, Nuclear induction, *Physical Review* 1946; 70:460-473.
- [86] Thorsten B., et. al., Fat and water magnetic resonance imaging. *J. Magn. Reson Imaging* 2010, 31(1):4-18.

CURRICULUM VITAE

Name: Haifeng Wang

Place of birth: Yuxi, Yunnan, P. R. China

Education:

B. S., Tsinghua University, Beijing July 2002

Major: Electrical Engineering

M. S., Tsinghua University, Beijing July 2005

Major: Electrical Engineering

Ph.D., University of Wisconsin, Milwaukee December 2012

Major: Electrical Engineering

Dissertation Title:

Accelerating MRI Data Acquisition Using Parallel Imaging and Compressed Sensing

Awards:

2012 UWM Chancellor's Graduate Student Award

2012 UWM Graduate Student Travel Award

2012 ISBI Travel Grant

2011 UWM Graduate Student Travel Award

Journal Publications:

- ♦ Haifeng Wang, Dong Liang, Kevin F. King, Leslie Ying. “Hybrid-Encoded CS MRI”. *Magnetic Resonance in Medicine*, in preparation.
- ♦ Haifeng Wang, Dong Liang, Kevin F. King, Nagarsekar Gajanan, Yuchou Chang, Leslie Ying. “Improving GRAPPA Using Cross-Sampled Autocalibration Data”. *Magnetic Resonance in Medicine*, Aug. 2011.
- ♦ Dong Liang, Haifeng Wang, Yuchou Chang, Leslie Ying. “Sensitivity Encoding Reconstruction with Nonlocal Total Variation Regularization”. *Magnetic Resonance in Medicine*, 65(5): 1384-1392, 2011.
- ♦ Haifeng Wang, Wenjuan Lu, Chuan Feng. “The Main Control Software of the Robot Glazing System”. *Journal of Computer Engineering and Applications*, China, 28:98-99, Oct. 2005.
- ♦ Haifeng Wang, Wenjuan Lu. “A Teaching Robot System for Glazing Potteries”. *Journal of Central South University (Science and Technology)*, China, 36(1):436-441, Aug. 5, 2005.

Conference Publications:

- ♦ Haifeng Wang, D. Liang, Kevin F. King, Leslie Ying. “Three-Dimensional Hybrid-Encoded MRI Using Compressed Sensing”. *Proc. of IEEE International Symposium on Biomedical Imaging (ISBI)*, Barcelona, Spain, May. 2012. Oral presentation.
- ♦ Haifeng Wang, Yuchou Chang, Dong Liang, Kevin F. King, Leslie Ying. “Cross Sampled Nonlinear GRAPPA for Parallel MRI”. *Proc. of International Society for Magnetic Resonance in Medicine (ISMRM) Annual Meeting and Exhibition*. Melbourne, Australia, May. 2012.
- ♦ Haifeng Wang, Dong Liang, Kevin F. King, Nagarsekar Gajanan, Leslie Ying. “Three-

- Dimensional Hybrid-Encoding for Compressed Sensing MRI”. *Proc. of International Society for Magnetic Resonance in Medicine (ISMRM) Annual Meeting and Exhibition*. Melbourne, Australia, May. 2012. Oral presentation.
- ♦ Haifeng Wang, Dong Liang, Kevin F. King, Nagarsekar Gajanan, Leslie Ying. “CS-GRAPPA: Improving GRAPPA Using Cross Sampling”. *Proc. of International Society for Magnetic Resonance in Medicine (ISMRM) Annual Meeting and Exhibition*. Montreal, Canada, May. 2011.
 - ♦ Haifeng Wang, Dong Liang, Kevin F. King, Nagarsekar Gajanan, Leslie Ying. “Cross-sampled GRAPPA for parallel MRI”. *Proc. of IEEE Annual International Conference of the Engineering in Medicine and Biology Society (EMBC)*, Buenos Aires, Argentina, Nov. 2010. Oral presentation.
 - ♦ Haifeng Wang, Dong Liang, Leslie Ying. “Pseudo 2D Random Sampling for Compressed Sensing MRI”. *Proc. of IEEE Annual International Conference of the Engineering in Medicine and Biology Society (EMBC)*, Minneapolis, USA, Sep. 2009.
 - ♦ Dong Liang, Haifeng Wang, Leslie Ying. “SENSE Reconstruction with Nonlocal TV Regularization”. *Proc. of IEEE Annual International Conference of the Engineering in Medicine and Biology Society (EMBC)*, Minneapolis, USA, Sep. 2009.
 - ♦ Dong Liang, Guangwu Xu, Haifeng Wang, Kevin F. King, Dan Xu, Leslie Ying. “Toeplitz Random Encoding MR Imaging Using Compressed Sensing”. *Proc. of IEEE International Symposium on Biomedical Imaging (ISBI)*, Boston, USA, July 2009.
 - ♦ Haifeng Wang, Dong Liang, Kevin F. King, Leslie Ying. “Toeplitz Random Encoding for Reduced Acquisition Using Compressed Sensing”. *Proc. of International Society for Magnetic Resonance in Medicine (ISMRM) Annual Meeting and Exhibition*. Hawaii, USA, Apr. 2009.
 - ♦ Haifeng Wang, Wenjuan Lu, Chuan Feng. “Locating Ceramics Based on Computer Vision”. *Proc. of IEEE Robotics, Automation and Mechatronics (RAM)*, 2:1120-1123,

Singapore, Nov. 2004.

- ♦ Ping Li, Wenjuan Lu, Haifeng Wang. “The Characteristics of the Transmission Delay via Internet and Analysis of the Real-Time Protocol Design”. *Proc. of IEEE International Conference on Networking Sensing and Control (ICNSC)*, Beijing, P.R. China, 2:1005-1008, Mar. 2005.

Peer-reviewer Activities:

- ♦ Journal reviewer for Open Access Medical Statistics
- ♦ Conference reviewer for *IEEE Annual International Conference of the Engineering in Medicine and Biology Society (EMBC)*

Patents:

- ♦ Haifeng Wang, Dong Liang, Leslie Ying. “Improving GRAPPA Using Cross Sampled Auto Calibration Data”. United States Provisional Patent Application No. 61/281,324 (Atty. File No. 020871-9056-US00).